Frequency stabilization and frequency conversion in high-Q silicon nitride microresonators

Thesis by
Bohan Li

In Partial Fulfillment of the Requirements for the
Degree of
Doctor of Philosophy

CALIFORNIA INSTITUTE OF TECHNOLOGY
Pasadena, California

2026
Defended October 22th, 2025

Bohan Li
ORCID: 0009-0007-8210-1903

ACKNOWLEDGEMENTS

I started my Ph.D. in 2020 during the turbulent time of Covid and ended it in 2025. The journey is nontrivial and I have special thanks to Prof. Vahala who advised my thesis work and provided funding throughout the years. In addition, I am grateful to the Caltech community for providing a good environment that allows me to focus on my thesis work.

ABSTRACT

Integrated photonics is an active research field in the recent decade. Silicon nitride is a prominent platform that features low optical loss and can be fabricated in a high-volume complementary metal–oxide–semiconductor (CMOS) foundry. The first part of the thesis focuses on taking advantage of these two mature properties to create integrated lasers with high frequency stability, which possibly has the lowest frequency noise among integrated lasers at the time when this thesis is written. Silicon nitride is also popular in the four-wave-mixing applications as it has an inherent high third-order optical nonlinearity $\chi^{(3)}$. In the second part of this thesis, however, I present advancement and applications of the second order optical nonlinearity $\chi^{(2)}$ in this material. The second order nonlinearity is not inherent but rather induced by optical signals through photogalvanic effect. This effect is presented as weak historically, but efficient applications are made available in this thesis through the high enhancement of low loss microresonators. Applications include efficient generation of low-noise and tunable lasers through second harmonic generation and demonstrating the quantum nature of correlated photon-pairs generated through spontaneous down conversion.

PUBLISHED CONTENT AND CONTRIBUTIONS

Li, Bohan, Zhiquan Yuan, James Williams, Warren Jin, Adrian Beckert, Tian Xie, Joel Guo, Avi Feshali, Mario Paniccia, Andrei Faraon, et al. (2025). "Down-converted photon pairs in a high-Q silicon nitride microresonator." In: *Nature* 639.8056, pp. 922–927. DOI: 10.1038/s41586-025-08662-3.

B. L. participated in the conception of the project, measurements, and writing of the manuscript.

Yuan, Zhiquan, Jinhao Ge, Peng Liu, Li, Bohan, Mingxiao Li, Jin-Yu Liu, Yan Yu, Hao-Jing Chen, John Bowers, and Kerry Vahala (2025). "Efficient and wavelength-tunable second-harmonic generation toward the green gap." In: *Science Advances* 11.27, eadw2781. DOI: 10.1126/sciadv.adw2781.

B. L. participated in the conception of the project, measurements, and writing of the manuscript.

Li, Bohan, Zhiquan Yuan, Warren Jin, Lue Wu, Joel Guo, Qing-Xin Ji, Avi Feshali, Mario Paniccia, John E Bowers, and Kerry J Vahala (2023). "High-coherence hybrid-integrated 780 nm source by self-injection-locked second-harmonic generation in a high-Q silicon-nitride resonator." In: *Optica* 10.9, pp. 1241–1244. DOI: 10.1364/OPTICA.498391.

B. L. participated in the conception of the project, measurements, and writing of the manuscript.

Yuan, Zhiquan, Heming Wang, Peng Liu, Li, Bohan, Boqiang Shen, Maodong Gao, Lin Chang, Warren Jin, Avi Feshali, Mario Paniccia, et al. (2022). "Correlated self-heterodyne method for ultra-low-noise laser linewidth measurements." In: *Optics Express* 30.14, pp. 25147–25161. DOI: 10.1364/OE.458109.

B. L. participated in the measurements of frequecy noise and writing of the manuscript.

Li, Bohan, Warren Jin, Lue Wu, Lin Chang, Heming Wang, Boqiang Shen, Zhiquan Yuan, Avi Feshali, Mario Paniccia, Kerry J Vahala, et al. (2021). "Reaching fiber-laser coherence in integrated photonics." In: *Optics Letters* 46.20, pp. 5201–5204. DOI: 10.1364/OL.439720.

B. L. participated in the conception of the project, measurements, and writing of the manuscript.

CONTENTS

LIST OF FIGURES

LIST OF TABLES

Chapter 1

INTRODUCTION

1.1 Integrated optical microresonators

Optical microresonators have been an active research area for decades. There are two main merits of microresonators in comparison to bulk optical cavities. First, it confines light into very small areas and enhances the light field within. This makes the optical effect that uses the second-order or third-order optical nonlinearity more significant. Typical applications are frequency conversion through three-wave mixing and frequency comb generation through four-wave mixing. It can also be used to enhance the light interaction with atoms and quantum dots (Vahala, 2003). The second benefit also comes from the small size. By replacing the bulk optical cavities with small microresonators, everything can be made smaller and perhaps cheaper.

Around 2025, the time when this thesis is drafted, articles published related with microresonator will very likely have the word 'on-chip' or 'integrated' in the title or abstract. The popular direction of research in this community now points to integrated photonics. Following the rise of integrated circuits, people came up with the concept of integrated photonics as an analogy of integrated circuits. The integrated photonics use optical materials that can be fabricated on a wafer scale in the same way as integrated circuits fabricated by commercial semiconductor foundries. People are imaging complicated photonic circuits where light is guided towards different components (including microresonator), and perhaps these circuits can do impressive tasks like how integrated circuits revolutionized computation power in the modern era. In this case, waveguides that can be fabricated on the same chip are also needed to couple light in and out of the resonator. Materials that cannot be integrated are considered to be not compact enough even though they may have higher Q factors. Historically, crystalline CaF_2 resonators made by mechanical polishing (Grudinin, Ilchenko, and Maleki, 2006) can achieve a quality(Q) factor of 10^{10}. And silica wedge microresonator (Lee et al., 2012) uses chemical etching that process multiple resonators at the same time on one wafer can achieve a 10^9 quality factor. These two types of resonators need to use an external tapered fiber to couple light in and out. Thus, they are not compatible with the idea of integrated photonics

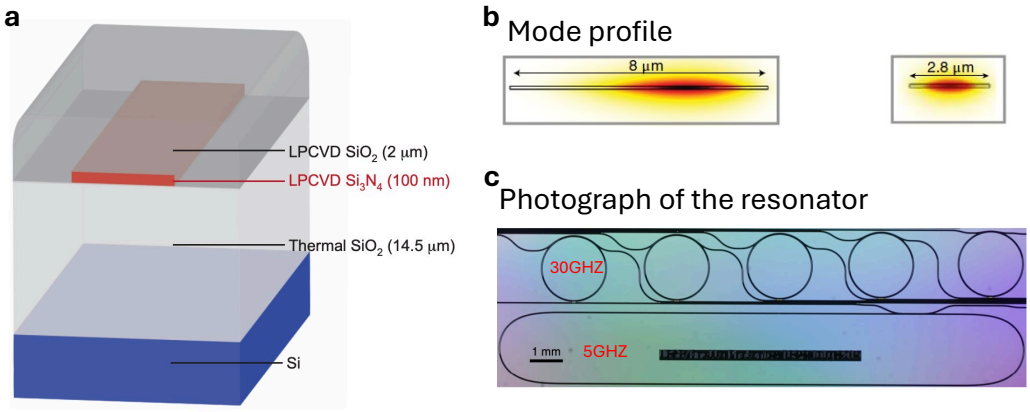

Figure 1.1: **Illustration of the thin-film silicon nitride platform. a** Cross-sectional diagram showing Si_3N_4 as the core material, silica as the cladding and silicon as the substrate. **b** Simulated mode profile of two different waveguide widths. **c** Top-view photograph of the Si_3N_4 microresonators.

and are no longer at the frontier of research.

There are many integrated photonic platforms for microresonators, such as silicon nitride (Jin et al., 2021; Ji et al., 2017; J. Liu et al., 2018), lithium niobate (X. Lu, Moille, Rao, et al., 2020; C. Wang et al., 2018), SiC (Guidry et al., 2020), diamond (Hausmann et al., 2014), tantala (Jung et al., 2021), AlGaAs (Chang et al., 2020), GaP (Wilson et al., 2020), AlN(X. Guo, Zou, and Tang, 2016). Silicon nitride is a leading platform in the telecommunication band due to its low optical loss, high third-order nonlinearity, ability to handle high power, and absence of two-photon absorption. Thin-film silicon nitride with thickness around 100nm has low optical loss. While thick-film waveguide with a thickness around 1000nm, has advantages in low bending losses, dispersion engineering, and high Kerr nonlinearity. All the work presented in this thesis uses the thin-film silicon nitride platform, which is known to have the lowest loss and highest quality factors among all integrated microresonators.

1.2 Thin-film silicon nitride platform

Shown in the Fig.1.1a, the silicon nitride waveguide sits on a silica substrate and is surrounded by a silica cladding. In the foundry, thermal silica is first grown on the silicon substrate and silicon nitride is deposed on the top, using a process called low-pressure chemical vapor deposition (LPCVD). After which a lithography and plasma etch are performed to shape the layer of silicon nitride into target geometric structure, such as a ring or a racetrack. Another layer of silica is deposited on the

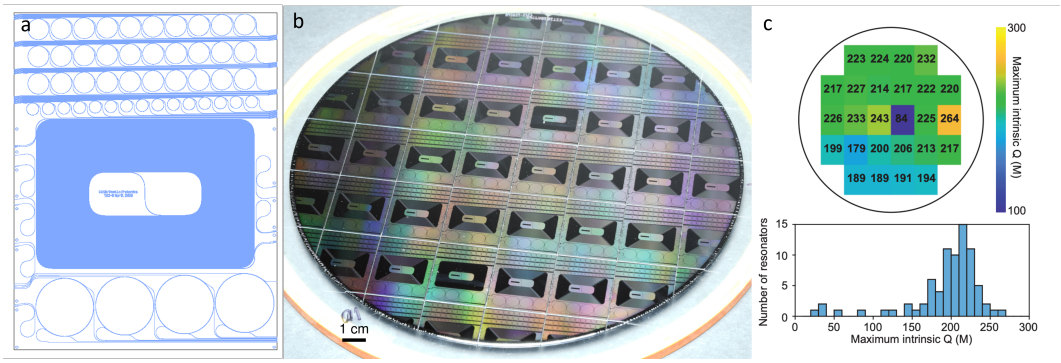

Figure 1.2: **Typical workflow from designing to testing.** **a** Digital mask generated with software. **b** Fabricated 200mm wafer delivered from foundry. **c** Measured quality factor distribution on the wafer.

top as guiding material and also as cladding to protect the waveguide. The whole device is then annealed at 1000 Celsius degree to let the hydrogen inside the silicon nitride core and cladding silica to defuse out.

Cross sections of the modes with two different waveguide widths is the shown in Fig.1.1b, about 90% percent of the mode is in the silica. The dispersive distribution is caused by the small thickness of 100 nm. Because silica has lower loss than silicon nitride, low confinement silicon nitride waveguide tends to be less lossy than their high confinement couterpart, where the majority of the mode is inside the silicon nitride core. The design also reduces mode overlap with the sidewall of the waveguide, which is rougher due to the fabrication process. A photograph of 30 GhZ free spectral range ring resonator and 5 Ghz free spectral range racetrack resonator is shown in Fig.1.1c. Waveguides are integrated on the same chip to couple light in and out.

The fabrication process is carried out in a high-volume complementary metal–oxide–semiconductor (CMOS) foundry. The work flow on our end is summarized in Fig1.2. A mask of silicon nitride photonic circuits is first designed and drawn using a software. The mask is sent to the CMOS foundry. We received the wafer and diced them into individual chips for testing. Quality factors of the resonators on the same wafer are measured and summarized in Fig1.2c. Chips with quality factors that meet the requirements are selected for further tasks.

The work presented in this thesis focuses on two specific applications, frequency stabilization and frequency conversion. A brief introduction is given below to help better understanding of the following chapters.

1.3 Frequency stabilization using microresonators

Using a cavity to increase the coherence of a noisy laser (a laser diode for example) is a common practice. Every PhD student in experimental optics should have experience with this technique. The most common one is external cavity diode laser (ECDL). Almost all the widely tunable commercial lasers (Toptica, Newport, etc.) are ECDLs, which directly use optical feedback from the cavity to stabilize the laser. Another popular technique is Pound-Drever-Hall (PDH) locking that extracts the frequency deviation from the cavity resonance electronically and then sends it back to laser for correction. These two techniques are readily applicable by switching the bulk cavity to microresonator. The benefit of using a microresonator is that it takes a small size and could be cheap to manufacture. There is a company (OEwaves) making a living by selling lasers locked to billion-Q-level crystalline microresonators. In regards of performance, the advantage comes from the high quality factor, but it also suffers from fundamental limitations such as thermal refractive noise (TRN) for having a small size. An attempt to address the TRN issue will be presented in Chapter 2 of this thesis.

Apart from real world applications, integrated photonics also has a need for integrated lasers. Integrated lasers refer to lasers that can be fabricated on the same wafer together with other integrated phonics components. PDH-locking a laser to a microresonator is a way to make use of microresonator but quite far away from an integrated laser. The photodetectors and electronic circuits therein are necessary parts for the PDH scheme and are hard to integrate. Nonetheless, having a piece of integrated photonics in the system is one step closer towards integration. Coupling a laser diode to the microresonator through an ECDL-like scheme is considered hybrid-integrated, as the laser and microresonator are on two different chips though they are physically very close to each other. For silicon nitride specifically, it is possible to heterogeneously integrate the III-V material laser diode and silicon nitride microresonator on the same chip(Xiang et al., 2023), which is a higher level of integration.

This thesis has two chapters about hybrid-integrated lasers using the self-injection locking and it is useful to introduce some basic background.

Self-injection lock

The principle of self-injection locking is well understood back in 1980s (Laurent, Clairon, and Breant, 1989). It uses the optical feedback from an external cavity to

lock the laser diode to the resonance of that cavity, and the laser would be stabilized if the linewidth of the cavity is narrow enough. The idea is the same as an external cavity diode laser. There are two components that are important, the quality factor of the external cavity and the strength of the feedback. In a microresonator the feedback comes from Rayleigh backscattering rather than the mirror reflections in typical ECDL. Mathematical formula of noise reduction specific to microresonator can be found in (Kondratiev et al., 2017). It suggests that the laser noise reduction factor is proportional to the square of microresonator quality factor and the square of feedback strength. In practice, the exact relationship is hard to verify but the laser performance is indeed better by using a microresonator with higher quality factor. The backscattering strength is the amount of light that is fed back to the laser. It consists of two parts, the coupling factor between the laser and the microresonator and the Rayleigh backscattering from the microresonator. The author verified through experiments that coupling factor is significantly correlated with the noise reduction factor. The Rayleigh backscattering of microresonator is hard to measure correctly and not controllable through the design and fabrication process. Thus it is treated as a random variable most of the time. To achieve a high coherence, one should pick a high quality factor microresonator and optimize the coupling between laser diode and the microresonator. The silicon nitride microresontors thus have unique advantages due to its high quality factors. Chapter 2 and 3 will present works using the self-injection lock technique with silicon nitride microresonator to achieve the world's narrowest linewidth in hybrid integrated lasers.

1.4 Frequency conversion using microresonator

Frequency conversion uses the second order or third order optical nonlinear effect to create frequency that is different from the pump. The use of microresonator is natural, small mode volume and high quality factors are key factors that enhance optical nonlinear effects. In four-wave-mixing, sub-milliwatt parametric oscillation threshold is observed using silicon nitride (Ji et al., 2017). In three-wave-mixing, a 5,000,000%/W second-harmonic conversion efficiency has been recorded using lithium niobate (J. Lu et al., 2020). These are levels not attainable in the bulk optical systems. The application of third order optical nonlinearity in microresonator includes the generation of Kerr frequency combs, soliton and low noise microwave signal. It can also be used to convert laser signal from 1570nm to 670nm with the assistance of a 940nm laser (X. Lu, Moille, Li, et al., 2019). The application of second order optical nonlinearity includes second harmonic generation, optical parametric

oscillations, and generation of entangled photon pairs. Chapter 4,5,6 presents work relevant to second harmonic generation. Details about the photogalvanic-induced second order nonlinearity will be given in those chapters and a brief introduction of second harmonic generation is given below.

Second harmonic generation in a microresonator

The second harmonic generation(SHG) in a microresonator involves two modes, pump mode and second harmonic (SH) mode. Frequencies of the two modes need to match, ω_{SH} =2ω_p for energy conservation. And the integration of the term $\chi^{(2)}E_p^2E_{SH}^*$ over the entire volume needs to be non-zero, where E_p,E_{SH} stands for electric field of the pump mode and SH mode respectively. If we treat the second order nonlinearity $\chi^{(2)}$ as a uniform value, this gives another requirement on the mode number, m_{SH}=2m_p. Two modes satisfying the above criteria are called natural phase matching. Due to chromatic dispersion, two modes from the same mode family normally cannot satisfy both relationships at the same time. One needs to select two modes from different families, and two mode families may only satisfy both conditions on a single wavelength. Note that the mode number matching condition is strict but the frequency matching can tolerate error within the resonator linewidth. In experiments, the frequency difference can be further reduced by tuning the temperature of the microresonator. The phase matching condition can also be satisfied with a spatially varied $\chi^{(2)}$, such as periodic poling in lithium niobate and photogalvanic induced grating in silicon nitride. This is quasi phase match and the period of $\chi^{(2)}$, needs to compensate the difference between $2m_p$ and m_{SH}. To have a high efficiency SHG, the engineering target is to maximize the integration of $\chi^{(2)}E_p^2E_{SH}^*$. In natural phase matching case, one wants to carefully select the cross-section of microresonator so that the phase matching condition can be satisfied at the desired wavelength. A thick core is needed in practice and one typically uses fundamental mode for the pump and a higher order mode for the SH. The mode overlap between these two modes is small. In material where $\chi^{(2)}$ could be changed spatially, one can phase match two fundamental mode so that the mode overlap is optimized.

Engineering concerns for thin-film silicon nitride design

The photogalvanic effect in silicon nitride will automatically match the mode number difference between two modes as long as energy conservation is matched (details can be found in Chapter 4,5,6 and the reference therein). The design principle is to

optimize Q factor, reduce mode volume and design couplers that can couple out two modes, preferably two fundamental modes. Reducing mode volume will increase bending loss and degrading Q factors, and there is a balance in choosing the size. Since the SH mode has a smaller profile, a pulley waveguide is needed to wrap around the resonator to ensure enough coupling. The fundamental mode will be leaked through this coupler which degrades Q factor, but it exhibits periodic pattern, shown in chapter 3. It is possible to minimize this loss through careful design and selecting an appropriate wavelength.

1.5 Thesis outline

In this thesis, we focus two applications of the optical microresonators: frequency stabilization and frequency conversion. The contents include the generation of low-noise mid-IR laser using a spiral resonator(Chapter 2) and a detailed documentation of the methods used to characterize the frequency noise(Chapter 3). We also demonstrated generation of low-noise laser at 780nm through second harmonic generation in silicon nitride(Chapter 4). We use a similar idea to generate tunable laser in the green band through frequecy doubling of 1um pump laser (Chapter 5). Finally we look at spontaneous down conversion and generate entangled photon pairs using a silicon nitride microresonator(Chapter 6).

The thesis is organized as follows:

Chapter 2 focuses on generating low-noise near-IR integrated laser using self-injection-lock technique. This work specifically addresses the limitation of thermal refractive noise that comes with the compact size of microresonator. A 1.4m spiral resonator is designed to increase the mode volume and reduce the thermal refractive noise. A record-low 40mHz Lorentzian linewidth is achieved with this method.

Chapter 3 describes the technique used to measure the laser frequency noise that are used in Chapter 2 and Chapter 4. The technique expands upon the traditional self-delayed heterodyne method and adds a cross-correlation signal processing that can reduce the noise originating from the photodetectors and other components in the measurement setup. It can achieve a noise floor of $0.01\text{Hz}^2/\text{Hz}$ at 1MHz offset frequency.

Chapter 4 investigates the combination of photogalvanic induced second-order nonlinearity and self-injection lock in a silicon nitride microresonator. A semiconductor laser diode is self-injection-locked to a silicon nitride microresonator. Photogalvanic effect creates a charge grating that matches the phase of two optical

modes. The generate low noise mid-IR laser is converted to 780nm through efficient second harmonic generation at an efficiency of 114%/W. A record low noise floor of $4Hz^2/Hz$ is achieved for a 780nm laser signal.

Chapter 5 extends the second harmonic generation (SHG) using silicon nitride resonators to the green spectrum. The on-chip green power as high as 5.3mW is generated with a conversion efficiency of 141%/W.The work provides a new convenient way to generate high power green light with semiconductor lasers. Flexible wavelength tunability and grating formation dynamics are also documented.

Chapter 6 demonstrates entangled photon pair generated through spontaneous parametric down conversion(SPDC) using silicon nitride microresonators. A pair generation rate of 0.8 million pairs/s on-chip are recorded. This shows the photogalvanic induced second-order nonlinearity is strong enough for quantum applications and further broadens the potential of silicon nitride platform. A transient behavior of the optically induced charges is also reported, which presents a challenge but can be addressed by periodic refresh of the photogalvanic effect.

References

Chang, Lin et al. (2020). "Ultra-efficient frequency comb generation in AlGaAs-on-insulator microresonators." In: *Nature communications* 11.1, p. 1331.

Grudinin, Ivan S, Vladimir S Ilchenko, and Lute Maleki (2006). "Ultrahigh optical Q factors of crystalline resonators in the linear regime." In: *Physical Review A—Atomic, Molecular, and Optical Physics* 74.6, p. 063806.

Guidry, Melissa A et al. (2020). "Optical parametric oscillation in silicon carbide nanophotonics." In: *Optica* 7.9, pp. 1139–1142.

Guo, Xiang, Chang-Ling Zou, and Hong X Tang (2016). "Second-harmonic generation in aluminum nitride microrings with 2500%/W conversion efficiency." In: *Optica* 3.10, pp. 1126–1131.

Hausmann, BJM et al. (2014). "Diamond nonlinear photonics." In: *Nature Photonics* 8.5, pp. 369–374.

Ji, Xingchen et al. (2017). "Ultra-low-loss on-chip resonators with sub-milliwatt parametric oscillation threshold." In: *Optica* 4.6, pp. 619–624.

Jin, Warren et al. (2021). "Hertz-linewidth semiconductor lasers using CMOS-ready ultra-high-Q microresonators." In: *Nat. Photon.* 15.5, pp. 346–353.

Jung, Hojoong et al. (2021). "Tantala Kerr nonlinear integrated photonics." In: *Optica* 8.6, pp. 811–817.

Kondratiev, NM et al. (2017). “Self-injection locking of a laser diode to a high-Q WGM microresonator.” In: *Opt. Express* 25.23, pp. 28167–28178.

Laurent, Ph, A Clairon, and Ch Breant (1989). “Frequency noise analysis of optically self-locked diode lasers.” In: *IEEE Journal of Quantum Electronics* 25.6, pp. 1131–1142.

Lee, Hansuek et al. (2012). “Chemically etched ultrahigh-Q wedge-resonator on a silicon chip.” In: *Nature Photonics* 6.6, pp. 369–373.

Liu, Junqiu et al. (2018). “Ultralow-power chip-based soliton microcombs for photonic integration.” In: *Optica* 5.10, pp. 1347–1353.

Lu, Juanjuan et al. (2020). “Toward 1% single-photon anharmonicity with periodically poled lithium niobate microring resonators.” In: *Optica* 7.12, pp. 1654–1659.

Lu, Xiyuan, Gregory Moille, Qing Li, et al. (2019). “Efficient telecom-to-visible spectral translation through ultralow power nonlinear nanophotonics.” In: *Nature Photonics* 13.9, pp. 593–601.

Lu, Xiyuan, Gregory Moille, Ashutosh Rao, et al. (2020). “On-chip optical parametric oscillation into the visible: generating red, orange, yellow, and green from a near-infrared pump.” In: *Optica* 7.10, pp. 1417–1425.

Vahala, Kerry J (2003). “Optical microcavities.” In: *nature* 424.6950, pp. 839–846.

Wang, Cheng et al. (2018). “Integrated lithium niobate electro-optic modulators operating at CMOS-compatible voltages.” In: *Nature* 562.7725, pp. 101–104.

Wilson, Dalziel J et al. (2020). “Integrated gallium phosphide nonlinear photonics.” In: *Nature Photonics* 14.1, pp. 57–62.

Xiang, Chao et al. (2023). “3D integration enables ultralow-noise isolator-free lasers in silicon photonics.” In: *Nature* 620.7972, pp. 78–85.

Chapter 2

REACHING FIBER-LASER COHERENCE IN INTEGRATED PHOTONICS

[1]We self-injection-lock a diode laser to a 1.41 m long, ultra-high-Q integrated resonator. The hybrid-integrated laser reaches a frequency noise floor of 0.006 Hz^2/Hz at 4 MHz offset, corresponding to a Lorentzian linewidth below 40 mHz – a record among semiconductor lasers. It also exhibits exceptional stability at low offset frequencies, with frequency noise of 200 Hz^2/Hz at 100 Hz offset. Such performance, realized in a system comprised entirely of integrated photonic chips, marks a milestone in the development of integrated photonics; and for the first time exceeds the frequency noise performance of commercially-available, high-performance fiber lasers.

2.1 Introduction

Optical metrology applications such as optical atomic clocks, automotive LiDAR, bio-sensing, and microwave photonics are placing increasingly stringent demands on the spectral purity, form factor, and stability of light sources. These emerging applications require optical performance not currently available in silicon photonics plaforms from commercial foundries. Meanwhile, ultra-low-loss silicon nitride has emerged as a leading platform for realising high-performance optical systems in a compact, affordable, and mass-manufacturable way (Blumenthal et al., 2018; Liu et al., 2021). Integrated resonators with 260 M Q factor and bend radius below 1 mm (Jin, Yang, et al., 2021), and on-chip delay lines over 20 m in length (Jin, Feshali, et al., 2021), have been fabricated on 200 mm wafers in complementary-metal-oxide-semiconductor (CMOS) foundries. This suggests that Q factors over 100 M, long the exclusive domain of academic research, may soon become accessible to real-world applications.

Recent advances have revealed a pathway towards ultra-narrow linewidth on-a-chip by self-injection-locking (SIL) integrated lasers to ultra-high Q microresonators (Shen et al., 2020; Jin, Yang, et al., 2021; Xiang et al., 2021). Compared to other means of laser stabilisation, such as Pound-Drever-Hall locking of a laser to

[1]Work presented in this chapter has been published in "Reaching fiber-laser coherence in integrated photonics", *Optics Letters* 46 (20), 5201-5204.

a reference cavity, SIL is well suited to integrated photonics due to its simplicity. Coupling a diode laser chip to a silicon nitride chip in a hybrid (Shen et al., 2020; Jin, Yang, et al., 2021; Lihachev et al., 2021; Oldenbeuving et al., 2012; Fan, Epping, et al., 2016) or heterogeneous (Xiang et al., 2021) integration scheme stabilises the laser without extraneous hardware such as electronic control circuitry, modulators, or isolators. In self-injection locking, surface and bulk inhomogeneities in the resonator lead to backscattering. When the laser frequency is aligned sufficiently close to a resonance frequency, the optical field reflected from within the resonator provides feedback to spontaneously align the laser to the resonance, dramatically reducing the laser linewidth (Dahmani, Hollberg, and Drullinger, 1987; Hjelme, Mickelson, and Beausoleil, 1991; Kondratiev et al., 2017; Matsko et al., 2007). The frequency noise reduction is proportional to the resonator Q factor squared (Li and Abraham, 1989), such that for sufficiently high Q factor, the laser linewidth reaches the thermodynamic limit imposed by microscopic thermal fluctuations within the resonator (Gorodetsky and Grudinin, 2004). In this work, we probe the limit imposed by this thermorefractive noise (TRN) in ultra-low-loss silicon nitride waveguides by fabricating large-mode-volume spiral resonators (Lee et al., 2013). Through SIL of a laser diode, these devices demonstrate frequency noise at or beyond the level of high-performance fiber lasers.

2.2 Design and fabrication of sprial resonators

To achieve large mode volume in a compact footprint, we design spiraled resonators (Lee et al., 2013) in an ultra-low-loss integrated photonic platform (Bauters et al., 2011; Jin, Yang, et al., 2021) featuring a 100 nm thick silicon nitride core, 2.2 μm thick tetraethyl-orthosilicate (TEOS) -based silicon dioxide top cladding, and 14.5 μm thick thermally oxidized silicon dioxide bottom cladding. The devices (pictured in Fig. 2.1a) were fabricated on 200 mm silicon wafers in a CMOS foundry (Jin, Yang, et al., 2021). Each resonator is drawn from two identical Archimedes spirals (Chen, Lee, and Vahala, 2014) with 40 μm pitch and minimum bend radius of 2 mm. The two spirals share a common center of curvature, and are interleaved by rotating one spiral by 180° with respect to the other. The resonator is formed by linking interior and exterior spiral endpoints with adiabatically curved transitions (Ladouceur and Labeye, 1995) with 0.9 mm minimum bend radius, drawn to precisely match direction and curvature with the spiral endpoints. Each adiabatic transition maintains 2.8 μm single-mode-waveguide width to prevent coupling to higher-order modes, while the waveguides widen to 10 μm waveguide width within

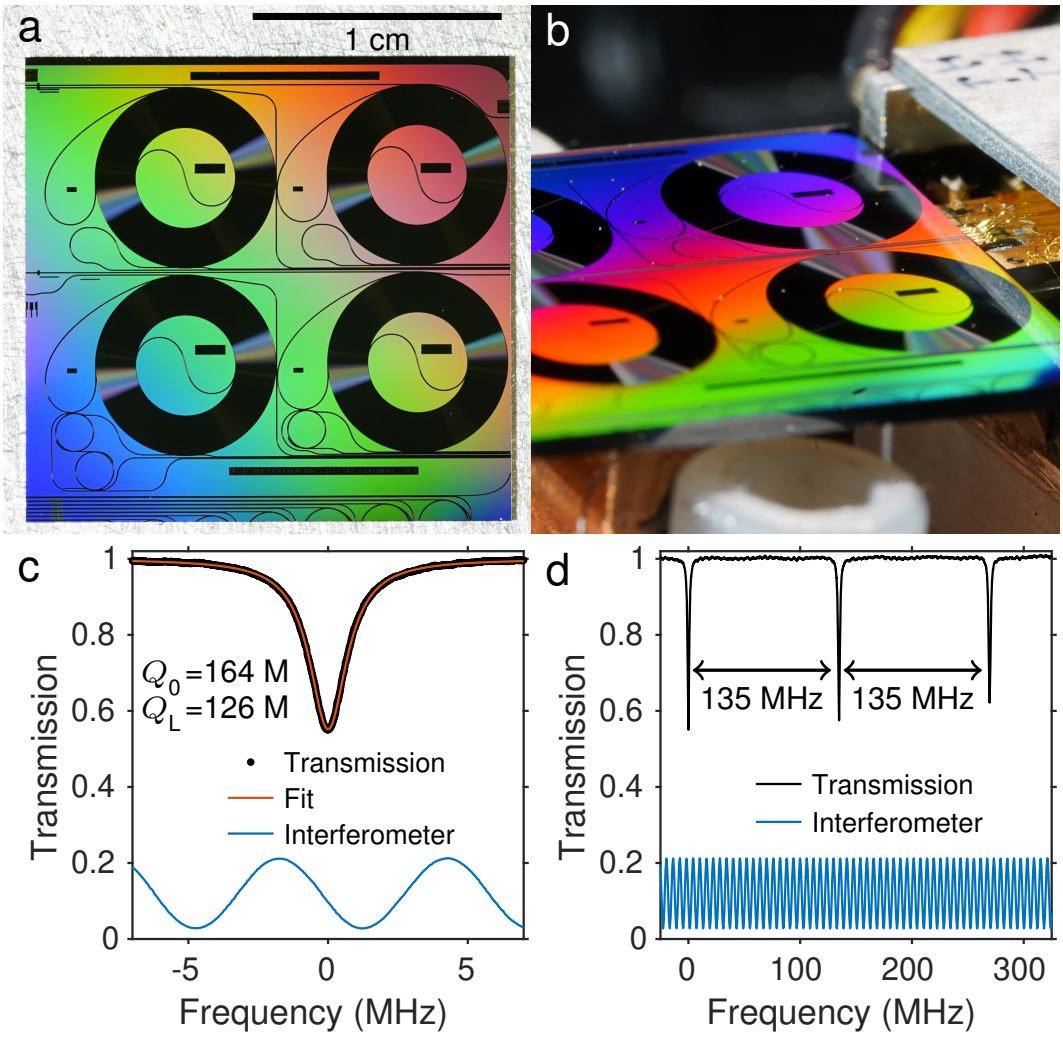

Figure 2.1: **The ultra-low-loss Si_3N_4 spiral resonators.** **(a)** Photograph of 1.41 m round-trip-length spiral resonators. Each resonator occupies a 9.2 mm×7.2 mm footprint. The chip features four independent, identical resonators, each designed with a different coupling strength. **(b)** Photograph of self-injection-locking (SIL) setup. **(c)** The transmission spectrum of a 1.41 m resonator with the measured intrinsic (Q_0=164) and loaded (Q_L=125.9±0.2) Q-factor values indicated. An average propagation loss of 0.17 dB/m within the resonator is implied by Q_0. Intrinsic Q factor is calculated assuming the coupling rate of the drop port is 0.7 of the through port, inferred from the design. **(d)** Transmission spectrum showing FSR of 135 MHz (134.73 ± 0.01 MHz) at 1551 nm.

the Archimedes spirals to minimize propagation loss. Two couplers are drawn along the outermost loop of the spiral to allow the SIL laser output to be taken from the drop-port, and thereby filter out high-offset frequency noise (Jin, Yang, et al., 2021). Resonators featuring round-trip length of 1.41 m (shown in Fig. 2.1a) and

0.312 m length (not pictured) were fabricated, with free spectral range of 135 MHz and 610 MHz, respectively.

2.3 Self-Injection-locking setup and light-current curve

The typical setup for SIL is shown in Fig. 2.1b. A commercial distributed-feedback (DFB) laser is butt-coupled to the spiral resonator using a 6-axis alignment stage, and is powered by an ultra-low-noise current source (ILX Lightwave LDX-3620B). Intrinsic and loaded Q factors as well as the FSR are measured for each resonator using a tunable laser calibrated by a fiber interferometer as illustrated for the 1.41 m resonator in Fig. 2.1c and Fig. 2.1d. We use a high power continuous wave (CW) 1550 nm DFB laser diode chip manufactured by Shenzhen PhotonX Technology Co. Ltd. The free-running DFB laser exhibits a lasing threshold of 15 mA, wavelength tunability of approximately 1 nm over a range of pump current up to 300 mA, and outputs 80 mW optical power for 250 mA pump current. The DFB laser and lensed fiber are coupled to the resonator using precision alignment stages (Thorlabs Nanomax 300 and 600). The total coupling loss, comprising coupling of the DFB laser to the on-chip waveguide and coupling from the on-chip waveguide to lensed fiber, is approximately 10 dB, while the insertion loss of the spiral resonator to its drop port is modeled to be 13 dB, due to the resonator being undercoupled.

As shown in Fig. 2.2a, single-mode lasing with large side-mode suppression ratio (SMSR) can be achieved over a wide range of pumping currents. Typical output power, collected from the drop port of the resonator, for the same range of pumping current, is shown in Fig. 2.2b. At each pumping condition, the air gap between the chips is adjusted to control the feedback phase (Dahmani, Hollberg, and Drullinger, 1987) to achieve single-mode lasing. Moreover, at any given pumping current, single-mode lasing can be observed at multiple distinct wavelengths depending on feedback phase. As a result, the wavelengths in Fig. 2.2a and power in Fig. 2.2b do not increase monotonically with the driving current, as they would in a free-running DFB laser. We note that below 80 mA, single-mode lasing could not be achieved for any feedback phase. Details of the single-mode lasing condition in the DFB-spiral system are under further study. Although the laser chip is mounted on a thermo-electric cooler, the spiral resonator is not temperature stabilized. Also, the air gap is not feedback stabilized. We believe that drift in the feedback phase and ambient temperature contribute to occasional mode hops between adjacent resonances of the resonator that were observed to occur on a time scale of approximately one hour. These factors could be addressed by packaging the device to improve thermal and

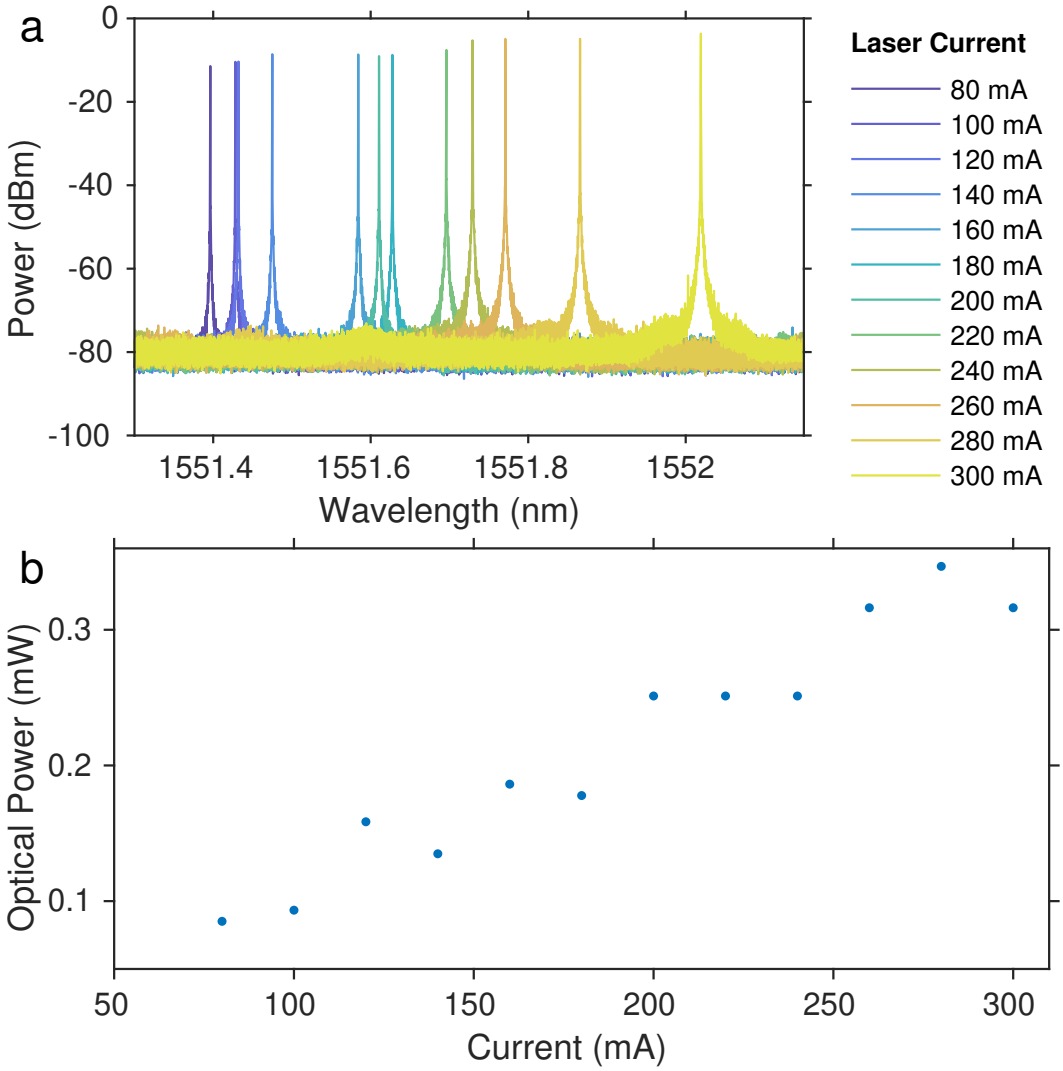

Figure 2.2: **Tuning curve of the self-injection-locked laser. (a)** Single-mode lasing with large side mode suppression ratio (SMSR) and **(b)** output power taken from the drop port of the SIL device (from a different scan) are shown for the 1.41 m long resonator at a series of pumping currents to the distributed feedback (DFB) laser. The data in (a) are collected using an optical spectrum analyzer (OSA) with 5 MHz resolution bandwidth (Apex AP2051A) in order to confirm single-mode operation.

mechanical stability (Liang et al., 2015). In a packaged device, as the gap between chips would no longer be adjustable, a resistive heater (Xiang et al., 2021) placed between the resonator and laser could be used instead to tune the feedback phase by the thermo-optic effect.

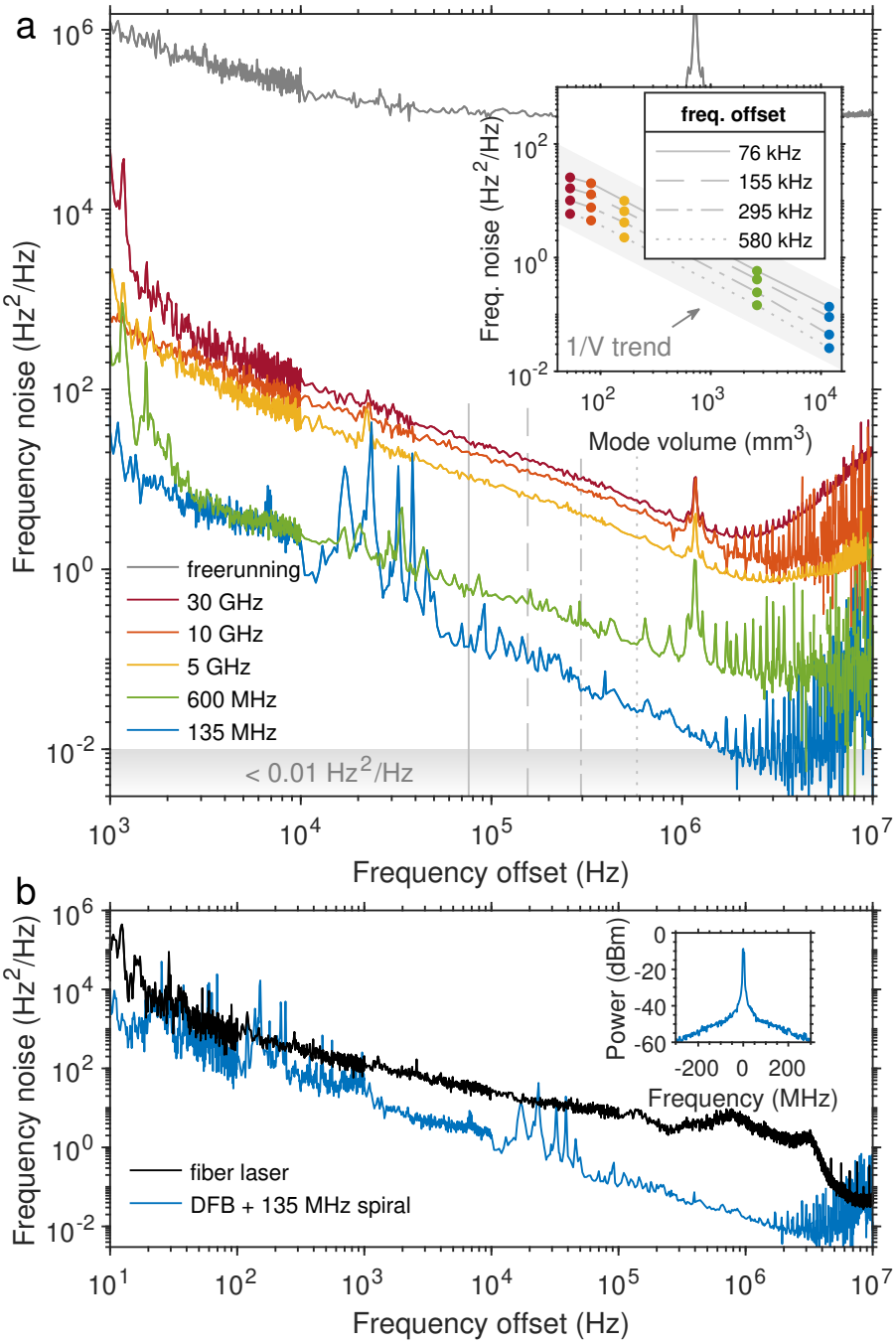

Figure 2.3: **Frequency noise measurement.** **(a)** Single-sideband frequency noise (FN) spectra of the DFB laser in free-running state, as well as in the SIL mode to resonators of various FSR. Vertical lines indicate the frequency offsets selected in the inset. Inset: FN versus mode volume at offset frequencies selected to avoid noise spurs and reveal the TRN floor. **(b)** FN comparison of a high-performance fiber laser to the SIL DFB laser using a 135 MHz spiral resonator. Inset: high-resolution optical spectrum of SIL DFB laser.

2.4 Charaterization of frequency noise

The frequency noise (FN) of the DFB laser self-injection-locked to the spiral resonators is shown in Fig. 2.3a. A commercial FN tester (OE4000) is used to measure FN below 10 kHz offset frequency. We combine this with a self-heterodyne cross-correlation method (Wang et al., 2020; Jin, Yang, et al., 2021) with higher sensitivity at offset frequency above 10 kHz. To explore the dependence on mode volume, we also measure the FN of the DFB laser self-injection locked to 30 GHz, 10 GHz, and 5 GHz FSR resonators studied in prior work (Jin, Yang, et al., 2021). The FN of these devices rises at high offset frequency (>2 MHz) due to their through-port configuration, as the frequency noise reduction factor decreases for offset frequency beyond the resonator's resonance bandwidth (Hjelme, Mickelson, and Beausoleil, 1991). However, the spiral resonators exhibit flat FN reduction factor at high offset frequency (Jin, Yang, et al., 2021) due to their drop-port configuration. We note that the noise spectrum for the FSR=135 MHz spiral device rises for offset frequencies above 4 MHz due to reaching the measurement-limited noise floor (see Appendix). FN below 10kHz offset is strongly influenced by environmental perturbations, and could be reduced by packaging, as discussed above. In the 10 kHz to 1 MHz range, we expect the FN to be dominated by thermorefractive contributions. In the inset, FN is plotted versus resonator mode volume, V, at selected offset frequencies. The data show strong agreement with the expected $1/V$ trend of TRN (Gorodetsky and Grudinin, 2004).

As shown in Fig. 2.3b, the FN of the DFB self-injection-locked to the 135 MHz spiral is comparable to or better than a high-performance fiber laser (Orbits Ethernal) over a wide range of offset frequencies. At high offset frequency, it outperforms the fiber laser by over an order of magnitude, reaching 0.006 Hz^2/Hz at 4 MHz, corresponding to Lorentzian linewidth (Jin, Yang, et al., 2021) below 40 mHz. Remarkably, the hybrid laser exhibits stability comparable to the fiber laser in the 100 Hz to 10 kHz frequency offset range as well, with a frequency noise level of 200 Hz^2/Hz at 100 Hz offset. In all configurations, we confirm single-mode operation of the SIL laser (Fig. 2.3b inset) using a high resolution (5 MHz resolution bandwidth) optical spectrum analyzer. We note that the noise spurs around 1 MHz offset, present in certain measurements, come from the pump current source, and are absent when using a different current source of the same model.

Details of the frequency noise (FN) measurement method are provided in the next chapter.Detectors used in the FN setup are a pair of Thorlabs PDB470C bal-

anced photodetectors, and a Keysight DSOS104A oscilloscope is used to record the data.The measurement-limited noise floor, reached by the FSR=135 MHz device in Fig. 2.3, is determined by the combination of the intrinsic photodetector noise, and the noise suppression factor of the cross-correlation technique on the photodetector noise (limited to 15 dB by the 50 ms time duration of data collection. The resulting noise floor scales with offset frequency, f, as f^2. All FN measurements in Fig. 2.3 are taken with pump currents in the range from 240 mA to 250 mA, with laser wavelength around 1551 nm. However, the FN spectra shown in Fig. 2.3 are typical of the SIL device for pump currents in the 100 mA to 300 mA range, which has been verified experimentally but not included in the paper.

2.5 Performance comparison and discussion

Finally, we compare this work with previous literature on narrow-linewidth integrated lasers. The Lorentzian (high-offset white frequency noise) linewidth is less than 0.04 Hz in this work, limited by the measurement noise floor. This substantially improves upon the 1.2 Hz linewidth in reference (Jin, Yang, et al., 2021), the 25 Hz linewidth in (Lihachev et al., 2021), and also surpasses the 0.1 Hz linewidth using non-planar crystalline resonators (Liang et al., 2015), achieved by self-injection locking. The current result is also much smaller than the 13 kHz (Stern et al., 2017) and 40 Hz linewidths (Fan, Rees, et al., 2020) demonstrated for silicon-nitride-external-cavity hybrid integrated lasers.

In conclusion, we self-injection-locked a DFB laser to a large-mode-volume spiral resonator to reduce thermorefractive noise. The resulting device has outstanding frequency noise characteristics that are comparable to or exceed that of a high performance fiber laser. Further improvements in wafer-scale heterogeneous integration may soon unite the laser and ultra-high Q resonator on a single substrate (Xiang et al., 2021), enabling the production of mass-manufactured laser sources with fiber-laser-equivalent coherence on a chip.

References

Bauters, Jared F et al. (2011). “Ultra-low-loss high-aspect-ratio Si_3N_4 waveguides.” In: *Opt. Express* 19.4, pp. 3163–3174.

Blumenthal, Daniel J et al. (2018). “Silicon nitride in silicon photonics.” In: *Proc. IEEE* 106.12, pp. 2209–2231.

Chen, Tong, Hansuek Lee, and Kerry J Vahala (2014). “Design and characterization of whispering-gallery spiral waveguides.” In: *Opt. Express* 22.5, pp. 5196–5208.

Dahmani, B, L Hollberg, and R Drullinger (1987). "Frequency stabilization of semiconductor lasers by resonant optical feedback." In: *Opt. Lett.* 12.11, pp. 876–878.

Fan, Youwen, Jörn P Epping, et al. (2016). "Optically Integrated InP–Si _3 N _4 Hybrid Laser." In: *IEEE Photonics J.* 8.6, pp. 1–11.

Fan, Youwen, Albert van Rees, et al. (2020). "Hybrid integrated InP-Si 3 N 4 diode laser with a 40-Hz intrinsic linewidth." In: *Opt. Express* 28.15, pp. 21713–21728.

Gorodetsky, Michael L and Ivan S Grudinin (2004). "Fundamental thermal fluctuations in microspheres." In: *J. Opt. Soc. Am. B* 21.4, pp. 697–705.

Hjelme, Dag Roar, Alan Rolf Mickelson, and Raymond G Beausoleil (1991). "Semiconductor laser stabilization by external optical feedback." In: *IEEE J. Quantum Electron.* 27.3, pp. 352–372.

Jin, Warren, Avi Feshali, et al. (2021). "Seamless multi-reticle photonics." In: *Opt. Lett.* 46, pp. 2984–2987.

Jin, Warren, Qi-Fan Yang, et al. (2021). "Hertz-linewidth semiconductor lasers using CMOS-ready ultra-high-Q microresonators." In: *Nat. Photon.* 15.5, pp. 346–353.

Kondratiev, NM et al. (2017). "Self-injection locking of a laser diode to a high-Q WGM microresonator." In: *Opt. Express* 25.23, pp. 28167–28178.

Ladouceur, Francois and E Labeye (1995). "A new general approach to optical waveguide path design." In: *J. Light. Technol.* 13.3, pp. 481–492.

Lee, Hansuek et al. (2013). "Spiral resonators for on-chip laser frequency stabilization." In: *Nat. Commun.* 4.1, pp. 1–6.

Li, H and NB Abraham (1989). "Analysis of the noise spectra of a laser diode with optical feedback from a high-finesse resonator." In: *IEEE J. Quantum Electron.* 25.8, pp. 1782–1793.

Liang, W et al. (2015). "Ultralow noise miniature external cavity semiconductor laser." In: *Nat. Commun.* 6.1, pp. 1–6.

Lihachev, Grigory et al. (2021). *Ultralow-noise frequency-agile photonic integrated lasers*. arXiv: 2104.02990 [physics.optics].

Liu, Junqiu et al. (2021). "High-yield, wafer-scale fabrication of ultralow-loss, dispersion-engineered silicon nitride photonic circuits." In: *Nat. Commun.* 12.1, pp. 1–9.

Matsko, Andrey B et al. (2007). "Whispering-gallery-mode resonators as frequency references. I. Fundamental limitations." In: *J. Opt. Soc. Am. B* 24.6, pp. 1324–1335.

Oldenbeuving, RM et al. (2012). "25 kHz narrow spectral bandwidth of a wavelength tunable diode laser with a short waveguide-based external cavity." In: *Laser Phys. Lett.* 10.1, p. 015804.

Shen, Boqiang et al. (2020). “Integrated turnkey soliton microcombs.” In: *Nature* 582.7812, pp. 365–369.

Stern, Brian et al. (2017). “Compact narrow-linewidth integrated laser based on a low-loss silicon nitride ring resonator.” In: *Opt. Lett.* 42.21, pp. 4541–4544.

Wang, Heming et al. (2020). “Towards milli-Hertz laser frequency noise on a chip.” In: *arXiv preprint arXiv:2010.09248*.

Xiang, Chao et al. (2021). “Laser soliton microcombs heterogeneously integrated on silicon.” In: *Science* 373.6550, pp. 99–103. ISSN: 0036-8075. DOI: 10.1126/science.abh2076. eprint: https://science.sciencemag.org/content/373/6550/99.full.pdf. URL: https://science.sciencemag.org/content/373/6550/99.

Chapter 3

CORRELATED SELF-HETERODYNE METHOD FOR LASER LINEWIDTH MEASUREMENTS

[1]Narrow-linewidth lasers are important to many applications spanning precision metrology to sensing systems. Characterization of these lasers requires precise measurements of their frequency noise spectra. Here we demonstrate a correlated self-heterodyne (COSH) method capable of measuring frequency noise as low as 0.01 Hz^2/Hz at 1 MHz offset frequency. The measurement setup is characterized by both commercial and lab-built lasers, and features low optical power requirements, fast acquisition time and high intensity noise rejection.

3.1 Introduction

Ultra-low-noise lasers are indispensable ingredients for a wide range of applications, including optical gyroscopes (Lai et al., 2020), optical atomic clocks (Newman, Maurice, Drake, et al., 2019), and light detection and ranging (LiDAR) systems (Suh and Vahala, 2018). Accurate measurement of ultra-low-noise frequency spectra is an essential prerequisite for optimizing their performance and advancing their applications. Hence, high demands are placed on measurement systems to characterize these lasers with low frequency noise floors and high intensity-fluctuation isolation.

Several methods have been used for laser linewidth characterization. Incoherent homodyne detection incorporates a fiber delay line exceeding the coherence length of the laser under test (Schumaker, 1984). While the method measures relatively high frequency noise levels accurately, it becomes inappropriate as the laser linewidth reaches Hz levels, where the coherence length is on the order of 10^5 km. Phase discriminators with sub-coherent-length delay have been proposed in such cases, either by locking to a quadrature point (J. Li et al., 2012; Lee et al., 2012) or using self-heterodyne detection to shift the signal to the radiofrequency (RF) domain so as to avoid low-frequency technical noise (Van Exter, Kuppens, and Woerdman, 1992; Ludvigsen, Tossavainen, and Kaivola, 1998). However, optical-to-electrical (OE) conversion at the photodetector (PD) introduces additional technical PD noise, and

[1]Work presented in this chapter has been published in "Correlated self-heterodyne method for ultra-low-noise laser linewidth measurements", *Optics Express* 30 (14), 25147-25161.

relative intensity noise (RIN) of the laser may also be coupled to the output signal through the OE conversion. These factors prevent the detection methods from achieving the sufficiently-low noise floor required for milli-Hertz-linewidth laser characterization. At the same time, cross-correlation has been applied to frequency noise characterization in the RF domain as a mature method for measuring ultra-low-noise microwave signals (Walls, 1992). This technique compares the signal against two references and correlates them to suppress the independent noise from the references. Similar techniques have been introduced in the optical domain to characterize sub-Hertz linewidth lasers with optical references (Xie et al., 2017).

In this paper, we demonstrate a reference-free self-heterodyne cross-correlator for ultra-low-noise laser linewidth measurements. By employing two PDs for OE conversion in the conventional self-heterodyne method, the cross-correlation can eliminate the need for references while extracting laser noise. In addition, balanced photodetectors (BPDs) are used to minimize the RIN coupling ratio. The cross-correlator has a noise floor lower than 0.01 Hz^2/Hz and 40.4 $dBrad^2$ RIN suppression at 1 MHz offset frequency. Various commercial and lab-built lasers are used to benchmark the measurements, including an external-cavity laser (ECL) and a distributed-feedback (DFB) laser with and without self injection locking. Factors that may impact cross-correlator performance, including environmental noise coupling and delay length selection, are also discussed. The measurement can be readily generalized to other wavelengths (Tran et al., 2021) and may advance the development of next-generation laser sources through rapid measurement of noise.

3.2 Measurement setup

The COSH setup is shown in Fig. 3.1(a). A laser under test is split by a three-port acousto-optic modulator (AOM) into frequency-downshifted (1^{st} order output) and unshifted (0^{th} order output) portions. The former is polarization-controlled and then recombined with the latter delayed by a 1-km-long fiber, which forms a modified Mach–Zehnder interferometer (MZI) with a free spectral range (FSR) of 214.06 kHz. The three-port AOM acts as a variable splitter that also uses the unshifted laser power compared to a two-port modulator. On the output side, instead of one PD, both outputs are divided and received by two identical balanced photodetectors (BPDs). Using BPDs helps suppress RIN and using two BPDs allows cross-correlation between the electrical outputs and suppresses independent BPD noise. The whole optical section of the system is isolated from the external environment with an acoustic shield. The BPD outputs are recorded using a high-

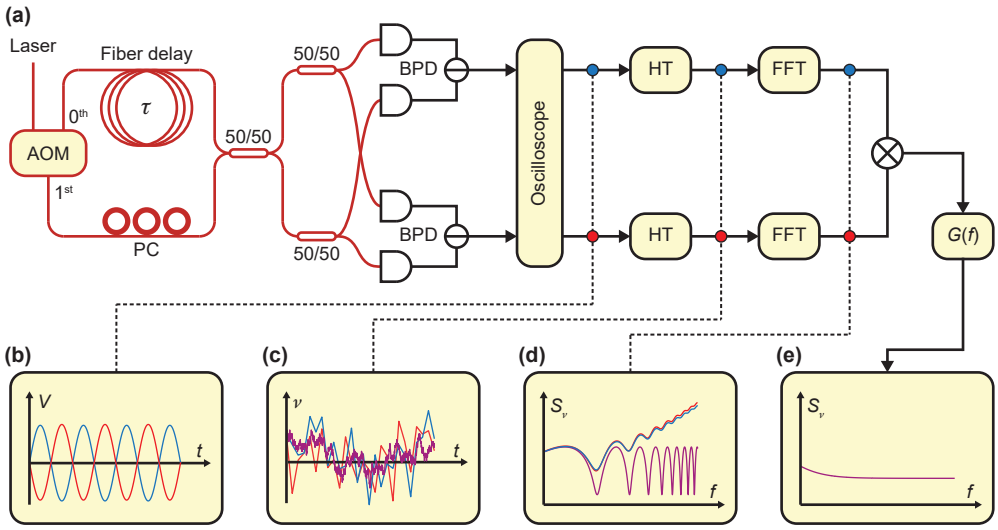

Figure 3.1: **Schematic of the correlated self-heterodyne (COSH) measurement setup.** **(a)** Illustration of the setup. AOM, acousto-optic modulator; PC, polarization controller; BPD, balanced photodetector; HT, Hilbert transform, followed by a time-domain difference operation; FFT, fast Fourier transform. **(b)** Self-heterodyne waveforms recorded by a high-speed oscilloscope. **(c)** Frequency fluctuations extracted with Hilbert transform and time-domain difference. The red and blue lines refer to the frequency fluctuations from two BPD outputs marked by color in accordance with inset (a) (similar hereinafter). Laser frequency noise (common mode) indicated by the purple line and BPD-induced noise (differential mode) are contained in the extracted results. **(d)** Power spectral density (PSD) of BPD output frequency given by FFT. The red and blue lines refer to the total noise PSD while the purple line indicates the laser frequency noise PSD (common mode). The deviation between them at high frequency is due to the BPD noise. **(e)** Single-sideband (SSB) laser noise after cross-correlation and $G(f)$ in which the BPD noise has been eliminated.

speed oscilloscope. The AOM is driven with a 55 MHz radio-frequency carrier which determines the center frequency of the recorded waveforms [Fig. 3.1(b)], and the sampling rate of the oscilloscope is set to 250 MHz to prevent aliasing. AC coupling at the oscilloscope is used to block low-frequency components that are spectrally far away from the carrier. The time delay between the two channels is estimated to be less than 0.5 ns and will not be considered in the following analyses. 2 seconds of waveforms (500×10^6 points for each channel, 1×10^9 points in total) are collected and transferred to a computer for data processing. While the record length is limited by the memory of our oscilloscope, it is sufficient to meet the noise floor requirements for the current measurements (see Section 4.3).

In the data processing part, phase fluctuations for each channel are extracted using

Hilbert transforms and then converted to frequency fluctuation through time-domain difference [Fig. 3.1(c)]. The Hilbert transform causes distortions at the endpoints of the waveforms, thus the first and last 40 ms (10×10^6 points) for each channel are discarded after the Hilbert transform. The remaining points are divided into non-overlapping segments (rectangular windowing, similar to Bartlett's method for estimating power spectra (Bartlett, 1948)), each with a τ_R time length [corresponding to a resolution bandwidth (RBW) of $1/\tau_R$] and fast-Fourier-transformed to obtain the frequency spectrum at a given offset frequency. For lower frequency offsets, the RBWs are made smaller with the segment lengths adjusted accordingly. The power spectrum density (PSD) of BPD output frequencies suffer from BPD noise [Fig. 3.1(d)]. To suppress this noise, the cross-correlation is calculated as the product between the Fourier coefficients of the two BPD output frequency spectra, averaged over all available segments. Owing to the independent nature of the two BPD noise sources, BPD noise can be suppressed compared to individual PSDs of BPD outputs. Finally, the cross-correlation spectrum is multiplied by a processing gain $G(f)$ to compensate the filtering effect from the MZI and recover the single-sideband (SSB) laser frequency noise result [Fig. 3.1(e)].

3.3 Modeling of the measurement process

In this section, we model the properties of the output signal from the COSH measurements. In the following, all spectral densities refer to two-sided spectral densities unless indicated otherwise.

Self-heterodyne noise detection

To model the self-heterodyne method for noise measurement, we begin with an idealized derivation, where a frequency-shifted signal beats against a delayed signal and the resulting frequency noise is calculated. From the Wiener-Khinchin theorem, the frequency noise of the original signal can be understood as the Fourier transform of the phase time-derivative correlation function:

$$S_\nu(f) = \int_{-\infty}^{\infty} \left\langle \frac{\dot{\phi}(0)}{2\pi} \frac{\dot{\phi}(t)}{2\pi} \right\rangle \mathrm{e}^{2\pi i f t} \mathrm{d}t = \frac{1}{4\pi^2} \int_{-\infty}^{\infty} \left\langle \dot{\phi}(0)\dot{\phi}(t) \right\rangle \mathrm{e}^{2\pi i f t} \mathrm{d}t \tag{3.1}$$

Here $S_\nu(f)$ is the frequency noise PSD of the input signal, f is the offset frequency, ϕ is the optical noisy phase signal, t denotes time, dot indicates derivative with respect to t and $\langle z \rangle$ denotes the ensemble average of z.

The self-heterodyne beating outputs a signal with phase $-2\pi f_\mathrm{c} t + \phi(t) - \phi(t-\tau)$, where τ is the delay time and f_c is the carrier frequency (determined by the AOM).

We are thus interested in the frequency noise of $\nu(\tau) = -f_c + [\dot{\phi}(t) - \dot{\phi}(t-\tau)]/(2\pi)$. By the time-shifting property of the Fourier transform we get

$$S_{\nu(\tau)}(f) = [2 - \exp(2\pi i f\tau) - \exp(-2\pi i f\tau)]S_\nu(f) = 4\sin^2(\pi f\tau)S_\nu(f) \quad (3.2)$$

thus the frequency noise reads

$$S_{\nu(\tau)}(f) = 4\sin^2(\pi f\tau)S_\nu(f) \quad (3.3)$$

The transfer function in the above equations has zeros at integer multiples of MZI FSR ($f = 1/\tau$, $2/\tau$, $3/\tau$ and so on). At these offset frequencies, destructive interference eliminates the phase difference at the MZI output. To compensate, the processing gain $G(f)$ should be chosen as

$$G(f) = \frac{1}{4\sin^2(\pi f\tau)} \quad (3.4)$$

We note that $G(f)$ diverges at integer multiples of the MZI FSR. This nonphysical divergence will be removed after the finite detection resolution bandwidth is properly considered (see discussion in section 3.3).

It is sometimes convenient to directly measure the phase noise corresponding to $S_{\nu(\tau)}(f)$, denoted as $S_{\varphi,\nu(\tau)}(f) \equiv S_{\nu(\tau)}(f)/f^2$ (e.g. by sending the RF signal directly to a phase noise analyzer). In this case,

$$S_{\varphi,\nu(\tau)}(f) = 4\frac{\sin^2(\pi f\tau)}{f^2}S_\nu(f) = (2\pi\tau)^2\,\mathrm{sinc}^2(f\tau)S_\nu(f) \quad (3.5)$$

where $\mathrm{sinc}\, z \equiv \sin(\pi z)/(\pi z)$ is the normalized sinc function.

Self-heterodyne noise detection using an AOM

Here we present a more rigorous derivation based on the setup described previously. Various non-ideal effects can be incorporated and compared against the experiments.

We assume a laser input signal of the form

$$A(t) = \exp(-2\pi i f_0 t)[1 + \delta a(t)]\exp[-i\delta\phi(t)] \quad (3.6)$$

where f_0 is the optical frequency. The δa and $\delta\phi$ are relative amplitude fluctuation and phase fluctuation, respectively, and are assumed to be small within the time scale of $1/f_c$, where $\delta\phi = \phi - 2\pi f_0 t$. This indicates that the laser would have low noise, which is the intended regime for the cross-correlator. Discussions on using the setup to measure a high-noise laser can be found below in Section 4.2.

The frequency-shifted signal becomes

$$A_1(t) = \frac{1}{\sqrt{2}} \exp(-2\pi i f_0 t) \exp(2\pi i f_c t)[1 + \delta a(t)] \exp[-i\delta\phi(t)] \tag{3.7}$$

and the delayed signal becomes

$$A_2(t) = \frac{1}{\sqrt{2}} \exp(-2\pi i f_0 t) \exp(2\pi i f_0 \tau)[1 + \delta a(t-\tau)] \exp[-i\delta\phi(t-\tau)] \tag{3.8}$$

where we have assumed that the AOM splits the light equally into two ports (which can be realized by adjusting the RF power input for the AOM).

The signals from the two arms are mixed at another coupler and form the MZI outputs. We do not assume *a priori* that the coupler is perfectly balanced and write the two output amplitudes as

$$A_+ = q_1 A_1 + i q_2 A_2, \quad A_- = q_1^* A_2 + i q_2^* A_1 \tag{3.9}$$

where q_1 and q_2 are complex transmission coefficients. We further assume that the two couplers just before the BPDs are matched, such that the relative power between the two arms remains the same at the two BPDs. In this case, powers at individual PDs can be found from $P_\pm \equiv |A_\pm|^2$, and the RF power of each BPD output reads, up to a proportional constant,

$$\Delta P \equiv P_+ - P_- = 2\mathrm{Re}[i q_1^* q_2 \exp(2\pi i f_0 \tau) \exp(-2\pi i f_c t)(1+\Sigma a) \exp(i\Delta\phi)] + \Delta|q|^2 \Delta a \tag{3.10}$$

where we have introduced some shorthand notations: $\Sigma a \equiv \delta a(t) + \delta a(t-\tau)$, $\Delta\phi \equiv \delta\phi(t) - \delta\phi(t-\tau)$, $\Delta a \equiv \delta a(t) - \delta a(t-\tau)$, and $\Delta|q|^2 \equiv |q_1|^2 - |q_2|^2$.

Next, the Hilbert transform is performed on ΔP to recover the analytic signal and extract the instantaneous phase. The terms within the brackets consist of the main part of ΔP and is itself an analytic signal oscillating at f_c. The Δa term may also influence the phase of the signal. However, only those frequency components of Δa around the carrier frequency f_c contribute to the phase noise at low offset frequencies. As the self-heterodyne beating shifts the phase noise information to f_c where the amplitude noise of a laser is extremely low, this effectively isolates the laser RIN from entering the phase extraction process. We can therefore approximate the analytic signal by

$$\mathcal{H}\Delta P \approx 2 i q_1^* q_2 \exp(2\pi i f_0 \tau) \exp(-2\pi i f_c t)(1 + \Sigma a) \exp(i\Delta\phi) \tag{3.11}$$

and the phase can be extracted as

$$\varphi = \Delta\phi - 2\pi f_c t + 2\pi f_0 \tau + \mathrm{Arg}[i q_1^* q_2] \tag{3.12}$$

After that, $\nu(\tau)$ is calculated from the time derivative of ϕ, which can be approximated with a finite time difference:

$$\nu(\tau) = \frac{\dot{\varphi}}{2\pi} = -f_c + \frac{\dot{\delta\phi}(t) - \dot{\delta\phi}(t-\tau)}{2\pi} \tag{3.13}$$

From here, the spectral density of $\nu(\tau)$ measured by a single BPD can be estimated and then used to recover $S_\nu(f)$ with the processing gain from Eq. (3.4). The results with cross-correlation can be further found in Section 3.4.

Resolution bandwidth

To compute $S_\nu(\tau)$ using the Wiener-Khinchin theorem, an infinite length of $\nu(\tau)$ would be required to complete the Fourier transform accurately. Using a limited amount of data leads to a finite resolution bandwidth, which will distort the measured frequency noise. Segmenting the data into shorter sections has a similar effect. Below we derive the modified PSD estimate and the corresponding $G(f)$ for the finite resolution bandwidth case.

In the calculation, $S_\nu(\tau)$ is estimated from the Fourier coefficients of the gated signal:

$$S_{\nu(\tau),\mathrm{gated}}(f) = \frac{|\hat{\nu}_{\mathrm{gated}}(\tau, f)|^2}{\int_{-\infty}^{\infty} w(\tau')^2 \mathrm{d}\tau'} \tag{3.14}$$

where $w(\tau')$ is the window function for gating and $\hat{\nu}_{\mathrm{gated}}(\tau, f)$ is the Fourier coefficient of the gated signal:

$$\hat{\nu}_{\mathrm{gated}}(\tau, f) = \int_{-\infty}^{\infty} \nu(\tau, t = \tau') w(\tau') \exp(2\pi i f \tau') \mathrm{d}\tau' \tag{3.15}$$

Viewing $\nu(\tau)$ as random variables, the expectation of $S_{\nu(\tau),\mathrm{gated}}$ reads

$$\begin{aligned}
\mathrm{E}[S_{\nu(\tau),\mathrm{gated}}(f)] &= \frac{\int_{-\infty}^{\infty}\int_{-\infty}^{\infty} \mathrm{E}[\nu(\tau, t=\tau')\nu(\tau, t=\tau'+\tau'')] w(\tau') w(\tau'+\tau'') \mathrm{e}^{2\pi i f \tau''} \mathrm{d}\tau' \mathrm{d}\tau''}{\int_{-\infty}^{\infty} w(\tau')^2 \mathrm{d}\tau'} \\
&= \frac{\int_{-\infty}^{\infty} \mathrm{d}\tau'' \langle \nu(\tau, 0)\nu(\tau, \tau'')\rangle \, \mathrm{e}^{2\pi i f \tau''} \int_{-\infty}^{\infty} \mathrm{d}\tau' w(\tau') w(\tau'+\tau'')}{\int_{-\infty}^{\infty} w(\tau')^2 \mathrm{d}\tau'} \\
&= \int_{-\infty}^{\infty} \mathrm{d}\tau'' \langle \nu(\tau, 0)\nu(\tau, \tau'')\rangle \, \mathrm{e}^{2\pi i f \tau''} w_2(\tau'') \qquad (3.16) \\
&= \int_{-\infty}^{\infty} S_{\nu(\tau)}(f - f') \hat{w}_2(f') \mathrm{d}f' \qquad (3.17)
\end{aligned}$$

where we introduced $w_2(\tau'')$ as the normalized autocorrelation of w and its associated Fourier transform $\hat{w_2}(f')$:

$$w_2(\tau'') = \frac{\int_{-\infty}^{\infty} w(\tau')w(\tau'+\tau'')\mathrm{d}\tau'}{\int_{-\infty}^{\infty} w(\tau')^2\mathrm{d}\tau'}, \quad w_2(0) = 1 \tag{3.18}$$

$$\hat{w_2}(f') = \int_{-\infty}^{\infty} w_2(\tau'')\exp(2\pi i f'\tau'')\mathrm{d}\tau'' \tag{3.19}$$

From Eq. (3.17), it can be seen that the effect of gating the signal results in convolving $S_{\nu(\tau)}$ with $\hat{w_2}$, which is equivalent to filtering the frequency domain trace of $S_{\nu(\tau)}$ with a response function of w_2 in the time domain from the viewpoint of Eq. (3.16).

To see how this filtering of $S_{\nu(\tau)}$ impacts signal processing, we rewrite Eq. (3.3) as

$$S_{\nu(\tau)}(f) = 4\sin^2(\pi f\tau)S_\nu(f) = [2 - 2\cos(2\pi f\tau)]S_\nu(f) \tag{3.20}$$

If $S_\nu(f)$ varies slowly within the MZI FSR scale $(1/\tau)$, the gating filter only affects the term within the brackets. For the rectangular window used here, w_2 becomes a triangular window, and $S_{\nu(\tau),\mathrm{gated}}$ can be found as

$$S_{\nu(\tau),\mathrm{gated}}(f) \approx [2 - 2(1 - \tau\mathrm{RBW})^+\cos(2\pi f\tau)]S_\nu(f) \tag{3.21}$$

where $z^+ = \max(0, z)$ is the ramp function and RBW is the resolution bandwidth of the rectangular window (equal to the reciprocal of its temporal width). The associated processing gain becomes

$$G_{\mathrm{gated}}(f) = \frac{1}{2 - 2(1 - \tau\mathrm{RBW})^+\cos(2\pi f\tau)} \tag{3.22}$$

We note that the divergence of $G(f)$ is no longer present in Eq. (3.22) for any finite RBW, which can be explained as a spectral leakage of noise from other offset frequencies to integer multiples of MZI FSR. If the RBW is larger than one MZI FSR such that $\tau\mathrm{RBW} > 1$, then Eq. (3.21) and Eq. (3.22) indicate that the fringe pattern is completely averaged out by the filtering. In this case the systems work in the same way as an incoherent detection setup.

Suppression of independent noise with cross-correlation

While the optical signals are converted to RF signal at the BPDs, technical BPD noise (usually characterized by its noise equivalent power) will also be present in the output and is dominant in the current measurement system. This increases the

phase noise of the output and limits the noise floor of the measurement without cross-correlation. We model this technical noise by adding noise terms, $\varphi_{\mathrm{BPD},1}$ and $\varphi_{\mathrm{BPD},2}$, for the extracted phase:

$$\varphi_1 = \varphi + \varphi_{\mathrm{BPD},1}, \quad \varphi_2 = \varphi + \varphi_{\mathrm{BPD},2} \tag{3.23}$$

The noise will be transferred to the frequency signal:

$$\nu_1(\tau) = \nu(\tau) + \nu_{\mathrm{BPD},1}, \quad \nu_2(\tau) = \nu(\tau) + \nu_{\mathrm{BPD},2} \tag{3.24}$$

where $\nu_{\mathrm{BPD},1}$ and $\nu_{\mathrm{BPD},2}$ are the noise terms after time-domain difference. In this case, calculating the Fourier coefficient of $\nu(\tau)$ leads to

$$\hat{\nu}_1(\tau, f) = \int_{-\infty}^{\infty} [\nu(\tau, t = \tau') + \nu_{\mathrm{BPD},1}] w(\tau') \exp(2\pi i f \tau') \mathrm{d}\tau' \tag{3.25}$$

Assuming $\nu(\tau)$ and $\nu_{\mathrm{BPD},1}$ are independent, the calculated PSD for $\nu_1(\tau)$ becomes

$$S_{\nu(\tau),1}(f) = S_{\nu(\tau),\mathrm{gated}}(f) + S_{\mathrm{BPD},1} \tag{3.26}$$

where $S_{\mathrm{BPD},1}$ is the gated PSD for $\nu_{\mathrm{BPD},1}$ noise and determines the measurement floor using only a single BPD.

To remove the BPD technical noise, both BPD outputs are used and cross-correlated to suppress the contribution of $\nu_{\mathrm{BPD},1}$ and $\nu_{\mathrm{BPD},2}$. The correlated estimate of $S_{\nu(\tau)}(f)$ is the product of two Fourier coefficients originating from different BPDs:

$$S_{\nu(\tau),\mathrm{corr}}(f) = \frac{\hat{\nu}_1(\tau, f)\hat{\nu}_2^*(\tau, f)}{\int_{-\infty}^{\infty} w(\tau')^2 \mathrm{d}\tau'} \tag{3.27}$$

Assuming $\nu(\tau)$, $\nu_{\mathrm{BPD},1}$ and $\nu_{\mathrm{BPD},2}$ are all independent, it can be readily shown that

$$\mathrm{E}[S_{\nu(\tau),\mathrm{corr}}(f)] = S_{\nu(\tau),\mathrm{gated}}(f) \tag{3.28}$$

and includes only the contributions from laser noise. However, BPD noise adds randomness to the correlation and increases the variance of $S_{\nu(\tau),\mathrm{corr}}(f)$. This effect will be more obvious at high offset frequencies when technical phase noise from the BPD is converted to larger frequency noise (see Section 4.3), or at low offset frequencies while using a short delay line (where $G(f) \gg 1$). This can be improved by averaging over N segments of data, which lowers the standard error of the mean by $\sqrt{N}$ times and therefore improves the signal-to-noise ratio by $\sqrt{N}$.

3.4 Characterization of the setup

RIN suppression

As noted in Section 3.2, the frequency-shifting process of the self-heterodyne setup effectively isolates RIN from coupling into the measured frequency noise. In order to characterize the RIN suppression performance of the cross-correlator, we measured the RIN conversion ratio with a setup shown in Fig. 3.2(a). The measurement setup consists of an ECL (RIO ORION 1550 nm laser module) modulated by an AOM to generate an artificial RIN signal. The AOM carrier generated from the arbitrary waveform generator is amplitude-modulated by a single-tone sine wave with manually configured frequency and modulation depth. The carrier frequency is selected as the optimal modulation frequency of this AOM (here 55 MHz) to minimize amplitude-phase coupling during the modulation process. By measuring the frequency noise with and without the power modulation using the cross-correlator, the RIN conversion ratio can be determined. The modulation intensity is calculated from the modulation depth and calibrated by tapping 10% of the modulated laser before the cross-correlator. All signals are recorded by the aforementioned high-speed oscilloscope.

Empirically, the RIN conversion to measured frequency noise can be described by

$$\tilde{S}_{\nu(\tau)}(f) = S_{\nu(\tau),\mathrm{corr}}(f) + f^2\alpha \times \mathrm{RIN}(f) \tag{3.29}$$

where $\tilde{S}_{\nu(\tau)}(f)$ is the measured frequency noise just before the processing gain, including RIN contributions, α is a proportionally constant that converts RIN to phase noise, and the extra f^2 factor further converts phase noise to frequency noise. For the reconstructed laser noise the above equation becomes

$$\tilde{S}_{\nu}(f) = S_{\nu}(f) + G(f)f^2\alpha \times \mathrm{RIN}(f) \tag{3.30}$$

The single-tone modulations used in the actual measurements could not be quantified by a spectral density. Instead, the frequency noise intensity can be recovered from

$$P_{\nu}(f_{\mathrm{AM}}) = S_{\nu}(f_{\mathrm{AM}}) \times \mathrm{RBW}(f_{\mathrm{AM}}) \tag{3.31}$$

where f_{AM} is the modulation frequency. Similarly, phase noise intensity is related to the frequency noise intensity by

$$P_{\phi}(f_{\mathrm{AM}}) = \frac{1}{f_{\mathrm{AM}}^2} P_{\nu}(f_{\mathrm{AM}}) \tag{3.32}$$

By comparing $P_{\phi}(f_{\mathrm{AM}})$ against the amplitude modulation intensity, α can be extracted through a linear fitting process.

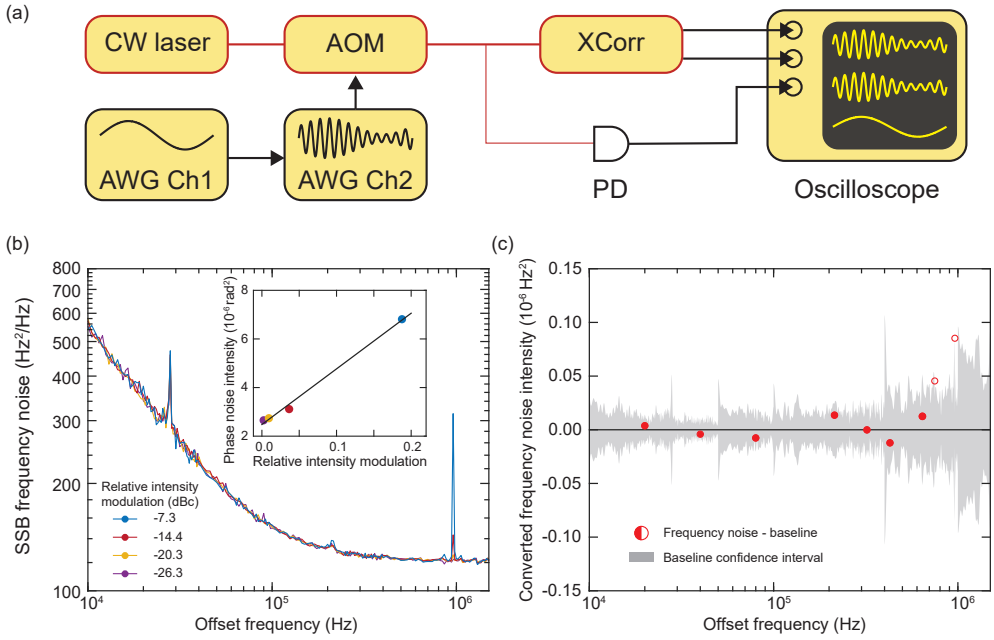

Figure 3.2: **RIN suppression characterization.** **(a)** Experimental setup for RIN suppression characterization. CW laser: continuous wave laser, AOM: acousto-optical modulator, XCorr: cross-correlator [as in Fig. 3.1(a)], AWG: arbitrary waveform generator, PD: photodetector, OSC: oscilloscope. **(b)** SSB laser frequency noise spectra under different modulation intensity at 963 kHz offset frequency. Inset: Phase noise intensity at 963 kHz as a function of modulation intensity. The solid black line is the linear fitting. **(c)** Frequency dependence of RIN conversion ratio. The shaded area stands for the confidence interval (99% confidence probability) of the frequency noise intensity without power modulation. The frequency noise intensity baseline has been subtracted for comparison. The red circles are plotted as the converted frequency noise intensity (measured frequency noise intensity minus baseline) at different offset frequency corresponding to the power modulation frequency. The solid (hollow) circles indicate that the converted frequency noise intensity is inside (outside) the shaded area.

The measured $\tilde{S}_\nu(f)$ under different modulation intensity at 963 kHz offset frequency are shown in Fig. 3.2(b). The noise spurs at 29 kHz come from the ECL itself, which also appear in Fig. 3.5 and Fig. 3.6. The inset of Fig. 3.2(b) shows the linear fitting between the phase noise intensity and the modulation intensity. Here, the RIN to measured laser phase noise conversion ratio $[G(f)\alpha]$ at 963 kHz (i.e., the slope of the fitting) is -46.4 dBrad^2 (2.29 $\times 10^{-5}$ rad^2). From here, α can be found as -40.4 dBrad^2 (9.16 $\times 10^{-5}$ rad^2).

As shown in Fig. 3.2(c), a -20 dBc modulation intensity is selected for all measurements at different modulation frequencies, which is sufficient as an overestimation

for RIN of a normal laser. The intrinsic laser frequency noise may obscure the presence of weakly-coupled RIN, and becomes a noise floor for the RIN conversion measurement. The frequency noise intensity without laser power modulation (i.e., the baseline) is measured 10 times and a 99% possibility confidence interval (shaded area) for the RIN conversion signal is given by assuming that the measured frequency noise intensity is normally distributed. When amplitude modulation is applied, the frequency noise intensity (red circles) at the corresponding offset frequency is calculated and compared with the baseline. A measured intensity outside the confidence interval indicates significant conversion of RIN. RIN conversion has been tested at 20 kHz, 40 kHz, 80 kHz, 214 kHz (equal to the MZI FSR $1/\tau_0$, where τ_0 = 4.67 ms is the delay time of the 1-km-long fiber), 321 kHz, 428 kHz, 642 kHz, 749 kHz, and 963 kHz. The modulation frequencies over 100 kHz match the integer and half-integer multiples of MZI FSR, corresponding to local maximums and minimums of $G(f)$, respectively. The measured frequency noises with artificial RIN coupling only fall outside of the confidence interval at 749 kHz and 963 kHz, which suggests that the RIN suppression is high enough for lasers at offset frequency lower than 1 MHz. We note that the $G(f)$ will amplify the RIN conversion at offset frequencies equal to integer multiples of the MZI FSR. However, as shown by the experimental data, the overall RIN conversion is not important in most cases.

Below we present a model for the origin of RIN coupling by considering signal leakage at the AOM within the cross-correlator [Fig. 3.1(a)]. We assume that a small portion of 0^{th} order light is leaked into the 1^{st} order port at the AOM, which is supported by experimental observations. The net effect is that the amplitude for the frequency-shifted arm should be modified as

$$\begin{aligned}\tilde{A}_1(t) = &\frac{1}{\sqrt{2}}\exp(-2\pi i f_0 t)\exp(2\pi i f_c t)[1+\delta a(t)]\exp[-i\delta\phi(t)] \\ &+\frac{\epsilon}{\sqrt{2}}\exp(-2\pi i f_0 t)[1+\delta a(t)]\exp[-i\delta\phi(t)]\end{aligned} \tag{3.33}$$

where ϵ is a complex number that represents the leakage amplitude. The amplitude on the other arm A_2 remains the same. The BPD power now reads, keeping only the signals oscillating near frequency f_c,

$$\begin{aligned}\Delta\tilde{P} = &2\mathrm{Re}[iq_1^* q_2\exp(2\pi i f_0\tau)\exp(-2\pi i f_c t)(1+\Sigma a)\exp(i\Delta\phi)] \\ &+\mathrm{Re}[\Delta|q|^2\epsilon\exp(-2\pi i f_c t)(1+2\delta a(t))]\end{aligned} \tag{3.34}$$

where the exponential of phase noise is linearized for convenience. The extra term results from the same-arm beating detected at the BPD. The analytic signal is given

by, up to first order of ϵ and $\Delta\phi$,

$$\mathcal{H}\Delta P \approx 2iq_1^* q_2 \exp(2\pi i f_0 \tau) \exp(-2\pi i f_c t) \left[1 + \Sigma a + i\Delta\phi + \frac{\Delta|q|^2|\epsilon|}{|q_1 q_2|} \exp(i\theta_{\mathrm{RIN}}) \left(\frac{1}{2} + \delta a(t)\right)\right] \tag{3.35}$$

Here θ_{RIN} is a phase angle that couples amplitude to phase:

$$\theta_{\mathrm{RIN}} = 2\pi i f_0 \tau + \mathrm{Arg}[\epsilon] - \mathrm{Arg}[iq_1^* q_2] \tag{3.36}$$

Performing phase extraction and time difference leads to

$$\tilde{\nu}(\tau) = \nu(\tau) + \frac{\Delta|q|^2|\epsilon|}{|q_1 q_2|} \sin(\theta_{\mathrm{RIN}}) \frac{\mathrm{d}\delta a}{2\pi \mathrm{d}t} \tag{3.37}$$

For the worst case (maximal coupling) $\sin(\theta_{\mathrm{RIN}}) = \pm 1$, and in the case when laser amplitude and frequency noise are independent, calculating the PSD gives

$$\tilde{S}_{\nu(\tau)}(f) = S_{\nu(\tau),\mathrm{corr}}(f) + f^2 \frac{(\Delta|q|^2)^2|\epsilon|^2}{|q_1|^2|q_2|^2} \frac{\mathrm{RIN}(f)}{4} \tag{3.38}$$

Comparing with the empirical model Eq. (3.29) gives

$$\alpha = \frac{(\Delta|q|^2)^2}{4|q_1|^2|q_2|^2}|\epsilon|^2 \tag{3.39}$$

and is directly proportional to the leaked power at the AOM.

Dynamic range

To quantify the upper limit of noise the COSH setup can measure, we use a DFB laser for characterization. Limited by the laser cavity length and reflectivity of the output facet, the noise of a DFB laser can reach the level of 1 MHz, corresponding to a coherence length shorter than the 1-km-long fiber delay line. However, the measurable noise is not directly related by the delay line, but only limited by the carrier frequency (see below).

Measurement results for a free-running DFB laser are shown in Fig. 3.3(a). The SSB frequency noise of the DFB laser is around 1.2×10^5 Hz^2/Hz at high offset frequencies, corresponding to a 0.75 MHz Lorentzian linewidth and a 267 m coherence length in fiber (assuming a fiber refractive index of 1.5). As the BPD noise is far less than the DFB laser noise, performing cross-correlation on the data provides negligible improvement. Note that the noise peak at 1.2 MHz is from the DFB laser. Combined with the estimate for the noise floor (see Section 4.3), the setup could reach over 70 dB dynamic range for frequency noise measurements.

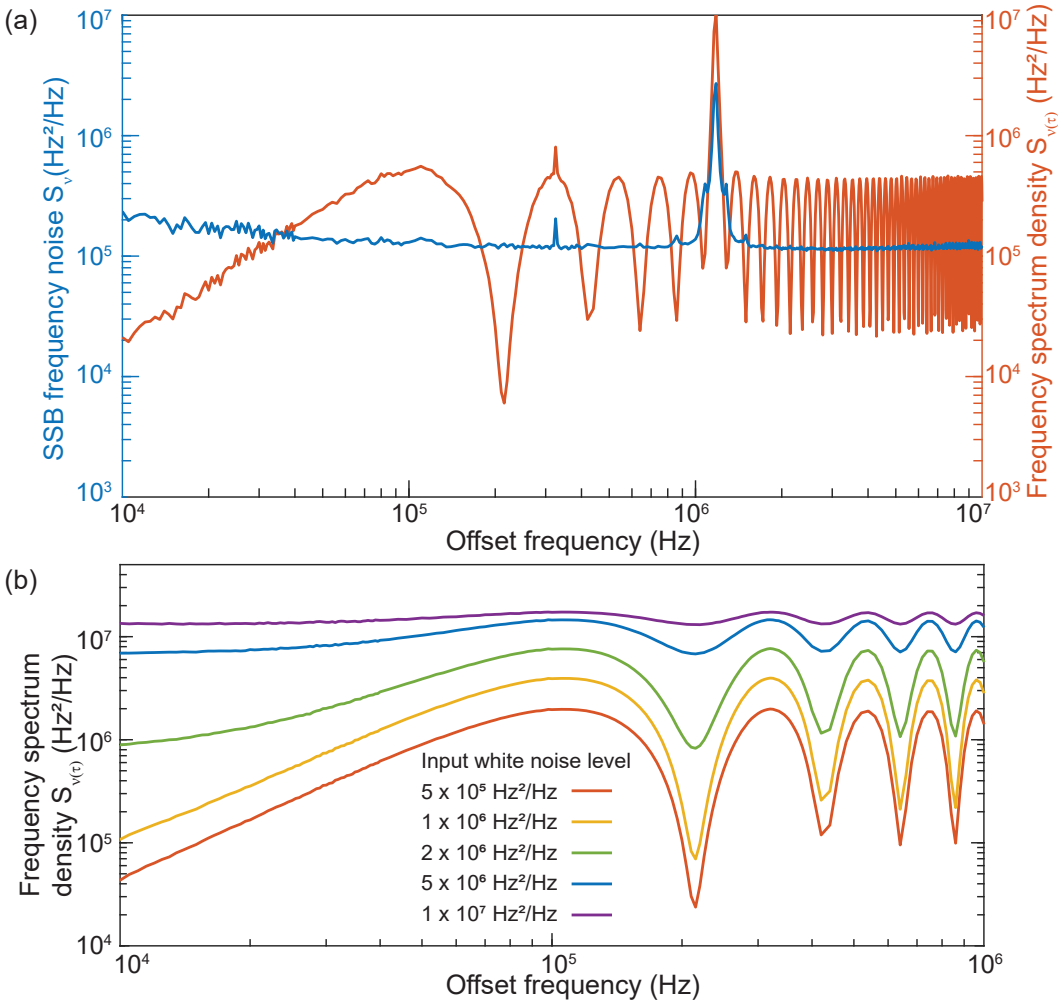

Figure 3.3: **Frequency noise measurement of high-noise laser. (a)** SSB frequency noise and frequency spectral density of a DFB laser. **(b)** Simulated $S_{\nu(\tau)}(f)$ output of the system when a laser with high white frequency noise is used as input. The white noise levels are, from bottom to top: 5×10^5 Hz^2/Hz, 1×10^6 Hz^2/Hz, 2×10^6 Hz^2/Hz, 5×10^6 Hz^2/Hz, 1×10^7 Hz^2/Hz.

To understand how the system behaves for higher laser frequency noise, simulations have been performed and the results are collected in Fig. 3.3(b). Increasing the laser frequency noise above 1×10^6 Hz^2/Hz leads to a visible decrease of fringe contrast before multiplying $G(f)$. This can be attributed to the wide broadening of the carrier signal $\exp(2\pi i f_c t)$. The components that are separated more than f_c from the carrier cross into the negative-frequency domain and will be reflected by the Hilbert transform. If such contributions are significant, Eq. (3.11) is invalidated, and the laser frequency noise can no longer be reliably recovered. Choosing an AOM with higher modulation frequency and increasing the sampling rate for the

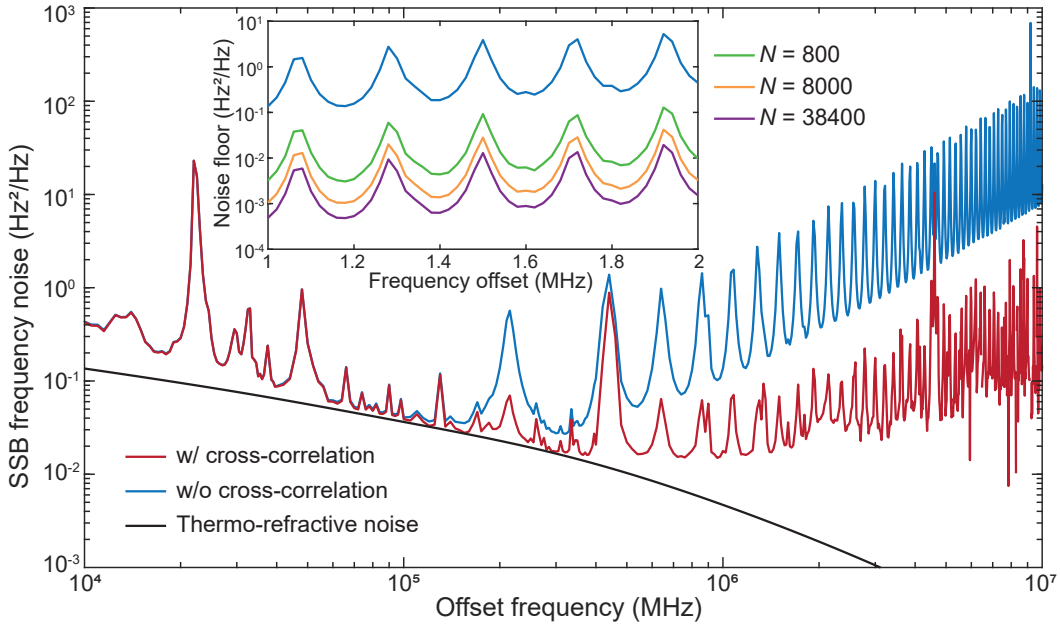

Figure 3.4: **SSB frequency noise of the DFB laser with SIL measured by the self-heterodyne method with and without cross-correlation.** The deviation between them is due to the BPD noise as illustrated in Fig. 3.1. The cross-correlator extracts the common mode SIL laser noise and suppresses the individual BPD noise to reach a 0.01 Hz^2/Hz noise floor at 1 MHz offset frequency. The simulated thermo-refractive noise is plotted in black for comparison. Inset: the measured frequency noise error bar is interpreted as the measurement system noise floor here. With increasing averaging segment number N, the noise floor is reduced by $\sqrt{N}$. The blue trace is the same as the main figure.

oscilloscope could increase the upper noise limit at the expense of measurement time or memory. We note that fringes are still visible even if the noise level exceeds the MZI FSR (i.e. the laser coherent length is shorter than the delay length), unless the resolution bandwidth is chosen to exceed the MZI FSR [as given by $G(f)$].

Noise Floor

Finally, the noise floor of the COSH method is verified using a DFB injection locked to a high-Q resonator. The laser linewidth coming from the compound laser-resonator system can be greatly suppressed (Dahmani, Hollberg, and Drullinger, 1987; Hjelme, Mickelson, and Beausoleil, 1991; Kondratiev et al., 2017) and have demonstrated record linewidth levels in integrated photonics platforms comparable to fiber lasers (B. Li et al., 2021).

Here, the aforementioned DFB laser has been self-injection-locked to a 7-m long,

ultra-high-Q on-chip resonator (with an intrinsic Q factor of 150 million). The SSB frequency noise of this lab-built laser is then measured by the setup and results are shown in Fig. 3.4. Compared with a 1.4-m long spiral resonator (B. Li et al., 2021), larger mode volume further suppresses the thermo-refractive noise (TRN) and reaches 0.041 Hz^2/Hz at 100 kHz offset frequency. The numerically simulated TRN is also plotted for comparison. The lowest measured frequency noise is 0.015 ± 0.002 Hz^2/Hz at 1 MHz offset frequency, comparable with the previous work (B. Li et al., 2021).

The power spectrum density given by a single BPD output frequency without cross-correlation is also illustrated in Fig. 3.1d. Since BPD technical noise is approximately white when characterized as phase noise, the independent BPD noise contribution to measured frequency noise scales as f^2 and is more apparent at high offset frequencies, which is confirmed by comparing the two traces in Fig. 3.4. The spurs in the single-BPD trace are the BPD technical noise amplified by $G(f)$ and are also an indication that the BPD noise has significant contributions. By using cross-correlation and averaging over N segments of data, the noise contribution can be reduced by $\sqrt{N}$. Here, for the 20 kHz resolution bandwidth used for high offset frequencies, we have $N = 38400$, and the signal-to-noise ratio is improved by 22.9 dB. As shown in the inset of Fig. 3.4, the error bar of measured frequency noise (standard deviation of frequency noise from multiple segments) is interpreted as the measurement setup noise floor here, and larger N (proportional to the overall data length used) leads to a lower noise floor. Assuming 0.05 mW optical input power at the BPD, the technical noise is equivalent to 0.10 Hz^2/Hz at 1 MHz offset frequency, consistent with the blue trace in Fig. 3.4 inset. With $N = 38400$, the noise floor with cross-correlation is suppressed to be 0.0005 Hz^2/Hz, consistent with the purple trace in the inset. At MZI FSR frequencies, the noise floor is enhanced but remains below 0.01 Hz^2/Hz around 1 MHz offset frequency. The spurs of measured SSB frequency noise at higher than 1 MHz offset frequency is significantly higher than the noise floor and are believed to originate from the residual RIN amplified by $G(f)$.

3.5 Discussion

Environmental noise coupling

Acoustic noise may be present in the external environment and can couple to the measured SSB frequency noise through the fiber delay of the modified MZI. To minimize environmental perturbations, the optical section of the measurement setup is

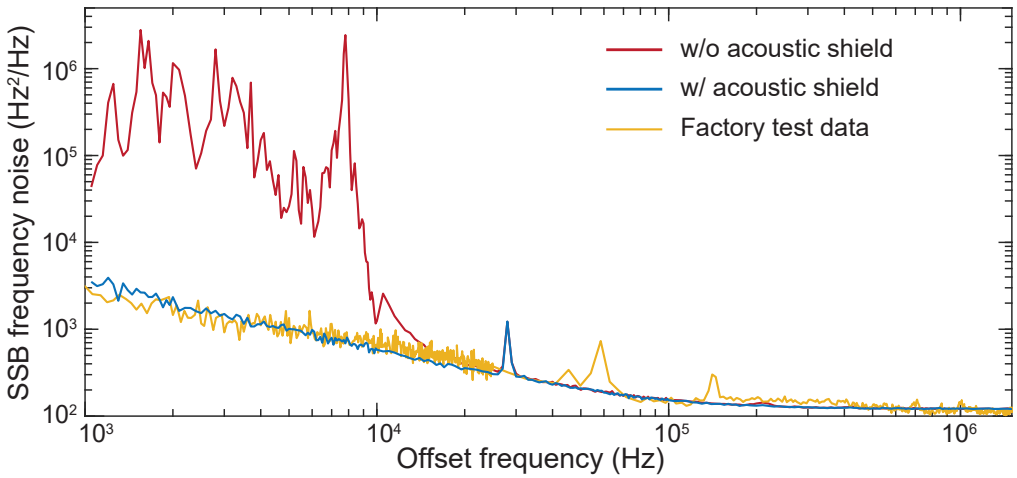

Figure 3.5: **Performance comparison with and without shielding.** Typical SSB frequency noise of a commercial ECL obtained using cross-correlator with/without an acoustic shield. The yellow trace is the test data as provided by the manufacturer.

acoustically shielded with a foam box. To calibrate the external noise isolation from the shield box, we have applied additional acoustic noise in the environment and measured the ECL frequency noise. As is shown in Fig. 3.5, the measured SSB frequency noise is smooth and no peaks can be found below 10 kHz offset frequency, compared to the case without the acoustic shield. Above 10 kHz, the effect of environment noise is not evident for the noise measurement system. Meanwhile, the frequency noise measured with acoustic shield is consistent with the laser manufacturers specification sheet.

Fiber delay length

A major drawback of the current setup is the decrease of sensitivity at integer multiples of MZI FSR, where the frequency noise destructively interferes and $G(f)$ reaches its maximum. These frequencies can be adjusted by changing the fiber delay length. If the destructive interference is undesired over a wide offset frequency range, the fiber delay length should be short enough such that the first MZI FSR appears outside the frequency range. For example, a 10 meter fiber (with MZI FSR equal to approximately 20 MHz) ensures that no fringes appear below 20 MHz offset frequency.

A major disadvantage of using a short fiber delay length is the large systematic error of low-frequency noise. To demonstrate this, the 1 km delay line in the MZI is substituted with a 15 meter fiber and the ECL noise is measured. The results are

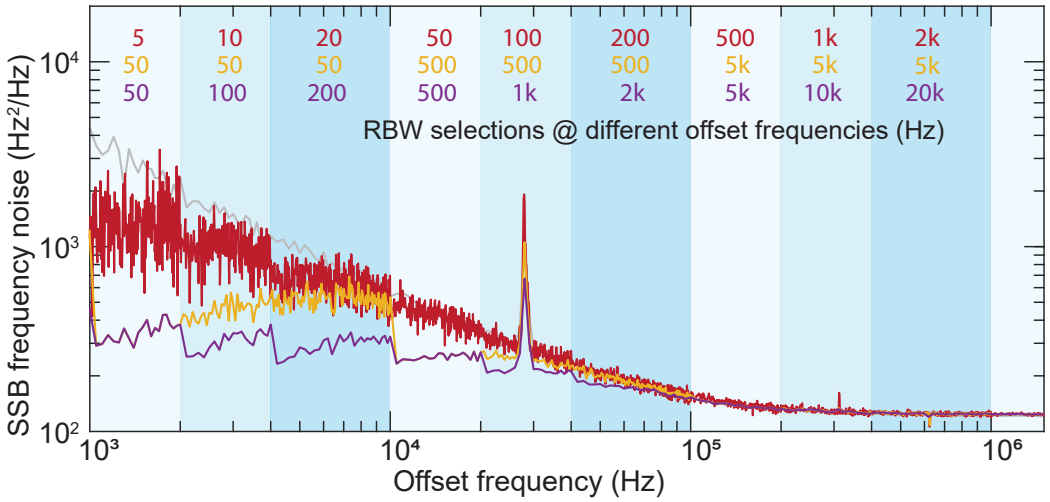

Figure 3.6: **Performance at different RBW configurations.** SSB frequency noise of the ECL calculated with different RBW configurations using 15-meter-long fiber delay line are plotted as red, yellow and purple traces. The RBWs chosen at different offset frequency intervals (marked by shading) are shown at the top with colors in accordance with traces. The gray line using 1-km-long fiber delay line is plotted as a reference and its RBW configurations are the same as the purple trace.

presented in Fig. 3.6. We note that there are frequency noise discontinuities when the RBW changes. For the purple trace in Fig. 3.6, the calculated frequency noise "jumps" at 20 kHz, 40 kHz and 100 kHz, where different RBWs are chosen for the offset frequency intervals on both sides. On the other hand, the data measured using 1 km delay length (grey trace) gives a continuous result and is consistent with the noise data from the laser manufacturers specification sheet.

The strong dependence of calculated noise on the RBW can be attributed to the non-white frequency noise spectrum of the laser. The gating filter acts differently on the spectrum compared to the white case and invalidates Eq. (3.21). By using smaller RBWs, the calculated noise becomes closer to the true laser noise, as seen from the red trace in Fig. 3.6.

3.6 Conclusion

In this paper we have demonstrated a correlated self-heterodyne (COSH) method to measure laser frequency noise with 0.01 Hz^2/Hz noise floor and high RIN rejection quantified by the coupling coefficient $\alpha = -40.4$ $dBrad^2$. Commercial ECL and DFB lasers with/without self-injection-locking are used to verify the performance. The cross-correlation noise floor is limited by the coupled RIN amplified by the

processing gain $G(f)$ as well as residual BPD technical noise.

The setup described here can be further reconfigured to meet specific measurement requirements. For example, the RIN suppression can be further enhanced by using an AOM with higher 0^{th} order to 1^{st} order isolation. Temperature controllers can be installed to the 50/50 couplers to adjust the coupling ratio precisely and balance the MZI arms. On the other hand, if the expected laser noise frequency is high, then cross-correlation is not necessary and the memory depth of the oscilloscope can be decreased accordingly. A conventional PD can be used in place of a BPD if RIN is not a concern. Overall, the specific measurement setup and parameters introduced in Section 2.1 are targeted towards ultra-low-noise laser measurement mainly at high offset frequencies, while the basic principle remains universal.

References

Bartlett, Maurice S (1948). "Smoothing periodograms from time-series with continuous spectra." In: *Nature* 161.4096, pp. 686–687.

Dahmani, B, L Hollberg, and R Drullinger (1987). "Frequency stabilization of semiconductor lasers by resonant optical feedback." In: *Opt. Lett.* 12.11, pp. 876–878.

Hjelme, Dag Roar, Alan Rolf Mickelson, and Raymond G Beausoleil (1991). "Semiconductor laser stabilization by external optical feedback." In: *IEEE J. Quantum Electron.* 27.3, pp. 352–372.

Kondratiev, NM et al. (2017). "Self-injection locking of a laser diode to a high-Q WGM microresonator." In: *Opt. Express* 25.23, pp. 28167–28178.

Lai, Yu-Hung et al. (2020). "Earth rotation measured by a chip-scale ring laser gyroscope." In: *Nature Photonics* 14.6, pp. 345–349.

Lee, Hansuek et al. (2012). "Chemically etched ultrahigh-Q wedge-resonator on a silicon chip." In: *Nature Photonics* 6.6, pp. 369–373.

Li, Bohan et al. (2021). "Reaching fiber-laser coherence in integrated photonics." In: *Optics Letters* 46.20, pp. 5201–5204.

Li, Jiang et al. (2012). "Characterization of a high coherence, Brillouin microcavity laser on silicon." In: *Optics Express* 20.18, pp. 20170–20180.

Ludvigsen, Hanne, Mika Tossavainen, and Matti Kaivola (1998). "Laser linewidth measurements using self-homodyne detection with short delay." In: *Optics Communications* 155.1-3, pp. 180–186.

Newman, Zachary L, Vincent Maurice, Tara Drake, et al. (2019). "Architecture for the photonic integration of an optical atomic clock." In: *Optica* 6.5, pp. 680–685.

Schumaker, Bonny L (1984). “Noise in homodyne detection.” In: *Optics Letters* 9.5, pp. 189–191.

Suh, Myoung-Gyun and Kerry J Vahala (2018). “Soliton microcomb range measurement.” In: *Science* 359.6378, pp. 884–887.

Tran, Minh et al. (2021). “Extending the spectrum of fully integrated photonics.” In: *arXiv preprint arXiv:2112.02923*.

Van Exter, MP, SJM Kuppens, and JP Woerdman (1992). “Excess phase noise in self-heterodyne detection.” In: *IEEE Journal of Quantum Electronics* 28.3, pp. 580–584.

Walls, Warren F (1992). “Cross-correlation phase noise measurements.” In: *Proceedings of the 1992 IEEE Frequency Control Symposium*. IEEE, pp. 257–261.

Xie, Xiaopeng et al. (2017). “Phase noise characterization of sub-hertz linewidth lasers via digital cross correlation.” In: *Optics Letters* 42.7, pp. 1217–1220.

Chapter 4

HIGH-COHERENCE 780 NM SOURCE BY SELF-INJECTION-LOCKED SECOND-HARMONIC GENERATION

4.1 Introduction

[1] By self-injection-locking a 1560 nm distributed feedback semiconductor laser to a high-Q silicon nitride resonator, a high-coherence 780 nm second harmonic signal is generated via the photogalvanic-induced second-order nonlinearity. A record-low frequency noise floor of 4 Hz^2/Hz is achieved for the 780 nm emission. The approach can be generalized for signal generation over a wide range of visible and near-visible bands. Highly coherent visible laser sources play a crucial role in the operation of optical atomic clocks (Ludlow et al., 2015), automotive LiDAR (Hecht, 2018), and sensing systems (Degen, Reinhard, and Cappellaro, 2017). However, existing bench-top visible lasers are both costly and bulky, limiting their use beyond laboratory environments including application in future navigation and sensing systems. To address this challenge, we generate visible light in a high-Q silicon nitride microcavity that is hybridly-integrated to a semiconductor laser operating in the near-infrared band. The cavity both line narrows the laser through self-injection-locking (SIL) (Jin et al., 2021; Li et al., 2021) and generates the high-coherence visible signal as a second-harmonic (SH) signal by way of the photogalvanic field-induced second-order nonlinearity (Lu et al., 2021) and the all-optical-poling effect (Billat et al., 2017; Hickstein et al., 2019; Nitiss et al., 2022) in Si_3N_4. Frequency noise is reduced by 100-fold compared with previous integrated visible lasers (Siddharth et al., 2022; Corato-Zanarella et al., 2023; Ling et al., 2023; Franken et al., 2021). The approach can be readily tuned to any visible or near-visible band.

4.2 Device geometry

The resonator is fabricated using the ultra-low-loss silicon-nitride photonic platform (Jin et al., 2021; Puckett and al, 2021) with a 100 nm thick silicon nitride waveguide

[1] Work presented in this chapter has been published in "High-coherence hybrid-integrated 780 nm source by self-injection-locked second-harmonic generation in a high-Q silicon-nitride resonator", *Optica* 10 (9), 1241-1244.

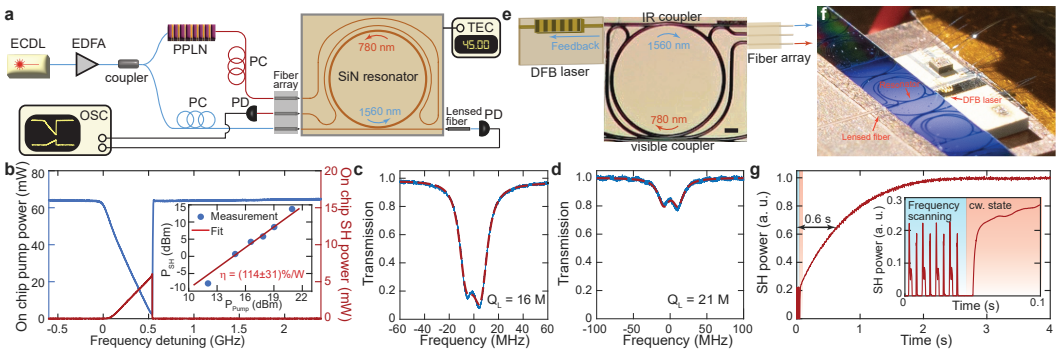

Figure 4.1: **Experimental setups and characterization of the Si_3N_4 resonator and SH generation performance.** **(a)** Experimental setup used to determine the phase matching condition and characterize the SH performance of the Si_3N_4 resonator. ECDL, external cavity diode lasers; EDFA, Erbium-doped fiber amplifier; PPLN, periodically poled lithium niobate; PC, polarization controller; PD, photodiode; OSC, oscilloscope; TEC, thermoelectric cooler. **(b)** Measured on-chip transmission pump power (left axis) and generated SH power (right axis) when scanning the frequency of a tunable laser across a cavity resonance at the phase matching condition. Inset: measured on-chip SH power (blue dots) plotted versus pump power levels. The frequency conversion efficiency is fit by the red line with a slope of 2. Within our measurement range, the SHG efficiency is found to be constant. **(c, d)** Transmission spectra of the pump resonance at 1560.1 nm (c) and the SH resonance at 780.05 nm (d). The experimental measurements are plotted in blue and the theoretical fittings are plotted in red. Each resonance exhibits backscatter-induced splitting. The leakage of 1560 nm light into 780 nm pulley coupler and the multimode nature of 780 nm waveguide make determination of the intrinsic (i.e., ring-only) Q factors of the 1560 nm and 780 nm modes difficult (see Appendix). **(e)** Schematic of the hybrid-integrated frequency conversion laser, where a DFB laser is endfire-coupled to a high-Q silicon-nitride microresonator to provide feedback to the laser. The upper and lower waveguides are designed for coupling at 1560 nm and 780 nm, respectively. The scale bar is 200 μm. **(f)** Photograph of the hybrid-integrated frequency conversion laser in panel (e). **(g)** The time response of the SH power after the DFB laser frequency is stopped at the operation point. **Inset**: zoom-in of the main plot. Prior to fixing the DFB laser frequency, the pump laser frequency is scanned and SH power changes periodically during frequency scanning (blue region). When the scanning is stopped, SH power builds to steady state (red region).

core and a 2.2 μm thick silica top cladding. The resonator has a 5 μm waveguide width and a 850 μm radius. Two pulley couplers are designed for efficient coupling at both the near-infrared and visible bands. The near-infrared coupler has a 2.3 μm waveguide width with a 3.5 μm gap that is designed to prevent coupling to the visible mode. The visible coupler has a 1.6 μm waveguide width with a 0.3 μm gap

that is designed to reduce coupling to the near-infrared mode.

4.3 Second harmonic generation

The resonator is first characterized using the experimental setup shown in Fig. 4.1a. A 4-channel fiber array and a lensed fiber are used to couple to near-infrared and visible resonances simultaneously. To probe the resonances, the output of a near-infrared tunable laser is split with one output doubled in frequency using a periodically-poled lithium niobate (PPLN) crystal. In this way, first and second harmonic probe waves are generated to characterize resonator spectra in these bands. Because the photogalvanic effect induces optical poling to thereby establish the quasi-phase-matching condition (Nitiss et al., 2022), a visible mode having twice the pumping frequency will achieve SH generation regardless of its propagation constant. To establish this condition, the Si_3N_4 chip is temperature controlled to tune the mode spectra. Tuning over no more than one free-spectral-range is sufficient, and in the current setup a chip temperature of 45 °C aligns the pump resonance at 1560.1 nm with a visible resonance at 780.05 nm. Photogalvanic-induced second-harmonic generation can be readily observed when scanning the pump laser across the near-infrared resonance, as shown in Fig. 4.1b. Continuous-wave SH power measurements with the pump laser frequency fixed at the cavity resonance are shown in the inset of Fig. 4.1b. The SH conversion efficiency is estimated to be 114±31%W (average over measured powers) and SH output power as high as 24 mW is measured (in the bus waveguide). The loaded Q factors of the pump and SH modes are determined by transmission spectra measurements shown in Fig. 4.1c,d.

4.4 Self-injection-locking and frequency noise measurement

To achieve a high coherence visible light source in a compact foot print, we replace the bulk tunable laser with a distributed-feedback (DFB) chip laser as shown in the experimental setup in Fig. 4.1e,f. The DFB laser is endfire-coupled to the silicon-nitride chip and can deliver 20 mW pump power to the resonator waveguide (accounting for 6 dB facet coupling loss). Backscatter-induced feedback from the resonator to the laser provides self-injection-locking that dramatically reduces the laser frequency noise (Jin et al., 2021; Li et al., 2021). Upon current tuning the DFB laser frequency into the 1560.1 nm resonance, the optical poling process is initialized through the field-induced photogalvanic effect. This process can be monitored by scanning the frequency of the DFB laser around the resonance by modulating the

pump current with a function generator. The SH signal produced during forward and backward scanning is shown in the inset of Fig. 4.1g (blue region). The function generator is then turned off, and the DFB frequency self-locks into the resonance center. The resulting SH signal time evolution is shown over short time interval in the inset of Fig. 4.1g (red region) and over several seconds in the main panel. The SH power build-up features a 0.6s rise time and takes only a few seconds to reach steady state. In steady-state operation, the SH power at 780 nm reaches over 0.5 mW on-chip as monitored via a lensed fiber (12dB coupling loss).

The SIL 1560 nm light and SH generated 780 nm light are then further analyzed to determine their frequency noise performance (Fig. 4.2a). The SH signal is sent to a delayed self-homodyne detection setup with quadrature-point locking (Lee et al., 2012) and its measured frequency noise is shown as the red trace in Fig. 4.2b. The peak at 18 kHz offset in the spectrum is due to the feedback loop response of a fiber stretcher used to maintain the quadrature point. At high offset frequencies, the photodetector (PD) white noise is suppressed using a cross-correlation technique (Walls, 1992; Yuan et al., 2022), and achieves 4 Hz^2/Hz noise floor above 6 MHz offset frequency, corresponding to a record-low 25 Hz instantaneous linewidth for visible on-chip sources. The frequency noise of the self-injection locked pump laser is characterized with a self-heterodyne approach (Yuan et al., 2022), and the result is shown as the blue curve in Fig. 4.2. Compared with the free-running DFB laser noise (gray trace), the SIL process suppresses the noise by 40 (32) dB at 100 kHz (1 MHz) offset frequency. The generated SH laser noise is 4 times higher than the SIL pump laser noise due to coherent photon conversion (Ling et al., 2023). Specifically, the phase fluctuation of the pump field is doubled in the SH signal through the squaring of the pumping field. The corresponding SH spectral density function therefore experiences a factor of 4 increase (6 dB) relative to the pump. The difference in these spectra at high offset frequencies is due to spontaneous emission noise in the 1560 nm signal resulting from its measurement at the transmission port of the coupled resonator system.

High intra-cavity photon density and resonant backscattering make this system prone to Kerr frequency comb generation (Jin et al., 2021). SIL comb formation is governed by feedback phase and frequency detuning (Shen et al., 2020; Lihachev et al., 2022), and these parameters also provide a way to favor single mode lasing over comb generation. In the present device the laser-to-chip gap (feedback phase) and pump current (frequency detuning) provide useful controls. The latter is illustrated

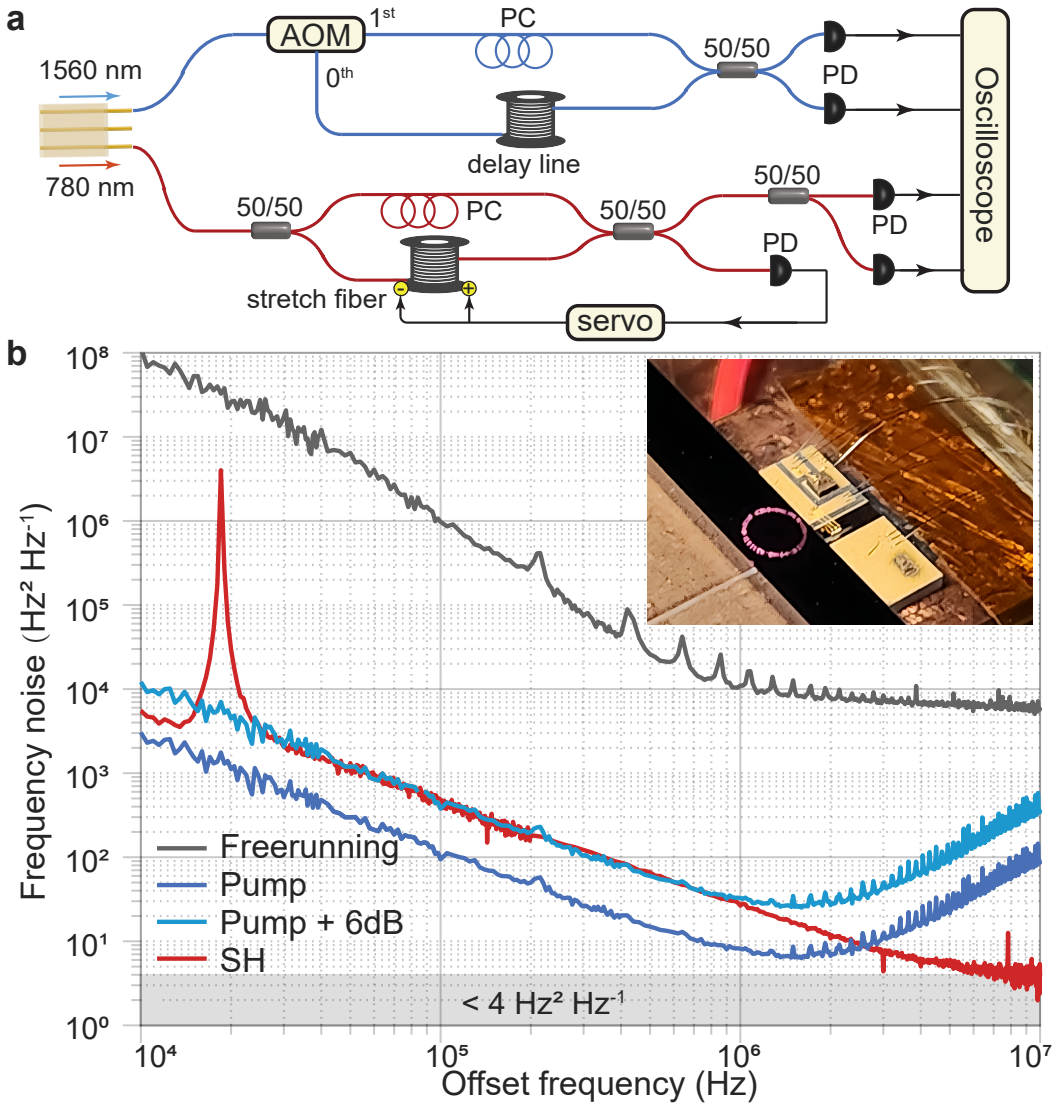

Figure 4.2: **Frequency noise measurement for SIL pump laser and generated SH laser.** **(a)** Frequency noise measurement setups for both the SIL 1560nm laser and the SH 780 nm laser. AOM, acousto-optic modulator. **(b)** Measured single-sideband frequency noise spectrum. Gray, blue and red traces show the frequency noise spectra of the free-running DFB signal, SIL pump signal (1560 nm), and SH signal (780 nm), respectively. The light blue trace shows the SIL pump laser frequency noise up-shifted by 6 dB. The inset is a photograph of the device under operation with 780 nm emission visible on the ring resonator.

in Fig. 4.3a where the transmitted pumping power and the SH power are plotted versus DFB laser current scan. Distinct regimes where the single-frequency SIL state and the comb state appear are indicated. In the comb state, only the pump comb line can be frequency doubled due to phase matching condition so that the

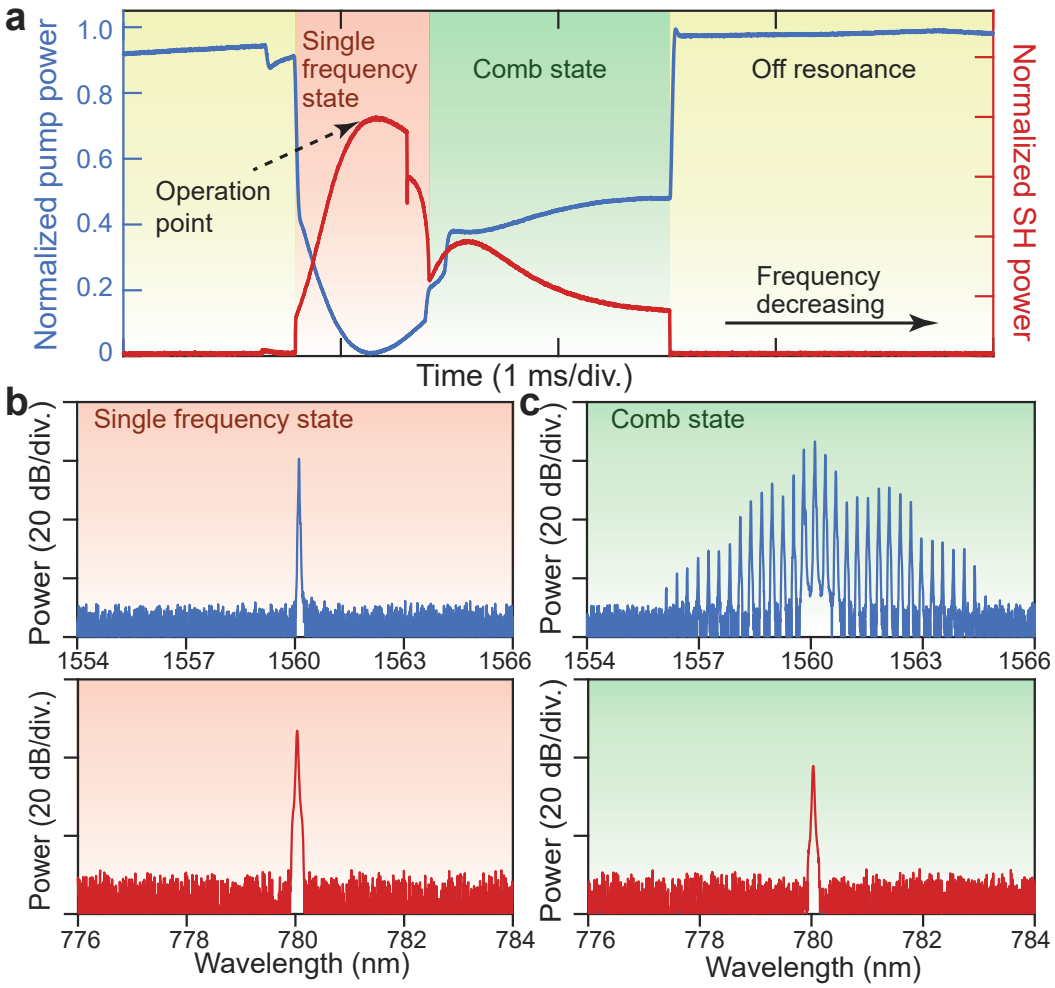

Figure 4.3: **Self-injection locked laser response with pump current induced frequency tuning. (a)** The measured SIL pump power (blue) and second harmonic power (red) when the pump current is scanned across the resonance. When the DFB laser frequency is tuned into the cavity resonance, the near infrared laser is initially in a single frequency state and eventually tunes to a comb state. **(b, c)** Upper panels: Measured optical spectra of the near infrared laser in the single frequency state (b) and comb state (c). Lower panels: corresponding SH 780 nm spectra.

generated SH power is reduced. The operation point used in the previous power and noise measurements is indicated. Typical SH spectra in the two regimes are shown in Fig. 4.3b,c. Reduced SH power is apparent for the comb state since intracavity pump power is reduced by comb formation.

4.5 Discussion

In conclusion, we have demonstrated a record-low 4 Hz^2/Hz frequency noise floor for a hybrid-integrated visible light source by self-injection-locking a DFB laser

with a high-Q Si_3N_4 resonator. The III-IV laser and the silicon nitride resonator can be readily heterogeneously integrated using the integration technique described in ref. (Xiang et al., 2023). The current resonator intrinsic Q factor is not optimal, and based on prior work could exceed 250M at 1560nm (Jin et al., 2021). This should further reduce frequency noise levels since the SIL noise reduction scales as Q^2 (Kondratiev et al., 2017). This scaling makes generation of highly coherent signals easier in the near-IR where optical Qs are overall much higher. The SH-SIL process therefore extends this advantage into the visible bands. Finally, the photogalvanic effect makes access to other wavelengths straightforward. Devices require only waveguide couplers designed for efficient visible and near infrared operation.

Appendix: coupler design principle

The 1560 nm pulley coupler waveguide width is chosen to achieve phase matching to the ring resonator fundamental eigenmode. The coupler occupies an effective arc length of about 0.1 radian of the resonator with a 3.5 μm minimum gap. This gap is too large to achieve significant interaction with the 780 nm eigenmode thereby reducing parasitic coupling of the 780 nm mode to the 1560 nm coupler.

The 1.6um width of the 780 nm pulley coupler waveguide is approximately phase-matched to the TE10 higher-order mode of the resonator. This substantially phase mismatches the coupler to the fundamental resonator eigenmode at 1560 nm, thereby suppressing parasitic coupling of the 1560 nm mode. The coupler gap is narrow (minimum 0.3 μm) and to further minimize perturbation to the 1560 nm mode, the gap is adiabatically reduced using the arc of an archimedian spiral. This however results in a coupler arc-length exceeding 1 radian, so that 780 nm optical power might undergo several coupling oscillations over the length of the coupler.

Some parasitic coupling of the 1560 nm light to the 780 nm coupler is expected. This parasitic loss channel contributes to the intrinsic Q factor of the resonator at 1560 nm. And spectral measurements of the intrinsic Q factor around 1560 nm reveal an oscillatory dependence (see Fig. 4.4) that is believed to result from this dependence.

References

Billat, Adrien et al. (2017). “Large second harmonic generation enhancement in Si3N4 waveguides by all-optically induced quasi-phase-matching.” In: *Nature communications* 8.1, p. 1016.

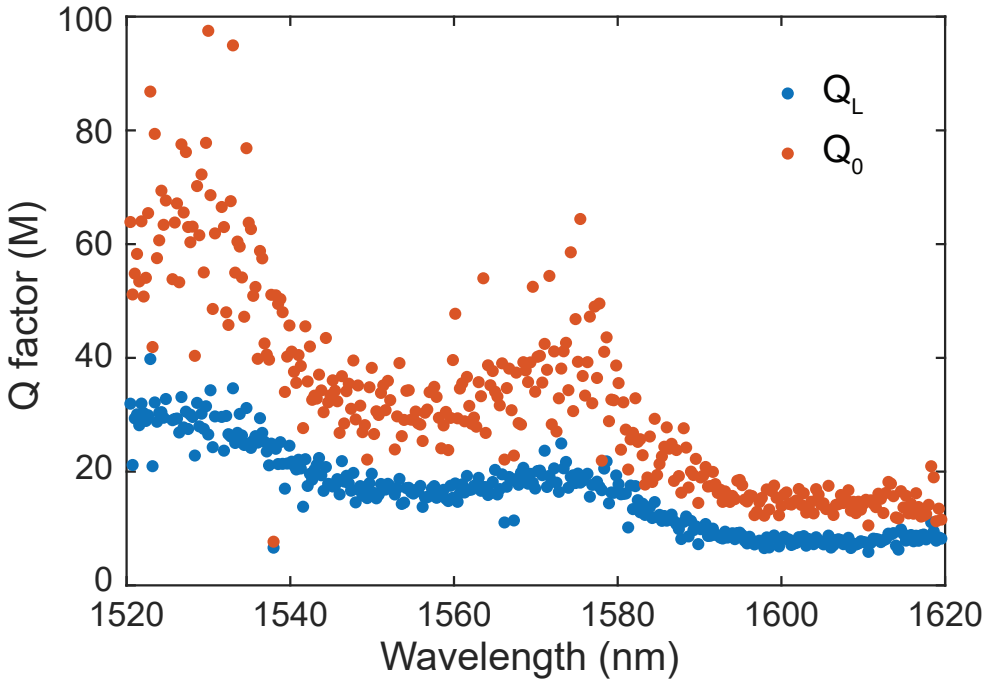

Figure 4.4: **Resonator loaded and intrinsic Q factor measurements plotted versus wavelength.** The spectral peaks in measured intrinsic Q factors are believed to originate from the wavelength-dependent coupling of 1560 nm light to the 780 nm pulley coupler.

Corato-Zanarella, Mateus et al. (2023). "Widely tunable and narrow-linewidth chip-scale lasers from near-ultraviolet to near-infrared wavelengths." In: *Nature Photonics* 17.2, pp. 157–164.

Degen, Christian L, Friedemann Reinhard, and Paola Cappellaro (2017). "Quantum sensing." In: *Reviews of Modern Physics* 89.3, p. 035002.

Franken, Cornelis AA et al. (2021). "Hybrid-integrated diode laser in the visible spectral range." In: *Optics letters* 46.19, pp. 4904–4907.

Hecht, Jeff (2018). "Lidar for self-driving cars." In: *Optics and Photonics News* 29.1, pp. 26–33.

Hickstein, Daniel D et al. (2019). "Self-organized nonlinear gratings for ultrafast nanophotonics." In: *Nature Photonics* 13.7, pp. 494–499.

Jin, Warren et al. (2021). "Hertz-linewidth semiconductor lasers using CMOS-ready ultra-high-Q microresonators." In: *Nat. Photon.* 15.5, pp. 346–353.

Kondratiev, NM et al. (2017). "Self-injection locking of a laser diode to a high-Q WGM microresonator." In: *Opt. Express* 25.23, pp. 28167–28178.

Lee, Hansuek et al. (2012). "Chemically etched ultrahigh-Q wedge-resonator on a silicon chip." In: *Nature Photonics* 6.6, pp. 369–373.

Li, Bohan et al. (2021). “Reaching fiber-laser coherence in integrated photonics.” In: *Optics Letters* 46.20, pp. 5201–5204.

Lihachev, Grigory et al. (2022). “Platicon microcomb generation using laser self-injection locking.” In: *Nature Communications* 13.1, p. 1771.

Ling, Jingwei et al. (2023). “Self-Injection Locked Frequency Conversion Laser.” In: *Laser & Photonics Reviews*, p. 2200663.

Lu, Xiyuan et al. (2021). “Efficient photoinduced second-harmonic generation in silicon nitride photonics.” In: *Nature Photonics* 15.2, pp. 131–136.

Ludlow, Andrew D et al. (2015). “Optical atomic clocks.” In: *Reviews of Modern Physics* 87.2, p. 637.

Nitiss, Edgars et al. (2022). “Optically reconfigurable quasi-phase-matching in silicon nitride microresonators.” In: *Nature Photonics* 16.2, pp. 134–141.

Puckett, M. and et al (2021). “422 Million intrinsic quality factor planar integrated all-waveguide resonator with sub-MHz linewidth.” In: *Nature communications* 12, p. 934.

Shen, Boqiang et al. (2020). “Integrated turnkey soliton microcombs.” In: *Nature* 582.7812, pp. 365–369.

Siddharth, Anat et al. (2022). “Near ultraviolet photonic integrated lasers based on silicon nitride.” In: *Apl Photonics* 7.4, p. 046108.

Walls, Warren F (1992). “Cross-correlation phase noise measurements.” In: *Proceedings of the 1992 IEEE Frequency Control Symposium*. IEEE, pp. 257–261.

Xiang, Chao et al. (2023). “3D integration enables ultralow-noise isolator-free lasers in silicon photonics.” In: *Nature* 620.7972, pp. 78–85.

Yuan, Zhiquan et al. (2022). “Correlated self-heterodyne method for ultra-low-noise laser linewidth measurements.” In: *Optics Express* 30.14, pp. 25147–25161.

Chapter 5

EFFICIENT AND WAVELENGTH-TUNABLE SECOND-HARMONIC GENERATION TOWARDS THE GREEN GAP

5.1 Introduction

[1]Teaser: Tunable, efficient green light is generated by frequency doubling infrared light in a high-Q Si3N4 microresonator.

Achieving compact and efficient visible laser sources is crucial for a wide range of applications. However traditional semiconductor laser technology faces difficulties in producing high-brightness green light, leaving a "green gap" in wavelength coverage. Second-harmonic generation (SHG) offers a promising alternative by converting near-infrared sources to visible wavelengths with high efficiency and spectral purity. Here, we demonstrate efficient and tunable SHG within the green spectrum using a high-Q Si_3N_4 microresonator. On chip green power as high as 5.3 mW is generated with a conversion efficiency of 141%/W (absolute 7.9%). A space-charge grating induced by the photogalvanic effect realizes reconfigurable grating numbers and flexible wavelength tuning over a range of 2.6 THz. Additionally, grating formation dynamics and competition is observed. These findings underscore the potential of Si_3N_4 as a robust, integrative platform for on-chip, tunable green light sources.

The development of compact, coherent visible laser sources is key to a range of applications in both science and engineering, including optical clocks (Ludlow et al., 2015), biomedical imaging (Luke et al., 2019), quantum information processing (Wendin, 2017), and laser displays (Chellappan, Erden, and Urey, 2010). However, it is challenging to create green light with high brightness and efficiency from traditional semiconductor laser technologies due to material limitations and low quantum efficiency (Moustakas and Paiella, 2017). This issue is commonly referred to as the "green gap" (Pleasants, 2013), a wavelength span around 500 – 550 nm. Dye lasers based on organic molecules offer wide wavelength tunability. However, like other traditional bench-top solutions, they are bulky and complex, limiting

[1]Work presented in this chapter has been published in "Efficient and wavelength-tunable second-harmonic generation toward the green gap", *Science Advances* 11 (27), eadw2781.

their use in compact applications (Schäfer, 2013). Also, quantum dot lasers have high tunable range and are suitable for on-chip integration, but still suffer from low efficiency and coherence at the green gap (Mei et al., 2017; C. Zhao et al., 2020).

Nonlinear optical phenomena in high-Q resonators provide another approach for achieving new wavelengths (Kerry J Vahala, 2003). For instance, optical parametric oscillation (OPO) based on four-wave mixing (FMW) in microresonators (Kippenberg, Spillane, and K. Vahala, 2004; Savchenkov et al., 2004) has been extensively studied in recent years (Sayson et al., 2019; X. Lu, Moille, et al., 2020; Domeneguetti et al., 2021), and enables access to the green gap (Sun et al., 2024). Alternatively, green light generation has been reported by third-harmonic generation (Carmon and Kerry J Vahala, 2007; Levy et al., 2011; Surya et al., 2018) and cascaded sum frequency generation (Ling, Staffa, L. Wu, et al., 2022), but with limited efficiency. In contrast, second-harmonic generation (SHG), offers high conversion efficiency and coherence by frequency-doubling from near-infrared sources (Bruch et al., 2018; J.-Y. Chen et al., 2019; J. Lu, Surya, et al., 2019; J. Lu, Ming Li, et al., 2020; Ling, Staffa, H. Wang, et al., 2023; Yan et al., 2023; H. Chen et al., 2025). Among various photonic platforms for SHG, Si_3N_4 is particularly promising due to its ultra-low optical loss, CMOS compatibility and suitability for nonlinear optics. And recently, photogalvanic effect induced second order nonlinearity has been observed in Si_3N_4 with efficient SHG (Puckett, Sharma, et al., 2016; Billat et al., 2017; X. Lu, Moille, et al., 2021; Nitiss et al., 2022; B. Li et al., 2023).

In this work, we leverage a thin-film, ultra-low-loss Si_3N_4 (W. Jin et al., 2021) to achieve efficient SHG in the green spectral range. By employing a carefully designed coupler to minimize leakage loss, we demonstrate a broadband high-Q region and strong green emission with high coherence (see Fig. 5.1A). In the photogalvanic-induced quasi-phase-matching process, optically induced space-charge gratings are reconfigurable, enabling robust, dynamically tunable SHG in real time. Furthermore, we observe dynamic grating competition during space-charge formation. The tunability, combined with the maturity of Si_3N_4 as a platform for photonic integration, positions this system as an ideal candidate for versatile, on-chip green laser sources.

5.2 Device characterization

The device is fabricated based on an ultra-low-loss Si_3N_4 platform (W. Jin et al., 2021; Puckett, Liu, et al., 2021). The Si_3N_4 resonator waveguide core is a 5-μm

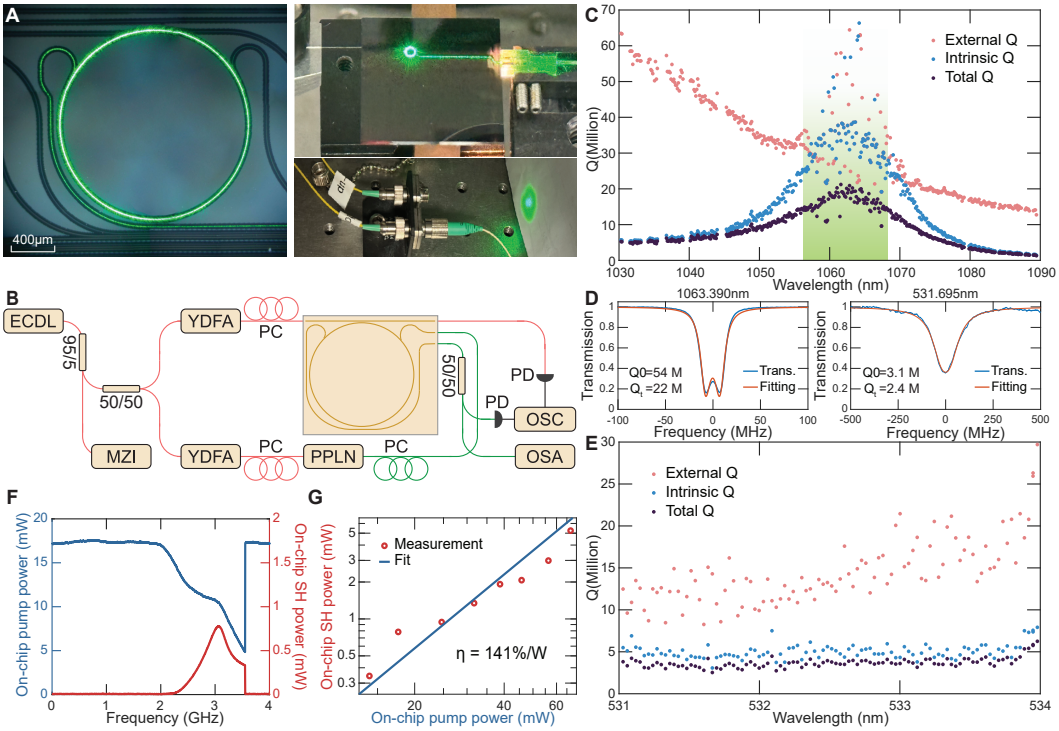

Figure 5.1: **Device characterization and SHG performance of the Si_3N_4 microresonator.** **A** Photographs of the ring resonator and off-chip green light emission during SHG operation. **B** Experimental setup for frequency-matching tuning and SHG performance characterization of the Si_3N_4 microresonator. The chip temperature is controlled and stabilized by a thermoelectric cooler (not shown). Abbreviations: ECDL, external cavity diode lasers; MZI, Mach–Zehnder interferometer; YDFA, Ytterbium-doped fiber amplifier; PPLN, periodically poled lithium niobate; PC, polarization controller; PD, photodetector; OSC, oscilloscope; OSA, optical spectrum analyzer. **C** Measured quality (Q) factor distribution versus wavelength from 1030 nm to 1090 nm, with the designed high-Q band highlighted in green. **D** Transmission spectrum and fitting of the pump resonance at 1064 and 532 nm. **E** Measured Q factor distribution versus the wavelength from 531 nm to 534 nm. **F** On-chip transmission of pump power (left axis) and SHG power (right axis) during pump laser frequency scanning across a cavity resonance at the phase-matching condition. **G** On-chip SHG power (red dots) versus pump power. The frequency conversion efficiency is fit by the blue line with a slope of two, indicating a constant SHG efficiency (η, in %/W) within the measured range.

wide by 50-nm thick design with an upper-cladding of 2.2-μm thick silica. The design has a radius of 850 μm, corresponding to a free-spectral-range (FSR) of 36.61 GHz at 1064 nm. To facilitate efficient coupling in both the near-infrared (near-IR) and visible bands, the design incorporates two pulley couplers (see Fig. 5.1A) for spectral partitioning. The upper coupler, with a 3.5 μm gap, enables

injection of the near-IR pump laser while minimizing coupling to the visible (green) mode, and the lower coupler, with a 0.3 μm gap, efficiently extracts the SHG signal while reducing the leakage of the near-IR mode.

The microresonator is characterized using the setup illustrated in Fig. 5.1B. A 1064 nm tunable laser is split into two beams. One beam serves as the probe wave for the fundamental near-IR modes and provides the pump power for SHG, while the other beam is amplified and frequency-doubled by a periodically poled lithium niobate (PPLN) crystal to probe the green resonances. A four-channel V-groove array (VGA) and a lensed fiber are used for simultaneous coupling to both the near-infrared and green waveguides.

The quality factor distribution in the near-IR band is first measured using a calibrated Mach–Zehnder interferometer (MZI) in combination with a wavelength-tunable laser(Yi et al., 2015). A main contribution to optical loss in the near-IR band is optical leakage through the visible coupler. And accordingly, the visible coupler was designed to minimize near-IR loss around the 1064 nm pumping wavelength. As shown in Fig. 5.1C, the measured Q distribution is maximal around this design target where, within a 12 nm bandwidth, the total Q factor exceeds 15 million (highlighted in green). The scatter in the Q data in this region is an artifact of measurement near the critical coupling point. Additionally, we characterize the Q distribution of the green modes by scanning the pump frequency while simultaneous tuning the PPLN crystal temperature to maintain sufficient SHG probe power (Fig. 5.1E). Within the measurement range, the green modes are undercoupled and their total Q factors are clustered around 3 million, which shows the low absorption loss of the material (Corato-Zanarella et al., 2024; Morin et al., 2021).

In the photogalvanic process, a space-charge grating creates a field that works with the existing Kerr effect to create an effective second-order nonlinearity. The grating also ensures quasi-phase-matching by compensating for the phase difference between fundamental and SHG fields (Nitiss et al., 2022). Therefore, only the frequency matching condition is necessary, where the frequency of the visible mode is required to be twice of the fundamental field. To accomplish this, chip temperature is tuned to align green and near-IR modes. During this process, the green resonance is monitored by PPLN doubling of the pump laser. It is worth noting that even without an external green probe signal, the near-IR pump light alone is sufficient to generate a weak seed signal, enabling the grating formation. The long-lived electron traps ensure that the space-charge grating remains stable over multiple days without

decrease in SHG efficiency (Billat et al., 2017).

At a chip temperature of 25.0 °C, a pump resonance (1063.390 nm) aligns with a visible resonance (531.695 nm), and photogalvanic-induced SHG occurs automatically. The Q factors of the pump and SHG modes are shown in Fig. 5.1D. When 17 mW input pump laser is launched into the waveguide and scanned across the near-infrared resonance, SHG power as high as 0.78 mW is generated on chip, corresponding to an efficiency of 250 %/W (Fig. 5.1F). For the same resonance, the on-chip SHG power is also measured versus pump power in Fig. 5.1G, with a conversion efficiency of 141 %/W averaged over input power levels. The SHG power reaches 5.3 mW in the bus waveguide at the input power of 67 mW (absolute efficiency of 7.9%). The green probe signal is turned off during this measurement. Based on the measured SHG efficiency and quality factors, the effective $\chi^{(2)}$ is estimated to be 0.022 pm/V. However, we note that the calculation of effective $\chi^{(2)}$ involves multiple assumptions, and certain parameters may vary. As a result, there are substantial uncertainties in this estimate.

5.3 Wavelength tunability

Concerning tuning of the emission, suppose at chip temperature T_0, a one-to-one frequency matching condition is satisfied, where a SHG mode $m_{2\omega}$ is frequency matched with the pump mode m_ω, $f(m_{2\omega}) = 2f(m_\omega)$ (as shown in Fig. 5.2A). Since the green and near-IR modes have different local FSRs and resonant frequency tuning coefficients ($\delta f/\delta T$) near these two modes, the frequency mismatch between the next pair of modes ($m_{2\omega}+2$ and $m_\omega+1$) can be compensated through a reduction in chip temperature by $\Delta T = \frac{2\mathrm{FSR}(m_{2\omega})-2\mathrm{FSR}(m_\omega)}{\delta f/\delta T(m_{2\omega})-2\delta f/\delta T(m_\omega)}$. This process can be cascaded to achieve multiple frequency-matched output wavelengths, with a constant optical-poling-induced grating number ($m_{\text{green}} - 2m_{\text{near-IR}}$) . The tuning mechanism is illustrated by multiple frequency matching conditions within a group of the same grating number (Fig. 5.2A), with each group corresponding to a single color in panel B. And tuning range is limited by the chip temperature range, which is kept between 17 °C and 60 °C, allowing a 0.6 nm wavelength change in the green by steps of 0.1 nm.

Unlike non-centrosymmetric materials poled by high-voltage electrical pulses, where the resonator grating number is fixed during fabrication, the photogalvanic process allows for reconfigurable grating structures due to optically-induced space-charge distribution (Nitiss et al., 2022). Accordingly, and in contrast to the above tuning

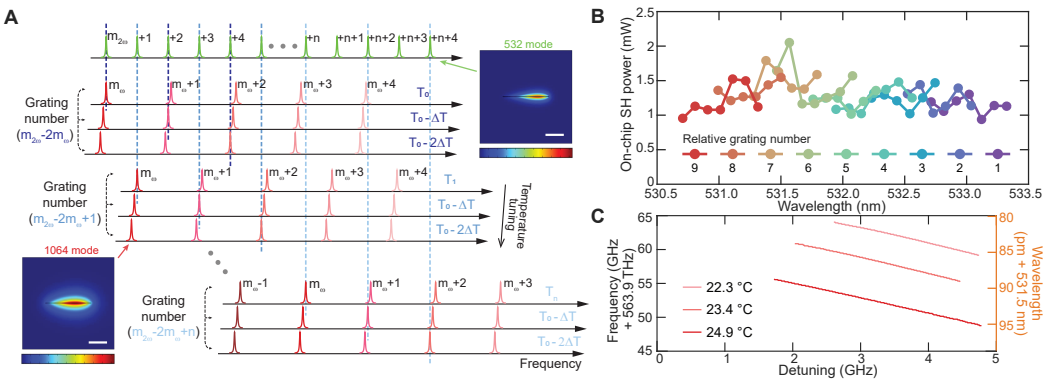

Figure 5.2: **Coarse and fine wavelength tuning in green SHG. A** Illustration of the multiple frequency matching condition in the SHG process for coarse tuning control. The first row shows multiple longitudinal modes of the fundamental TE mode family in the green spectral region. Subsequent rows display the longitudinal modes of the fundamental TE mode at 1.06 μm, with different SHG frequency-matching conditions (dashed lines) at the corresponding cavity temperatures. Within each group, the grating number ($m_{\text{green}} - 2m_{\text{near-IR}}$) of the photogalvanic space-charge field remains constant. Inset: cross-sectional view of simulated mode profiles at the green SHG mode and near-IR pump mode, respectively. The scale bar represents 2 μm. **B** Experimental measurements of the generated SHG wavelengths at different matching conditions. The y-axis represents indicate the on-chip SHG power, and the colors indicate the grating number difference between the pump and SHG modes. **C** Measured output green light frequencies are plotted versus the laser-cavity detuning at three different cavity temperatures for the same pump-SHG mode pair. The on-chip pump power is 78 mW. Continuous tuning is available at each point in 2B, and this panel shows a representative example.

process, the pump mode m_ω can be matched to adjacent green modes (temperature tuning), such as $m_{2\omega} + 1$ (second group in Fig. 5.2A) by adjusting the temperature. In this case, $T_1 - T_0 = \frac{\text{FSR}(m_{2\omega})}{2\delta f/\delta T(m_\omega) - \delta f/\delta T(m_{2\omega})}$. This process enables matching a single pump mode to multiple green modes, creating new colors in Fig. 5.2B. All experimentally measured on-chip SHG powers at different frequency matching conditions are plotted versus wavelength and categorized by the relative grating number. The OSA spectrum of each generated green signal is used to determine the SHG wavelength and on-chip SHG power, and the on-chip pump power is maintained at 39 mW. At the same chip temperature, increasing the relative grating number shifts the matching wavelength toward shorter wavelengths. The wide high-Q distribution at both wavelengths enables a maximum tunability of 2.6 nm (2.6 THz) with nearly constant SHG efficiency and minimum on-chip SHG power around 1 mW. Importantly, there is no fundamental limit to the SHG wavelength tuning range, and

the only restriction comes from the PPLN crystal used to probe the mode resonance frequencies.

Finally we also demonstrate the continuous fine tuning of the SHG wavelength by adjusting the pump laser frequency (laser-cavity detuning) within a single matching point in panel B. Due to the OSA's resolution limit, a wavemeter [HighFinesse GmbH, WS6-600] is utilized to record the green light with 0.1 pm resolution. As shown in Fig. 5.2C, at 24.9 °C the SHG signal emerges when the laser-cavity detuning reaches 1.8 GHz. The SHG frequency then decreases at twice the rate of the detuning as it continues to increase, with the laser sweeping out of the cavity mode when the detuning reaches 4.8 GHz. When the chip temperature is slightly adjusted while maintaining the frequency matching condition, the cavity resonances also shift, thereby shifting the green light wavelength. By selecting three cavity temperatures, the output frequency can be continuously tuned by 16 GHz, which means each data point in Fig. 5.2B can occupy a width of 16 pm.

5.4 Vernier matching and grating competition

Due to different local FSRs of modes at 532 nm (32.15 GHz) and 1064 nm (36.61 GHz), a Vernier frequency matching condition is also available. This allows alignment of mode pairs with different grating numbers at the same temperature. Following the method used in Fig. 5.1C and 5.1E, we measured the frequency dispersion of the modes in both the green and near-IR spectral bands simultaneously (shown in Fig. 5.3A). At a resonator temperature of 43.8 °C, two distinct SHG alignments are observed at 1064.135 nm / 532.069 nm and 1065.658 nm / 532.829 nm. These are indicated by the blue (mode 1) and red (mode 2) arrows, respectively. The aligned modes are separated by 25 (11) modes in the green (near-IR) band, consistent with the FSR values previously measured ($32.15 / 36.61 \approx 22 / 25$).

To distinguish the green light generated by each of the two modes, a counter-propagating (CP) pump setup is employed (Fig. 5.3B). Here, two pump lasers are amplified and directed through circulators, generating two on-chip counter-propagating SHG signals. These signals are detected independently using photodetectors connected to the two output ports of the VGA. When a single pump laser is coupled into the resonator, SHG occurs automatically upon adjusting the pump wavelengths to match both resonances. The output green light spectra are shown in Fig. 5.3C. At this specific temperature, mode 2 achieves perfect frequency matching, while mode 1 has a slight residual misalignment (see panel a), resulting in higher

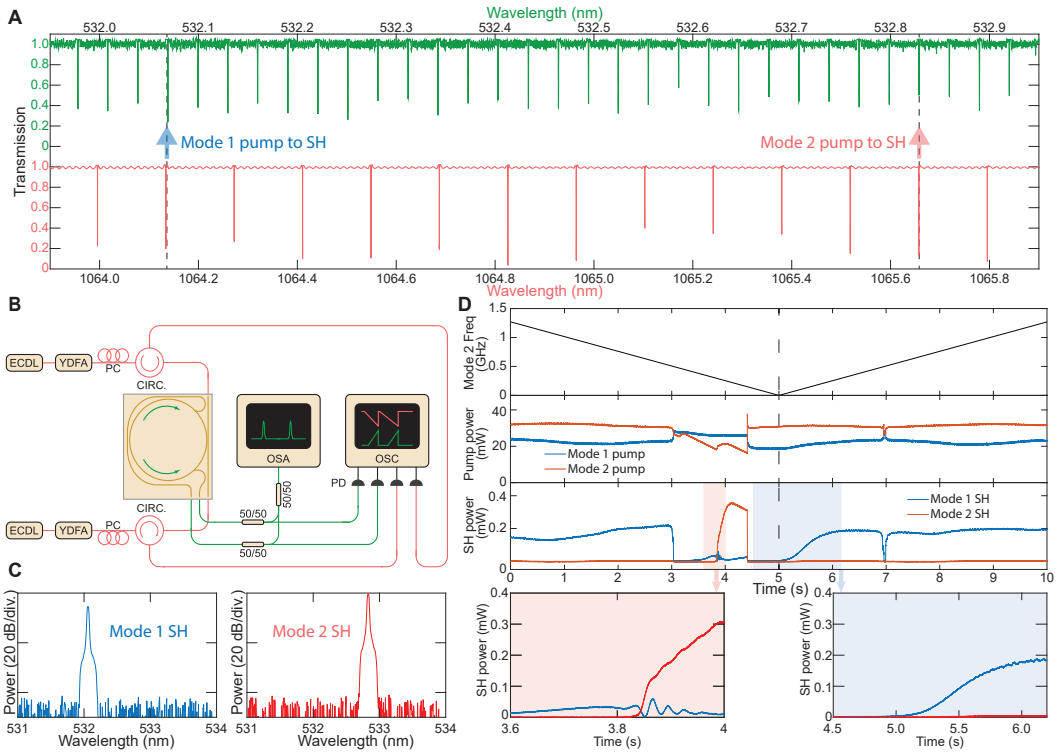

Figure 5.3: **Vernier matching between green and near-IR modes and observation of grating competition dynamics. A** Simultaneously measured frequencies of the mode families in green (green) and near-IR (red) bands are plotted versus wavelength at chip temperature 43.8 °C. Vernier frequency matching is observed due to spectrally local FSR differences. Red and blue arrows indicate the positions of two distinct modes used for second-harmonic generation (SHG). SH: second-harmonic. **B** Experimental setup for counter-pumped SHG at two distinct wavelengths (mode 1 and mode 2 in panel **A**). **C** Optical spectrum of the independently generated green light from two distinct pairs of modes. **D** Observation of the grating competition dynamics between two pairs of modes with different space charge grating numbers. The pump frequency of mode 2 is scanned periodically while the pump frequency of mode 1 is unchanged and in resonance. Top trace: the frequency change of the mode 2 pump laser during scanning; middle trace: the transmitted on-chip pump power during scanning; bottom trace: the corresponding generated on-chip SHG power. Lower panel insets: zoom-in views of the corresponding shaded regions of the bottom trace, showing the grating built-up and erasure process.

output power for mode 2.

The SHG process arises from photogalvanic-induced grating poling, where the SHG signal follows the formation of the corresponding grating in the microresonator. However, since these two green light signals originate from the same transverse mode family but differ in grating numbers, they produce unique electron distributions

within the material. And this introduces grating competition during the formation process of each grating.

To investigate the dynamics of this grating competition, we apply a 0.1 Hz ramp signal to gradually scan the pump laser frequency relative to mode 2, while keeping the mode 1 pump laser in resonance and fixed. In the first 5 seconds, the mode 2 pump laser frequency gradually shifts from blue to red, scanning from outside of mode 2, entering its resonance, and then moving out again. During the next 5 seconds, it reverses direction, scanning from red to blue across the mode 2 resonance. This frequency scan path is depicted in the top trace of Fig. 5.3D, with the corresponding transmitted pump power and SHG power on-chip displayed in the middle and bottom traces. At the beginning, the mode 1 pump laser is tuned into the mode 1 resonance, establishing the grating structure for mode 1 and enabling SHG. As the mode 2 pump frequency gradually scans into resonance, the SHG power from mode 2 increases while the SHG power from mode 1 decreases (zoom-in in the left inset). This observation indicates the formation of the grating for mode 2 and the erasure of the mode 1 grating, leading to a brief overlap where both green lights coexist. Fluctuations in mode 1 SHG power are attributed to interference induced by backscattering from mode 2. The grating formation for mode 2 occurs within a second, consistent with previous observations (B. Li et al., 2023). Notably, the abrupt drop in mode 1 SH power at $t = 3$ s results from a sudden loss of pump power due to thermal competition, while the gradual decrease after $t = 3.8$ s indicates grating reformation, accompanied by an increase in mode 2 SH power. This highlights the contrast in timescales between two processes: grating formation develops over seconds, whereas thermal effects manifest within milliseconds.

When the mode 2 pump laser scans out of resonance, it no longer influences the grating structure, allowing the mode 1 pump laser to re-establish resonance and rebuild its grating. Since the grating for mode 2 has already been formed, mode 1 SHG power does not regenerate immediately but instead increases gradually as the mode 1 grating is rebuilt and mode 2's grating neutralizes (right inset of Fig. 5.3D). The observed relaxation time between the formation of the two gratings reflects the timescale associated with dynamic switching between modes. Mode 1's grating takes longer to regenerate due to the slight mode misalignment.

For comparison, at $t = 7$ seconds, mode 1 SHG power drops as the mode 2 pump laser scans into resonance from the red side and change the cavity temperature. However, this brief resonance does not last long enough to create a new grating or

fully erase the existing one, so mode 1 SHG power quickly returns after the mode 2 laser exits resonance.

5.5 Discussion

In summary, we have demonstrated efficient and tunable second-harmonic generation in Si_3N_4 microresonators within the green spectral range. By leveraging photogalvanic induced quasi-phase-matching, robust second-harmonic generation was achieved with precise control over multiple frequency-matched modes. Table 5.1 summarizes the key metrics of this work and previous works for green light generation in integrated platforms. The high quality factors for both green and near-IR modes highlights the potential of Si_3N_4 microresonators for high-efficiency, stable performance across different frequency bands. The observed grating competition between SHG modes further reveals the dynamic behavior of photonic grating formation, suggesting avenues for more advanced control, including dynamic mode-switching.

The results presented here offer several key advantages, including a wide transparency window, ultra-high quality factors, compatibility with CMOS photonic integration, and excellent power handling capabilities. Si_3N_4 has demonstrated impressive capability for broader photonic integration, including heterogeneous and hybrid integration with active components such as III-V semiconductor lasers (Komljenovic et al., 2015; Xiang et al., 2021; Moss et al., 2013; Dutt et al., 2015; Stern et al., 2018; X. Lu, Q. Li, et al., 2019; Snigirev et al., 2023). Commercially available distributed Bragg reflector (DBR) laser diodes operating in the 1 μm band can deliver over 200 mW of output power. If hybridly-integrated with the device demonstrated in this work, these lasers are expected to generate more than 10 mW of on-chip green light. Towards practical applications, maintaining long-term performance necessitates precise thermal management and optimized mechanical coupling to ensure stability and efficiency. Additionally, the all-optical poling method does not require lithographically-defined electrodes and subsequent poling with high-voltage electrical pulses. On the other hand, traditional $\chi^{(2)}$ materials, such as PPLN, provide larger $\chi^{(2)}$ nonlinearity, making them ideal for applications requiring efficient SHG at low input power levels. Nonetheless, the achievable power in Si_3N_4 SHG can be notably enhanced by utilizing higher-order modes for perfect phase matching (X. Lu, Moille, et al., 2021) and also through further boost in optical Q factors. Also, broadband SHG can be achieved through careful resonator design (Clementi et al., 2024). With their high efficiency and photonic integration

compatibility, this work shows that Si_3N_4 microresonators are promising candidates for on-chip tunable coherent green sources.

Table 5.1: **Comparison of state-of-the-art green light generation in integrated platforms**

Work	Process	Material	Tunability	λ_{Pump}	λ_{Green}	Pump power	Green power	Normalized efficiency	Max absolute efficiency
This work	SHG	Si_3N_4	2.6 THz	1064 nm	532 nm	67 mW	5.3 mW	141 %/W	7.90%
Ref. (Sun et al., 2024)	OPO	Si_3N_4	70 THz	766.2-778.8 nm	535-612 nm	50 mW	100-500 μW	20 %/W	1%
Ref. (Surya et al., 2018)	THG	AlN/ Si_3N_4	Not shown	1542 nm	514 nm	30 mW	49 μW	180 %/W^2	0.16%
Ref. (Ling, Staffa, L. Wu, et al., 2022)	Cascaded SHG+SFG	Lithium Niobate	Not shown	1560 nm	520 nm	54 mW	334 μW	12000 %/W^2	0.60%
Ref. (Yan et al., 2023)	Cascaded SHG+SFG	Lithium Niobate	Not shown	1550 nm	517 nm	20 mW	2 μW	152 %/W^2/cm^2	0.01%
Ref. (H. Chen et al., 2025)	SHG	Lithium Tantalate	0.2 THz	1064 nm	532 nm	16 mW	1.87 mW	1290 %/W/cm^2	11.7%

References

Billat, Adrien et al. (2017). "Large second harmonic generation enhancement in Si3N4 waveguides by all-optically induced quasi-phase-matching." In: *Nature communications* 8.1, p. 1016.

Bruch, Alexander W et al. (2018). "17 000%/W second-harmonic conversion efficiency in single-crystalline aluminum nitride microresonators." In: *Applied Physics Letters* 113.13.

Carmon, Tal and Kerry J Vahala (2007). "Visible continuous emission from a silica microphotonic device by third-harmonic generation." In: *Nature Physics* 3.6, pp. 430–435.

Chellappan, Kishore V, Erdem Erden, and Hakan Urey (2010). "Laser-based displays: a review." In: *Applied optics* 49.25, F79–F98.

Chen, Haiwei et al. (2025). "Continuous-wave second-harmonic generation of green light in periodically poled thin-film lithium tantalate." In: *Optics Letters* 50.4, pp. 1125–1127.

Chen, Jia-Yang et al. (2019). "Ultra-efficient frequency conversion in quasi-phase-matched lithium niobate microrings." In: *Optica* 6.9, pp. 1244–1245.

Clementi, Marco et al. (2024). "Ultrabroadband Resonant Frequency Doubling on a Chip." In: *arXiv preprint arXiv:2412.03322*.

Corato-Zanarella, Mateus et al. (2024). "Absorption and scattering limits of silicon nitride integrated photonics in the visible spectrum." In: *Optics Express* 32.4, pp. 5718–5728.

Domeneguetti, Renato R et al. (2021). "Parametric sideband generation in CMOS-compatible oscillators from visible to telecom wavelengths." In: *Optica* 8.3, pp. 316–322.

Dutt, Avik et al. (2015). “On-chip optical squeezing.” In: *Physical Review Applied* 3.4, p. 044005.

Jin, Warren et al. (2021). “Hertz-linewidth semiconductor lasers using CMOS-ready ultra-high-Q microresonators.” In: *Nat. Photon.* 15.5, pp. 346–353.

Kippenberg, TJ, SM Spillane, and KJ Vahala (2004). “Kerr-nonlinearity optical parametric oscillation in an ultrahigh-Q toroid microcavity.” In: *Physical review letters* 93.8, p. 083904.

Komljenovic, Tin et al. (2015). “Heterogeneous silicon photonic integrated circuits.” In: *Journal of Lightwave Technology* 34.1, pp. 20–35.

Levy, Jacob S et al. (2011). “Harmonic generation in silicon nitride ring resonators.” In: *Optics express* 19.12, pp. 11415–11421.

Li, Bohan et al. (2023). “High-coherence hybrid-integrated 780 nm source by self-injection-locked second-harmonic generation in a high-Q silicon-nitride resonator.” In: *Optica* 10.9, pp. 1241–1244.

Ling, Jingwei, Jeremy Staffa, Heming Wang, et al. (2023). “Self-Injection Locked Frequency Conversion Laser.” In: *Laser & Photonics Reviews*, p. 2200663.

Ling, Jingwei, Jeremy Staffa, Lue Wu, et al. (2022). “Third-harmonic generation on chip through cascaded χ (2) processes.” In: *CLEO: Science and Innovations*. Optica Publishing Group, SF4G–3.

Lu, Juanjuan, Ming Li, et al. (2020). “Toward 1% single-photon anharmonicity with periodically poled lithium niobate microring resonators.” In: *Optica* 7.12, pp. 1654–1659.

Lu, Juanjuan, Joshua B Surya, et al. (2019). “Periodically poled thin-film lithium niobate microring resonators with a second-harmonic generation efficiency of 250,000%/W.” In: *Optica* 6.12, pp. 1455–1460.

Lu, Xiyuan, Qing Li, et al. (2019). “Chip-integrated visible–telecom entangled photon pair source for quantum communication.” In: *Nature physics* 15.4, pp. 373–381.

Lu, Xiyuan, Gregory Moille, et al. (2020). “On-chip optical parametric oscillation into the visible: generating red, orange, yellow, and green from a near-infrared pump.” In: *Optica* 7.10, pp. 1417–1425.

– (2021). “Efficient photoinduced second-harmonic generation in silicon nitride photonics.” In: *Nature Photonics* 15.2, pp. 131–136.

Ludlow, Andrew D et al. (2015). “Optical atomic clocks.” In: *Reviews of Modern Physics* 87.2, p. 637.

Luke, Alexander Maninagat et al. (2019). “Lasers: A review with their applications in oral medicine.” In: *Journal of lasers in medical sciences* 10.4, p. 324.

Mei, Yang et al. (2017). “Quantum dot vertical-cavity surface-emitting lasers covering the ‘green gap’.” In: *Light: Science & Applications* 6.1, e16199–e16199.

Morin, Theodore J et al. (2021). “CMOS-foundry-based blue and violet photonics.” In: *Optica* 8.5, pp. 755–756.

Moss, David J et al. (2013). “New CMOS-compatible platforms based on silicon nitride and Hydex for nonlinear optics.” In: *Nature photonics* 7.8, pp. 597–607.

Moustakas, Theodore D and Roberto Paiella (2017). “Optoelectronic device physics and technology of nitride semiconductors from the UV to the terahertz.” In: *Reports on Progress in Physics* 80.10, p. 106501.

Nitiss, Edgars et al. (2022). “Optically reconfigurable quasi-phase-matching in silicon nitride microresonators.” In: *Nature Photonics* 16.2, pp. 134–141.

Pleasants, Simon (2013). “Overcoming the’green gap’.” In: *Nature Photonics* 7.8, pp. 585–585.

Puckett, Matthew W, Kaikai Liu, et al. (2021). “422 Million intrinsic quality factor planar integrated all-waveguide resonator with sub-MHz linewidth.” In: *Nat. Commun.* 12.1, pp. 1–8.

Puckett, Matthew W, Rajat Sharma, et al. (2016). “Observation of second-harmonic generation in silicon nitride waveguides through bulk nonlinearities.” In: *Optics Express* 24.15, pp. 16923–16933.

Savchenkov, Anatoliy A et al. (2004). “Low Threshold Optical Oscillations in a Whispering Gallery Mode C a F 2 Resonator.” In: *Physical review letters* 93.24, p. 243905.

Sayson, Noel Lito B et al. (2019). “Octave-spanning tunable parametric oscillation in crystalline Kerr microresonators.” In: *Nature Photonics* 13.10, pp. 701–706.

Schäfer, Fritz Peter (2013). *Dye lasers*. Vol. 1. Springer Science & Business Media.

Snigirev, Viacheslav et al. (2023). “Ultrafast tunable lasers using lithium niobate integrated photonics.” In: *Nature* 615.7952, pp. 411–417.

Stern, Brian et al. (2018). “Battery-operated integrated frequency comb generator.” In: *Nature* 562.7727, pp. 401–405.

Sun, Yi et al. (2024). “Advancing on-chip Kerr optical parametric oscillation towards coherent applications covering the green gap.” In: *Light: Science & Applications* 13.1, p. 201.

Surya, Joshua B et al. (2018). “Efficient third-harmonic generation in composite aluminum nitride/silicon nitride microrings.” In: *Optica* 5.2, pp. 103–108.

Vahala, Kerry J (2003). “Optical microcavities.” In: *nature* 424.6950, pp. 839–846.

Wendin, Göran (2017). “Quantum information processing with superconducting circuits: a review.” In: *Reports on Progress in Physics* 80.10, p. 106001.

Xiang, Chao et al. (2021). “Laser soliton microcombs heterogeneously integrated on silicon.” In: *Science* 373.6550, pp. 99–103. ISSN: 0036-8075. DOI: 10.1126/science.abh2076. eprint: https://science.sciencemag.org/content/373/6550/99.full.pdf. URL: https://science.sciencemag.org/content/373/6550/99.

Yan, Congliao et al. (2023). “Red and green light generation in TPPLNOI ridge optical waveguide with 1550 nm picosecond laser.” In: *Optics Communications* 529, p. 129023.

Yi, Xu et al. (2015). “Soliton frequency comb at microwave rates in a high-Q silica microresonator.” In: *Optica* 2.12, pp. 1078–1085.

Zhao, Chunyu et al. (2020). “Low-efficiency-droop InGaN quantum dot light-emitting diodes operating in the “green gap”.” In: *Photonics Research* 8.5, pp. 750–754.

Chapter 6

DOWN CONVERTED PHOTON PAIRS IN A HIGH-Q SILICON NITRIDE MICRORESONATOR

[1] Entangled photon pairs from spontaneous parametric down conversion (SPDC) (Harris, Oshman, and Byer, 1967) are central to many quantum applications (Kimble, 2008; Lvovsky, Sanders, and Tittel, 2009; H. Zhang et al., 2011; Simon, 2017; Wehner, Elkouss, and Hanson, 2018). SPDC is typically performed in non-centrosymmetric systems (Boyd, Gaeta, and Giese, 2008) that possess an inherent second-order nonlinearity ($\chi^{(2)}$) (Z. Ma et al., 2020; Javid et al., 2021; X. Guo et al., 2017). Here we demonstrate strong narrow-band SPDC with an on-chip rate of 0.8 million pairs per second in Si_3N_4. Si_3N_4 is both the preeminent material for photonic integration and also exhibits the lowest waveguide loss (essential for integrated quantum circuits); but, being amorphous, lacks an intrinsic $\chi^{(2)}$ and this limits its role in photonic quantum devices. SPDC in Si_3N_4 is enabled by combining strong light-field enhancement inside a high optical Q-factor microcavity with an optically-induced space-charge field. Narrow-band photon pairs with a record high spectral brightness are presented. The quantum nature of the down-converted photon pairs is verified through coincidence measurements. This light source, based on Si_3N_4 integrated photonics technology, unlocks new avenues for quantum systems on a chip.

6.1 Introduction

Since its demonstration (Harris, Oshman, and Byer, 1967), spontaneous parametric down-conversion (SPDC) has been widely used to generate entangled photon pairs for a range of applications (Kimble, 2008; Lvovsky, Sanders, and Tittel, 2009; H. Zhang et al., 2011; Simon, 2017; Wehner, Elkouss, and Hanson, 2018). Traditionally, non-centrosymmetric (Boyd, Gaeta, and Giese, 2008) materials with a strong $\chi^{(2)}$ have been used for SPDC. The advent of thin films of noncentrosymmetric materials has made possible SPDC in integrated photonics. For example, on-chip waveguides in lithium niobate (Z. Ma et al., 2020; Javid et al., 2021) and aluminum nitride (X. Guo et al., 2017) enable quantum light sources at smaller footprints and

[1] Work presented in this chapter has been published in "Down-converted photon pairs in a high-Q silicon nitride microresonator", *Nature* 639 (8056), 922-927.

their fabrication uses scalable methods. Along-side non-centrosymmetric systems, it has also been possible to induce an effective $\chi^{(2)}$ in amorphous systems by way of the photogalvanic effect. Historically, this approach was first demonstrated in optical fibers (Österberg and Margulis, 1986) where second-harmonic generation (SHG) was observed. More recently, a photo-galvanic induced $\chi^{(2)}$ has also been observed in Si_3N_4 waveguides where efficient second-harmonic generation has been generated (Puckett, Sharma, et al., 2016; Billat et al., 2017; X. Lu, Moille, et al., 2021; Nitiss et al., 2022; B. Li et al., 2023). Also, SPDC at low photon flux rates has been observed in Si_3N_4 waveguides (Dalidet et al., 2022).

The relatively weak nature of the photogalvanic induced $\chi^{(2)}$, compared to non-centrosymmetric systems, poses a challenge for its application to SPDC. Nonetheless, if overcome, SPDC in the Si_3N_4 system would offer unparalleled capability for photonic integration including heterogeneous integration with active components (Komljenovic et al., 2015; Xiang, J. Liu, et al., 2021). Moreover, the recent development of Si_3N_4 waveguides featuring ultra-low optical loss (W. Jin et al., 2021; Puckett, K. Liu, et al., 2021) makes this platform ideally suited for both transport of quantum states on chip and seamless (i.e., nearly lossless) coupling of these waveguides to an efficient SPDC source.

To overcome the weak second-order nonlinearity, we implement SPDC in high Q-factor Si_3N_4 resonators. Pair generation rates up to 0.8 million pairs/s on-chip are demonstrated at a record high spectral brightness. Furthermore, the associated resonance linewidths assure narrow-band SPDC such that the photon pair source could be applied in applications such as quantum memories (H. Zhang et al., 2011; Yunfei Wang et al., 2019) and entanglement swapping (Pan et al., 1998; Vitullo et al., 2018) without the need for a lossy spectral filter. Significantly, this generation rate is attained with only 1.5 mW on-chip pump power, a level that is readily attainable using semiconductor lasers heterogeneously integrated to the Si_3N_4 SPDC device (Xiang, J. Liu, et al., 2021). To confirm the quantum nature of these down-converted photons, coincidence measurements are performed and show a coincidence to accidental ratio ranging from 50 - 2500 depending upon on-chip pump power. We also report a transient behavior in the SPDC process, requiring periodic refresh of the photogalvanic effect.

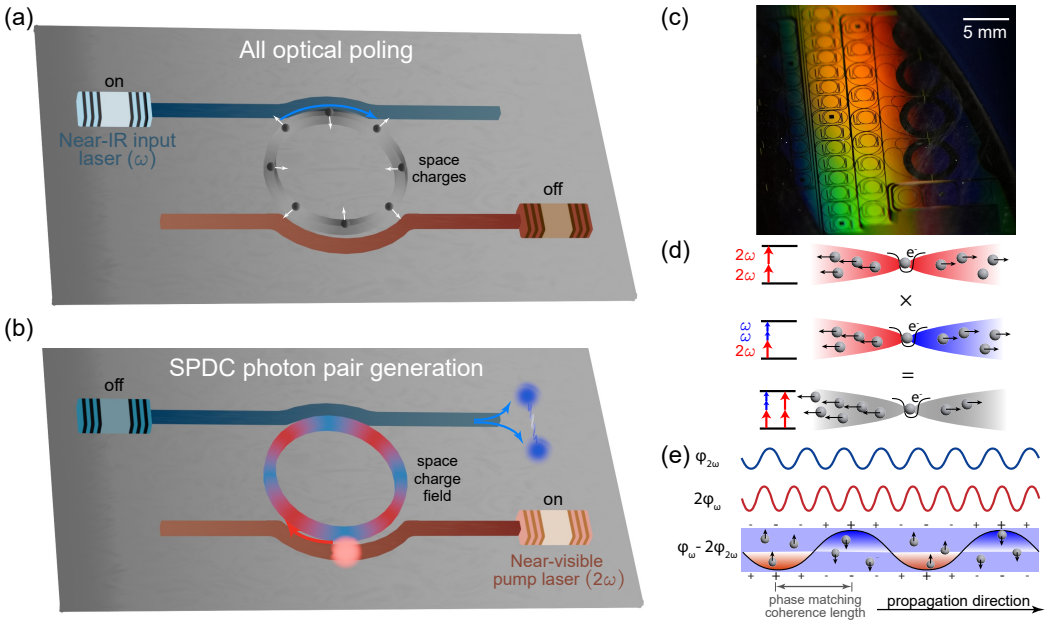

Figure 6.1: **Principle of photogalvanic-induced spontaneous parametric down conversion (SPDC). a** Depiction of periodic space-charge grating formation in a Si_3N_4 microresonator. Input light at ω (1560 nm) is coupled into the resonator and an initial weak second-harmonic signal at 2ω (780 nm) is generated through symmetry breaking, e.g., at the waveguide/cladding interface (Shen, 1989). The co-propagating input light and second-harmonic signal induce a periodic space-charge distribution. The resulting electric field combined with the inherent $\chi^{(3)}$ of Si_3N_4 create an effective $\chi^{(2)}$, thereby further enhancing the second-harmonic signal. **b** Depiction of SPDC in a Si_3N_4 microresonator. After space-charge grating formation (panel **a**), pump light at 780 nm is coupled into the resonator and near-IR entangled photon pairs are generated by SPDC at 1560 nm. Lasers (both 1560 nm and 780 nm) and resonators can be integrated on a semiconductor photonic chip. **c** Photograph of a section of the 8-inch wafer showing many Si_3N_4 resonators used in this work (highlighted region). **d** The photogalvanic process relies upon two-photon transitions (780 nm) and three-photon transitions (one 780 nm photon and two 1560 nm photons) that occur simultaneously in Si_3N_4. Quantum interference (Anderson, Mizrahi, and Sipe, 1991) of these two processes breaks symmetry and creates a field that induces drift of conduction electrons generated by the absorption process. **e** Diagram of the charge distribution with respect to the phase of two optical signals along the propagation direction. The net space-charge accumulation is proportional to the phase difference between two optical frequenciessin$(\phi_{2\omega} - 2\phi_{\omega})$. This space-charge distribution and the resulting electric field quasi-phase-matches the momentum difference for second-harmonic generation.

6.2 SPDC in silicon nitride waveguides

Fig. 6.1a and b illustrate the preparation and application of the SPDC process in a high-Q Si_3N_4 microresonator with an effective $\chi^{(2)}$. 780 nm (near-visible) pump

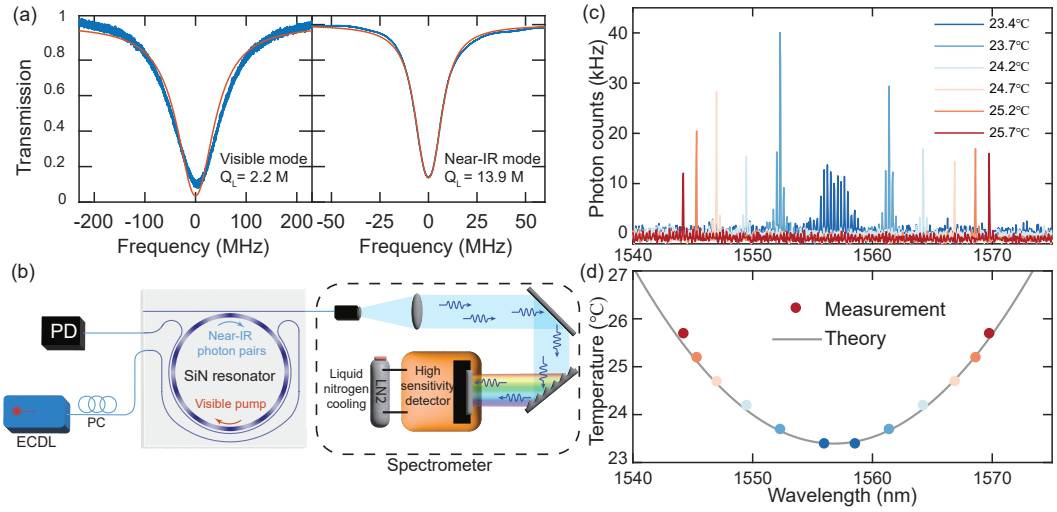

Figure 6.2: **Experimental results for photon pair generation.** **a** Measurements of resonator Q factor for near-visible (left panel) and near-IR (right panel) modes. Blue traces are measurements and red traces are the theoretical fitting. **b** Experimental setup for SPDC spectral measurements. A 780-nm external-cavity diode laser (ECDL) pumps the resonator and SPDC photons are analyzed by a liquid nitrogen cooled high-sensitivity spectrometer. **c** SPDC photon spectra measured at several chip temperatures given in the legend. **d** Measured wavelength-temperature dependence (dots) is plotted with the theoretical calculation based on thermal frequency tuning.

photons enter the microresonator and interact with a spatially varying $\chi^{(2)}$ to produce 1560 nm (near-IR) photon pairs through SPDC. Pump and SPDC photons are resonant in the cavity, and the resulting resonant enhancement makes it possible to leverage the relatively weak $\chi^{(2)}$ to realize significant photon pair generation rates. Moreover, the process is quasi-phase-matched, but unlike conventional quasi-phase-matching where lithographically-defined electrodes are required to write domains by application of an external electric field, quasi-phase-matching is performed without lithography through an all-optical induction process referred to as all-optical-poling (Billat et al., 2017; Hickstein et al., 2019; Nitiss et al., 2022). This process writes a periodic space-charge field through the photogalvanic effect, and this field in combination with the third-order Kerr effect ($\chi^{(3)}$ nonlinearity) induce an effective $\chi^{(2)}$ that reverses sign periodically to quasi-phase-match the SPDC process. For a high Q resonator, it is only necessary that pump and sub-harmonic resonances are frequency aligned by temperature tuning of the resonator. Fig. 6.1a provides an illustration of the resulting optical-induced $\chi^{(2)}$ inside a silicon nitride microresonator. Further details on the photogalvanic process are provided in the Fig. 6.1a-e caption.

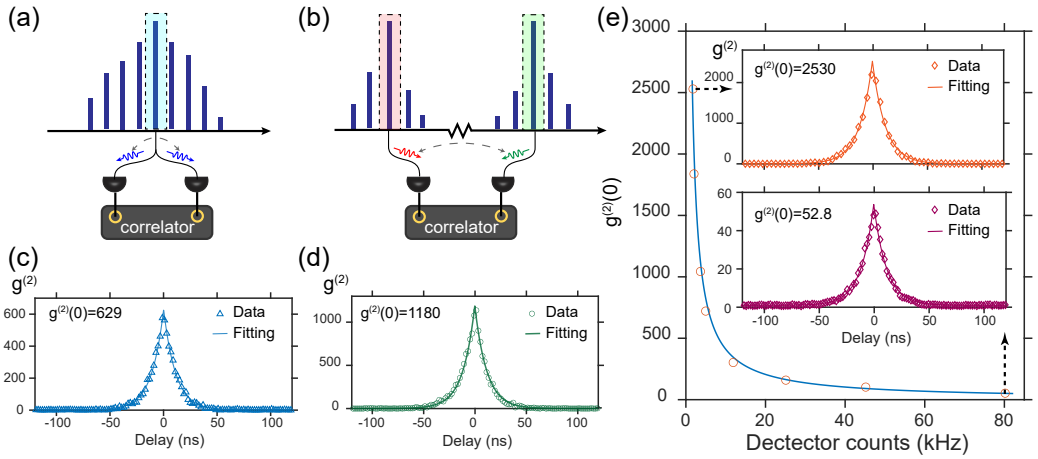

Figure 6.3: **Second-order quantum correlation measurement. a,b** Illustration of the measurement setup showing degenerate (a) and non-degenerate (b) cases. **c** Measured $g^{(2)}$ for the degenerate SPDC case through self-correlation. **d** Measured $g^{(2)}$ for the non-degenerate SPDC case through cross-correlation of signal and idler photons. **e** Measured $g^{(2)}(0)$ of non-degenerate SPDC at different pump powers. The red dots show the $g^{(2)}(0)$ at different detector count rates, and the blue curve is an inverse proportional fitting. Insets: $g^{(2)}(0) = 2530$ is obtained with a 17.2 kHz on-chip photon pair generation rate, and $g^{(2)}(0) = 52.8$ is obtained with a 795 kHz on-chip pair generation rate.

6.3 SPDC photon spectra

The resonator uses Si_3N_4 waveguides cladded with silica where the waveguide core (5 μm wide and 0.1 μm thick) is multimode. This wider dimension is found to reduce loss and boost Q factor. The free spectral range (FSR) of the resonator is 35 GHz. Two different waveguide-resonator couplers are used to couple 1560 nm and 780 nm light (see Fig. 6.1a,b,c). The pumping and fundamental coupler waveguides feature designs with slightly different geometries to ensure coupling to the fundamental mode of the resonator. Q factors of the near-IR mode and the near-visible mode are retrieved by fitting the linewidth of the Lorentzian transmission when a laser is scanned across the cavity's resonance. The measured Q factors are shown in Fig. 6.2a. After establishing an operating temperature at which frequency matching occurs between near-visible and near-IR modes, on-chip near-IR pumping power of 60 mW produces a second-harmonic (SH) signal through build-up of the photogalvanic $\chi^{(2)}$ and the concomitant SH generation achieves an efficiency of 650%/W. Details of the setup and characterization of SH generation are included in the Supplementary Information, section I.

After the effective $\chi^{(2)}$ is created, the resonator is pumped at the near-visible mode

for SPDC generation using a continuous-wave (cw) laser. The down conversion signal is collected through the 1560 nm port. Benefically, the 1560 nm coupler also serves as a filter that suppresses coupling of 780 nm pump light with a high extinction ratio of 60 dB.

The spectral distribution of the SPDC light is measured using a high sensitivity spectrometer (Fig. 6.2b). The results are shown in Fig. 6.2c where the measured spectra are integrated over 10 seconds and the indicated photon count rate is on-chip.

The down-conversion process can be degenerate or non-degenerate depending on the frequency matching condition as controlled by the chip temperature. Degenerate down-conversion happens when the near-visible mode frequency is exactly twice of the near-IR mode, the same condition as for SH generation. By increasing the temperature away from the SH matching frequency, the near-visible mode frequency mismatches the central near-IR mode (data in Fig. 6.2c), resulting in down-conversion to non-degenerate modes. However, on account of second-order dispersion, the down-conversion process experiences gradual phase mismatch with increasing amounts of non-degeneracy (i.e., signal and idler modes are more spectrally separated). This phase mismatch is given by $\omega_m + \omega_{-m} - 2\omega_0 = m^2 D_2$, where ω_0 is the near-IR frequency of perfect matching with the pump frequency, while ω_m and ω_{-m} are frequencies of the signal and idler modes (with m a relative mode number such that ω_0 corresponds to $m = 0$). Also, D_2 is the second order dispersion coefficient. The spectral locations of signal and idler waves versus temperature are plotted in Fig. 6.2d. Modeling (black curve in Fig. 6.2d) based on frequency tuning versus temperature measurements and measurements of the second-order dispersion agrees well with this data. Details of the model and measurement appear in the Supplementary Information, section II.

The cw pump and the narrow linewidth of the resonator ensure that signal and idler photons are spectrally separable provided that phase matching restricts emission into a single idler and single signal mode resonant frequency. Presently, this happens for two cases presented in Fig. 6.2c (respectively, colors orange and red at temperatures 25.2 and 25.7 °C). As discussed in the Supplementary Information, section III, the resonator second-order dispersion as well as resonator linewidth (or correspondingly optical Q factor) can be used to ensure the single idler/signal condition for spectral separability. Most notably, the use of a larger free-spectral-range resonator (> 74 GHz) would guarantee this condition for all cases. Conversely, multi-mode frequency-bin entangled sources can be useful for information encod-

ing when photon pairs are generated across multiple cavity resonances (dark blue and light blue traces in Fig. 6.2c) (Morrison et al., 2022). Nonetheless, in the current resonator design multiple simultaneous pair wavelengths can occur due to second order dispersion.

6.4 Quantum nature of the down converted photons

The quantum nature of the SPDC photon pairs is verified by measuring the second-order correlation $g^{(2)}$. Experimentally, down-converted photons are detected using superconducting single-photon detectors (SNSPDs) manufactured by ID Quantique. Both degenerate SPDC (Fig. 6.3a) and non-degenerate SPDC (Fig. 6.3b) cases are studied by temperature adjustment of the resonator. In the degenerate case, a spectral filter with 10 GHz bandwidth selects only the center mode and the filtered photon pair stream is passed through a 50/50 coupler before detection on the SNSPDs. In the non-degenerate case, signal and idler photons (typically separated by 10s of nm) are selected with two 10 GHz-bandwidth spectral filters before detection on the SNSPDs. In both cases, the second-order correlation is measured by counting the two-photon coincidence rates at different delay times for the two optical paths.

The two cases are first studied at a relatively-low pumping power of 50 μW (on-chip). Measurements of $g^{(2)}$ versus time delay for degenerate and non-degegenerate cases are presented in Figs. 6.3c and d, respectively. Fitting of the data (blue and green curves) uses the theoretical results: $g^{(2)}_{\text{degenerate}} = 1 + \frac{1}{4R\tau_L}e^{-\tau/\tau_L}$, and $g^{(2)}_{\text{non-degenerate}} = 1 + \frac{1}{2R\tau_L}e^{-\tau/\tau_L}$ for cavity-enhanced SPDC (Ou and Y. Lu, 1999; X. Guo et al., 2017). In these expressions, R is the photon pair generation rate, τ_L is the loaded cavity life time, and τ is the delay between two detectors. The data fitting gives a cavity lifetime of 11.2 ns and 11.9 ns for 6.3c and d, respectively, which are in good agreement with the lifetime of 11.5 ns obtained from the 13.9 million cavity Q measurement. Moreover, the fitted on-chip pair generation rates are 35 kHz and 33 kHz, respectively. These should be compared with the measured detector count rates of 3.7 kHz and 3.4 kHz for 6.3c and d, respectively. Accounting for the 9.8 dB chip to detector loss, these measurements are in good agreement with fitting to theory.

In Fig. 6.3e, we examine further the relationship between $g^{(2)}(0)$ and photon pair generation rate R. A larger generation rate reduces the $g^{(2)}(0)$ value due to a higher probability to detect non correlated photons. The observed inverse relationship of $g^{(2)}(0)$ on generation rate is consistent with the theory. In the measurement $g^{(2)}(0)$

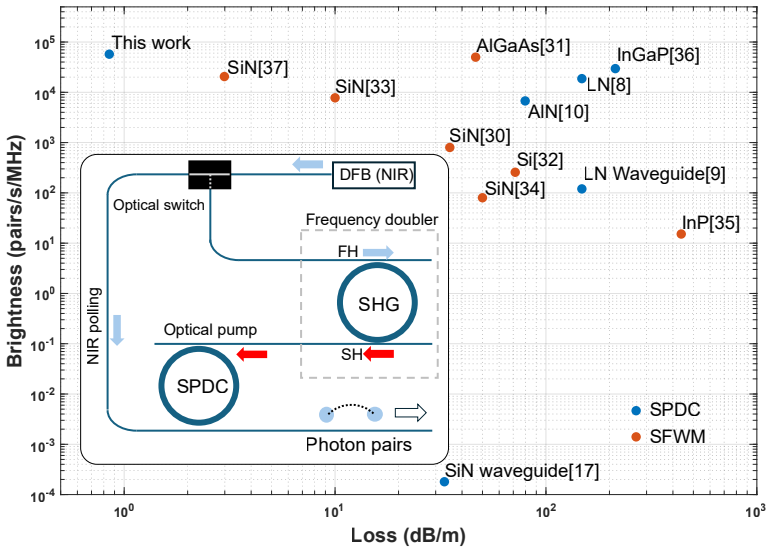

Figure 6.4: **Measured SFWM and SPDC brightness and loss performance comparison.** The performance of this work is compared and plotted with other integrated quantum photonics platforms using two metrics, waveguide optical loss and source brightness (see Ref.(Dalidet et al., 2022; X. Guo et al., 2017; Z. Ma et al., 2020; Javid et al., 2021; X. Lu, Q. Li, et al., 2019; Steiner et al., 2021; C. Ma et al., 2017; Fan et al., 2023; Wen et al., 2022; Kumar et al., 2019; M. Zhao and Fang, 2022; Chen et al., 2024)). The source brightness metric has been frequently used in this context. In addition, the comparison adds the waveguide loss metric which is of critical importance for integrated quantum systems since it impacts quantum state transport across the semiconductor chip. Brightness is calculated from the maximum reported pair generation rate divided by the spectral span (from the resonator total quality factor). Waveguide loss is estimated from the resonator intrinsic quality factor, if not reported. Both SFWM (red points) and SPDC (blue points) processes are included in the plot. The pump power used in the references are: this work: 1.5mW; ref. (Z. Ma et al., 2020): 13.4 μW; ref. (Javid et al., 2021): 0.45 mW; ref. (X. Guo et al., 2017): 2.3 mW; ref. (Dalidet et al., 2022): 0.43 mW; ref. (X. Lu, Q. Li, et al., 2019): 0.45 mW; ref. (Steiner et al., 2021): 25 μW; ref. (C. Ma et al., 2017): 60 μW; ref. (Fan et al., 2023): 2.0 mW; ref. (Wen et al., 2022): 6.2 mW; ref. (Kumar et al., 2019): 22 μW; ref. (M. Zhao and Fang, 2022): 1.2 μW; ref. (Chen et al., 2024): 0.33 mW. **Inset**: a conceptual figure for an integrated photonic SPDC source featuring a single integrated NIR (telecom) DFB pump that is frequency doubled (SHG) by a high-Q Si_3N_4 resonator to provide the near-visible pump for a high-Q Si_3N_4 resonator SPDC source.

values spanning 53 to 2530 are measured corresponding to detector count rates as high as 80.2 kHz (1.5 mW on-chip pump power) to as low as 1.8 kHz (25 μW on-chip pump power). As an aside, the 80.2 kHz at-detector rate corresponds to a 795

kHz on-chip rate, which is an exceptionally strong level for a non-centrosymmetric material.

During the experiment, we observed that the down-converted photon flux rate decays over time. We believe this is caused by washing-out of the space-charge distribution by the near-visible pump. At this wavelength, electrons may be excitepd to the conduction band through multi-photon absorption. These free charges could then drift to neutralize the accumulated charges and thereby reduce the effective $\chi^{(2)}$. At 1.5mW on-chip pump power, the reduction of pair production for non-degenerate conditions is relatively slow, taking several minutes to impact the measurement. Moreover, the generation rate fully recovers when pumping is combined with a near-IR signal. Specifically, this decay phenomena does not occur for SH generation when near-IR and visible are simultaneously present. Details on this behavior are provided in the Methods.

6.5 Discussion and outlook

In addition to SPDC, spontaneous four-wave-mixing (SFWM) also offers excellent performance for pair production on-chip (Duan et al., 2024). A comparison of both SPDC and SFWM demonstrated brightness versus waveguide optical loss is provided in Fig. 6.4. To compare usable photon pairs for applications, we consider the maximum reported photon pair generation rates in the literature. All the input power levels required are readily achievable with integrated laser sources (Xiang, W. Jin, et al., 2023). Although the photogalvanic-induced $\chi^{(2)}$ nonlinearity in our system is weak, the combination of a high-quality factor and high spectral coherence ensures that the generated photons are tightly centered within a narrow bandwidth for high brightness. Preservation of fidelities and interference visibilities of quantum states is facilitated during transport by chip integration. Ultra-low-loss waveguides further improve these metrics over chip scale distances, as well as over greater distances such as for introduction of time delay.

In contrasting SFWM with SPDC, SPDC requires a near-visible pump light source. However, in the present Si_3N_4 system, the photogalvanic effect can efficiently generate the SPDC pump as the second harmonic of a telecom pump (B. Li et al., 2023). As a result, the entire integrated SPDC system (including pair source and pump) can operate from a single telecom semiconductor laser pump in a manner similar to that employed for SFWM. This concept is illustrated as the inset of Figure 6.4. Furthermore, SPDC provides excellent (octave-span) pump and photon-pair isola-

tion on account of the intrinsic octave span nature of the process. And even while octave-span separation of photon pairs from the pump wave is possible in SFWM (X. Lu, Q. Li, et al., 2019), phase matching requires signal and idler photons to be widely separated in wavelength. Besides non-equivalent optical loss in transporting such widely separated photon pairs across a chip, integrated components typically feature very different characteristics over such wide optical spans. As a result, the ability of SPDC to generate photon pairs that are both well isolated from their pump, yet still within the telecom band, is a possible advantage.

In summary, we have demonstrated a strong SPDC process and verified its quantum nature in a non-centrosymmetric material. Moreover, the material, Si_3N_4, is the dominant photonic material for ultra-low-loss integration with other photonic devices including actives such as III-IV semiconductor lasers (Komljenovic et al., 2015; Xiang, J. Liu, et al., 2021). High Q factors also give rise to the concentrated frequency distribution and spectral separability of the down-converted photon pairs, which are important for interactions with atomic and narrow-linewidth solid-state systems in real applications. The ability to integrate both pump lasers (780 nm) and near-IR lasers (1560 nm) with the SPDC cavity also provides a way to refresh the space charge to ensure that the system can work repetitively. Integration with other components will also enable more complex systems on-a-chip that rely upon the SPDC process. Overall, the addition of the SPDC process to the suite of capabilities provided by Si_3N_4 offers significant opportunities for the photonic integration of quantum systems (O'brien, Furusawa, and Vučković, 2009; Moody et al., 2022).

6.6 Experiment details

Effective $\chi^{(2)}$ creation through second-harmonic generation.

To induce an effective $\chi^{(2)}$ and simultaneously quasi-phase-match the down conversion process, a space-charge grating is created using the experimental setup in Extended Data Fig. 6.5a. The temperature of the microresonator is carefully controlled to frequency match the visible mode and the near-IR cavity mode, and monitoring of these frequencies is performed using a near-IR band tunable laser (1560 nm) that is frequency-doubled using a periodically-poled lithium niobate crystal. Once this is done, the frequency of the near-IR laser is tuned into the cavity resonance. A periodic space-charge field then builds up and generates second-harmonic (SH) power as described elsehere (B. Li et al., 2023). Steady-state is achieved within a few seconds and the grating persists for a long time without the external excitation.

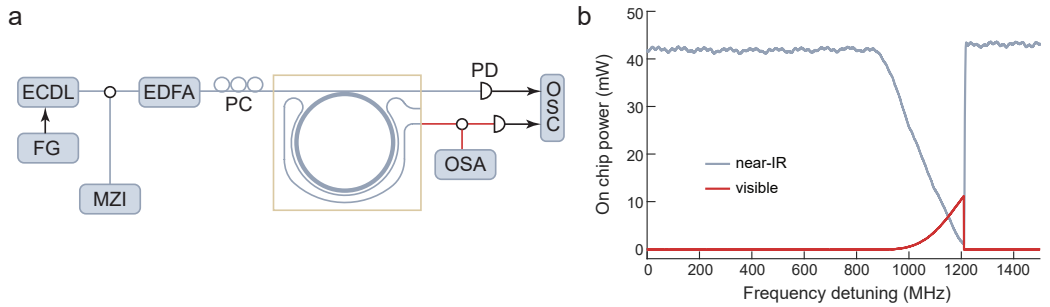

Figure 6.5: **Experimental setup and characterization of second harmonic generation. a** An external cavity diode laser (ECDL) is amplified by an erbium-doped fiber amplifier (EDFA), and then coupled to the resonator chip using a lensed fiber. The chip-waveguide is designed to couple power in the near-IR (1560 nm) to the high-Q silicon nitride microresonator. The SH harmonic signal is coupled to the second waveguide. A microwave function generator (FG) enables frequency sweeping of the laser, and the frequency sweep is measured using a calibrated Mach-Zehnder interferometer (MZI). The transmitted 1560 nm signal and the generated SH signal are collected and sent into two photodetectors (PDs), separately. The detected electrical signals are sent into an oscilloscope (OSC). Also shown are PC: polarization controller, OSA: optical spectrum analyzer. **b** After the space-charge grating builds up, the on-chip transmitted pump power (blue) and generated SH power (red) are recorded when scanning the frequency of the pump laser across a cavity resonance.

The SH power conversion efficiency and $\chi^{(2)}$ strength are then characterized using a lower-power near-IR pump power, as shown in Extended Data Fig. 6.5b. Here, 11 mW on-chip 780 nm SH signal is observed when 41 mW of 1560nm laser power is launched into the waveguide. This corresponds to a second-harmonic efficiency (η) of 651%/W. We believe this value is limited by saturation of the SH process and the presence of cascaded sum-frequency generation to 520 nm.

For comparison, second-harmonic efficiency can also be estimated from the measured photon pair generation rate, R, and visible (780 nm) pump power, P_{vis}, in the SPDC process (X. Guo et al., 2017):

$$R = \frac{\kappa_{\mathrm{IR,\,L}}^3}{8\kappa_{\mathrm{IR,\,e}}^2}\eta P_{\mathrm{vis}}, \tag{6.1}$$

where $\kappa_{\mathrm{IR,\,L}}$ ($\kappa_{\mathrm{IR,\,e}}$) is the loaded (external) cavity loss rate of the near-IR mode. At 1.5 mW on chip pump power, the photon pair generation rate is measured to be 800 kHz. Using the above expression and optical loss rates from the main text, an SHG efficiency of η =624%/W is calculated, in close agreement with the above measured

value. As an aside, we expect this calculation to underestimate the peak SHG efficiency, because, as noted in the main text, the charge distribution faded away in the presence of the 780 nm pump (see Methods for more details). In particular, the 800 kHz rate was recorded a few minutes after the 780 nm pump had been coupled into the resonator and the charge distribution would therefore not be as strong as the initial state. Overall, the agreement of these two inferred efficiency values might be fortuitous in view of the experimental uncertainties.

SPDC spectral measurements. We use a a low-noise liquid nitrogen cooled spectrometer for spectral measurements, *PyLoN* IR 1024-1.7 with a quantum efficiency of $> 75\,\%$. The spectrometer is equipped with a 300 g/mm grating (1.2 μm blaze) and an efficiency of $> 50\%$ for wavelengths < 1600 nm.

Temperature dependence of the photon pair wavelengths. The wavelengths of the generated photon pairs are determined by the frequency matching condition between the visible pump mode and the near-IR-band mode family. To determine this matching condition, the dispersion of the near-IR mode family is first measured using a calibrated Mach–Zehnder interferometer in combination with a wavelength-tunable laser (Yi et al., 2015). The resonant frequency ω_m of mode m can be approximated as a Taylor series relative to a mode at ω_0 defined to have a relative mode number $m = 0$:

$$\omega_m = \omega_0 + D_1 m + \frac{1}{2} D_2 m^2 + \sum_{j>2} \frac{1}{j!} D_j m^j, \tag{6.2}$$

where D_j is the j-th order dispersion coefficient. Specifically, $D_1/2\pi$ equals the FSR and D_2 is the second-order dispersion coefficient at mode $m = 0$. As shown in Extended Data Fig. 6.6a, a second-order expansion agrees well with measurements over a range of mode numbers within a few 100 of $m = 0$. The parabolic fitting gives $D_2/2\pi$ = -863.7 kHz.

The resonant frequency tuning coefficients $\delta\omega/\delta T$ are directly measured by varying the temperature of the microresonator chip using a thermoelectric cooler (TEC). The results are shown in Extended Data Fig. 6.6b. Using these measurements, the relative frequency detuning rate $(\delta\omega_{\mathrm{vis}}/\delta T - 2\delta\omega_{\mathrm{IR}}/\delta T)$ is determined to be -814.8 MHz/K. Combined with the negative D_2 measured above, the temperature detuning coefficient changes the SPDC process from degenerate to non-degenerate with changing resonator temperature. Accordingly, suppose that the degenerate SPDC process is phase matched to near-IR mode number $m = 0$ at temperature T_0

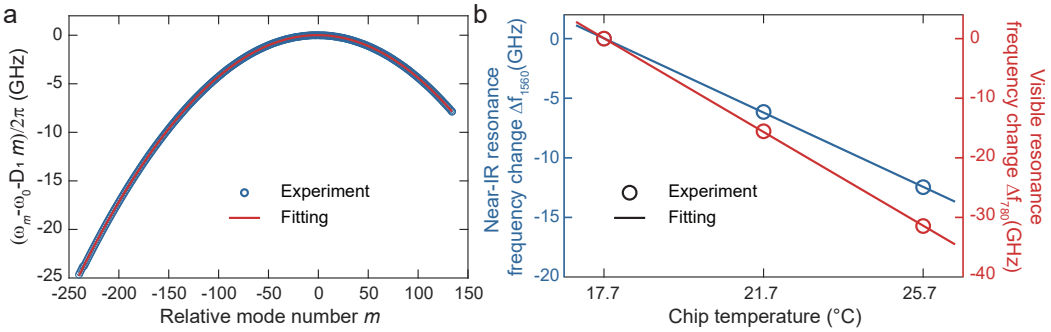

Figure 6.6: **Measurement of resonator dispersion relation and resonance temperature tuning coefficients.** **a** Measured frequency dispersion (blue circles) of the mode family in the near-IR band is plotted versus the relative mode number m. The solid red curve is a parabolic fit using $D_1/2\pi$ = 35.09 GHz and $D_2/2\pi$ = -863.7 kHz. In the plot, the mode frequencies are offset by the linear term in the Taylor expansion to make clear the second-order group dispersion, and ω_0 is chosen so that $m = 0$ phase matches to the the pump mode in the SHG process (1557.372 nm). **b** Measured frequency tuning of both near-IR (left axis) and visible (right axis) cavity mode frequencies as a function of temperature. The frequencies of the cavity mode resonances at 17.7 °C are chosen as a reference, separately.

(i.e., $\omega_{\mathrm{vis}}(T_0) = 2\omega_0(T_0)$). Then, using the dispersion expansion (Eqn. 6.2), the non-degenerate phase matching condition at temperature T can be written as,

$$\omega_{\mathrm{vis}}(T) = \omega_m(T) + \omega_{-m}(T) = 2\omega_0(T) + D_2 m^2, \tag{6.3}$$

$$D_2 m^2 = \omega_{\mathrm{vis}}(T) - 2\omega_0(T) = (\delta\omega_{\mathrm{vis}}/\delta T - 2\delta\omega_{\mathrm{IR}}/\delta T)(T - T_0). \tag{6.4}$$

where mode numbers $+m$ and $-m$ are the relative mode numbers of the near-IR modes involved in the SPDC process. From Eq. 6.4 and using the measured value for $\delta\omega_{\mathrm{vis}}/\delta T - 2\delta\omega_{\mathrm{IR}}/\delta T$, the quadratic coefficient of the chip temperature as a function of the photon pair wavelength is calculated to be 0.0131 K/nm^2, and is used to plot the quadratic function in Fig. 6.2d in the main text.

Bandwidth of the down-converted photon pairs. In the spontaneous down conversion process, a few near-IR mode pairs can phase match with the visible pump mode, because slight frequency mismatch caused by dispersion can be smaller than the resonator linewidth. The phase matching condition can be written as:

$$D_2 m_{\mathrm{max}}^2 - D_2 m_{\mathrm{min}}^2 = 2\Delta\omega, \tag{6.5}$$

where $\pm m_{\mathrm{max}}$ ($\pm m_{\mathrm{min}}$) is the largest (smallest) relative mode number of the phase matched mode pairs, and $\Delta\omega = \omega/Q$ is the full width at half maximum (FWHM)

of the near-IR resonances. In the degenerate case, $m_{\text{min}} = 0$. m_{max} is then given by,

$$D_2 m_{\text{Deg,max}}^2 = 2\Delta\omega, \tag{6.6}$$

Using current resonator values, $m_{\text{Deg,max}}$ is calculated to be 5.7, which is consistent with the dark blue trace in Fig. 6.2c in the main text.

A condition for $m_{\text{Deg,max}}$=1 is given by $D_2 > 2\Delta\omega = 2\omega_0/Q$ where Q is the loaded cavity Q-factor of the near-IR modes. By rewriting D_2 in terms of free-spectral-range $\Delta\nu_{\text{FSR}}$ (Hertz units) and the waveguide group velocity dispersion parameter β_2 (Yi et al., 2015), the following design condition for single mode SPDC emerges,

$$Q\Delta\nu_{\text{FSR}}^2 > \frac{n}{\pi\lambda_0|\beta_2|}, \tag{6.7}$$

where λ_0 and n are the wavelength and effective index of the mode $m = 0$, respectively. β_2 is related to D_2 as $\beta_2 = -nD_2/cD_1^2$, and is calculated to be 540 $\text{ps}^2\text{km}^{-1}$, using the parameters from the previous section. For other values typical of the ultra-low-loss Si_3N_4 system, this gives $Q\Delta\nu_{\text{FSR}}^2 > 5.49 \times 10^{11}$ GHz^2. Assuming Q = 100 million, which is readily attainable by this system, $\Delta\nu_{\text{FSR}} > 74$ GHz is sufficient to guarantee single-mode degenerate SPDC.

In the non-degenerate case, the equation can be modified as:

$$2\Delta\omega = 2D_2\overline{m}\Delta m, \tag{6.8}$$

where $\overline{m} = (m_{\text{max}} + m_{\text{min}})/2, \Delta m = (m_{\text{max}} - m_{\text{min}})/2$. At 23.7 °C, $\overline{m}$ = 16, and Δm is calculated to be 1. This is again consistent with observations since on both long and short wavelengths of the spectrum, photon fluxes are observed in only one neighbouring mode on each side of the strongest mode. At even higher temperatures, no side peaks are observed in the spectrum.

$g^{(2)}$ measurements. The $g^{(2)}(t)$ and pair generation rates are measured via a pair of 1.55 μm SNSPDs with a quantum efficiency of 85% provided from ID Quantique. Signal from the SNSPDs is recorded by a ID900 time-to-digital converter with a temporal resolution of 2 ns.

Characterization on the temporal degradation of the effective $\chi^{(2)}$. As mentioned in the main text, the SPDC rate is observed to decay in time. We believe this phenomenon to result from multiphoton excitation of conduction band electrons by the 780 nm pump. These electrons would gradually neutralize the space charge,

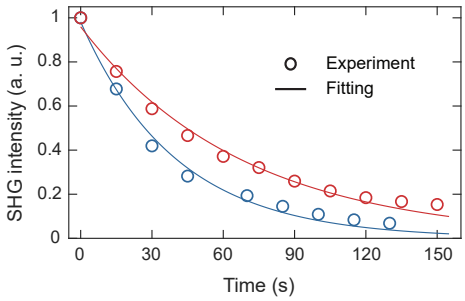

Figure 6.7: **Measured $\chi^{(2)}$ intensity decay as a function of time at different visible pump powers.** The second-harmonic intensity is normalized to the initial condition after writing of the space-charge grating. The red (blue) circles refer to the on-chip pump power of 0.5 (1.5) mW and are fitted by a exponential function (solid lines). The decay lifetime is fitted to be 68 (40) s, respectively.

thereby diminishing the effective $\chi^{(2)}$. This section provides an investigation on the speed of this effect. It is experimentally challenging to reconstruct the decay directly from the SPDC rate, because the SPDC rate is sensitive to temperature and laser detuning. Alternatively, we chose to monitor the charge through the second harmonic generation signal when scanning the 1560 nm laser across the resonance and recording the peak value of the second-harmonic signal, such as shown in Extended Data Fig. 6.5b. This measurement samples a range of different detunings and should be less affected by the temperature change.

The experimental setup is the same as in Extended Data Fig. 6.5a. The space-charge grating is first introduced through second harmonic generation as described in section I. Then, the 1560 nm laser is turned off and the 780 nm laser is tuned into resonance to simulate the condition of SPDC. Each time after a 15 s interval, the 780 nm signal is turned off and the 1560 nm is scanned across the resonance to collect the second-harmonic peak value. Two, on-chip 780 nm pump powers (0.5 mW, 1.5 mW) are used, and the result is shown in Extended Data Fig. 6.7. An exponential decay fit to the data gives lifetimes of 68 s and 40 s for pumping powers 0.5 mW and 1.5 mW, respectively. As expected, the decay is faster with the higher pump power. We also note that as time increases, the data significantly deviate from the exponential fit and decay rate decreases. Possible mechanisms that could impact SHG efficiency include changes in pump laser phase or polarization. Since the SPDC measurement in the main text requires a wait time of a few minutes for chip temperature to achieve steady state, the observed decay times are consistent

with our observation that the SPDC rate can be observed over several minutes.

References

Anderson, Dana Z, Victor Mizrahi, and John E Sipe (1991). "Model for second-harmonic generation in glass optical fibers based on asymmetric photoelectron emission from defect sites." In: *Optics letters* 16.11, pp. 796–798.

Billat, Adrien et al. (2017). "Large second harmonic generation enhancement in Si3N4 waveguides by all-optically induced quasi-phase-matching." In: *Nature communications* 8.1, p. 1016.

Boyd, Robert W, Alexander L Gaeta, and Enno Giese (2008). "Nonlinear optics." In: *Springer Handbook of Atomic, Molecular, and Optical Physics*. Springer, pp. 1097–1110.

Chen, Ruiyang et al. (2024). "Ultralow-loss integrated photonics enables bright, narrowband, photon-pair sources." In: *Physical Review Letters* 133.8, p. 083803.

Dalidet, Romain et al. (2022). "Near perfect two-photon interference out of a down-converter on a silicon photonic chip." In: *Optics Express* 30.7, pp. 11298–11305.

Duan, Liao et al. (2024). "Broadband Entangled-Photon Pair Generation with Integrated Photonics: Guidelines and A Materials Comparison." In: *arXiv preprint arXiv:2407.04792v1*.

Fan, Yun-Ru et al. (2023). "Multi-Wavelength Quantum Light Sources on Silicon Nitride Micro-Ring Chip." In: *Laser & Photonics Reviews* 17.10, p. 2300172.

Guo, Xiang et al. (2017). "Parametric down-conversion photon-pair source on a nanophotonic chip." In: *Light: Science & Applications* 6.5, e16249–e16249.

Harris, SE, MK Oshman, and RL Byer (1967). "Observation of tunable optical parametric fluorescence." In: *Physical Review Letters* 18.18, p. 732.

Hickstein, Daniel D et al. (2019). "Self-organized nonlinear gratings for ultrafast nanophotonics." In: *Nature Photonics* 13.7, pp. 494–499.

Javid, Usman A et al. (2021). "Ultrabroadband entangled photons on a nanophotonic chip." In: *Physical Review Letters* 127.18, p. 183601.

Jin, Warren et al. (2021). "Hertz-linewidth semiconductor lasers using CMOS-ready ultra-high-Q microresonators." In: *Nat. Photon.* 15.5, pp. 346–353.

Kimble, H Jeff (2008). "The quantum internet." In: *Nature* 453.7198, pp. 1023–1030.

Komljenovic, Tin et al. (2015). "Heterogeneous silicon photonic integrated circuits." In: *Journal of Lightwave Technology* 34.1, pp. 20–35.

Kumar, Rakesh Ranjan et al. (2019). "Entangled photon pair generation from an InP membrane micro-ring resonator." In: *Applied Physics Letters* 114.2.

Li, Bohan et al. (2023). "High-coherence hybrid-integrated 780 nm source by self-injection-locked second-harmonic generation in a high-Q silicon-nitride resonator." In: *Optica* 10.9, pp. 1241–1244.

Lu, Xiyuan, Qing Li, et al. (2019). "Chip-integrated visible–telecom entangled photon pair source for quantum communication." In: *Nature physics* 15.4, pp. 373–381.

Lu, Xiyuan, Gregory Moille, et al. (2021). "Efficient photoinduced second-harmonic generation in silicon nitride photonics." In: *Nature Photonics* 15.2, pp. 131–136.

Lvovsky, Alexander I, Barry C Sanders, and Wolfgang Tittel (2009). "Optical quantum memory." In: *Nature photonics* 3.12, pp. 706–714.

Ma, Chaoxuan et al. (2017). "Silicon photonic entangled photon-pair and heralded single photon generation with CAR> 12,000 and g (2)(0)< 0.006." In: *Optics Express* 25.26, pp. 32995–33006.

Ma, Zhaohui et al. (2020). "Ultrabright quantum photon sources on chip." In: *Physical Review Letters* 125.26, p. 263602.

Moody, Galan et al. (2022). "2022 Roadmap on integrated quantum photonics." In: *Journal of Physics: Photonics* 4.1, p. 012501.

Morrison, Christopher L et al. (2022). "Frequency-bin entanglement from domain-engineered down-conversion." In: *APL Photonics* 7.6.

Nitiss, Edgars et al. (2022). "Optically reconfigurable quasi-phase-matching in silicon nitride microresonators." In: *Nature Photonics* 16.2, pp. 134–141.

O'brien, Jeremy L, Akira Furusawa, and Jelena Vučković (2009). "Photonic quantum technologies." In: *Nature photonics* 3.12, pp. 687–695.

Österberg, U and Walter Margulis (1986). "Dye laser pumped by Nd: YAG laser pulses frequency doubled in a glass optical fiber." In: *Optics letters* 11.8, pp. 516–518.

Ou, ZY and YJ Lu (1999). "Cavity enhanced spontaneous parametric down-conversion for the prolongation of correlation time between conjugate photons." In: *Physical Review Letters* 83.13, p. 2556.

Pan, Jian-Wei et al. (1998). "Experimental entanglement swapping: entangling photons that never interacted." In: *Physical review letters* 80.18, p. 3891.

Puckett, Matthew W, Kaikai Liu, et al. (2021). "422 Million intrinsic quality factor planar integrated all-waveguide resonator with sub-MHz linewidth." In: *Nat. Commun.* 12.1, pp. 1–8.

Puckett, Matthew W, Rajat Sharma, et al. (2016). "Observation of second-harmonic generation in silicon nitride waveguides through bulk nonlinearities." In: *Optics Express* 24.15, pp. 16923–16933.

Shen, YR (1989). “Surface properties probed by second-harmonic and sum-frequency generation.” In: *Nature* 337.6207, pp. 519–525.

Simon, Christoph (2017). “Towards a global quantum network.” In: *Nature Photonics* 11.11, pp. 678–680.

Steiner, Trevor J et al. (2021). “Ultrabright entangled-photon-pair generation from an al ga as-on-insulator microring resonator.” In: *PRX Quantum* 2.1, p. 010337.

Vitullo, Dashiell LP et al. (2018). “Entanglement swapping for generation of heralded time-frequency-entangled photon pairs.” In: *Physical Review A* 98.2, p. 023836.

Wang, Yunfei et al. (2019). “Efficient quantum memory for single-photon polarization qubits.” In: *Nature Photonics* 13.5, pp. 346–351.

Wehner, Stephanie, David Elkouss, and Ronald Hanson (2018). “Quantum internet: A vision for the road ahead.” In: *Science* 362.6412, eaam9288.

Wen, Wenjun et al. (2022). “Realizing an entanglement-based multiuser quantum network with integrated photonics.” In: *Physical Review Applied* 18.2, p. 024059.

Xiang, Chao, Warren Jin, et al. (2023). “3D integration enables ultralow-noise isolator-free lasers in silicon photonics.” In: *Nature* 620.7972, pp. 78–85.

Xiang, Chao, Junqiu Liu, et al. (2021). “Laser soliton microcombs heterogeneously integrated on silicon.” In: *Science* 373.6550, pp. 99–103. ISSN: 0036-8075. DOI: 10.1126/science.abh2076. eprint: https://science.sciencemag.org/content/373/6550/99.full.pdf. URL: https://science.sciencemag.org/content/373/6550/99.

Yi, Xu et al. (2015). “Soliton frequency comb at microwave rates in a high-Q silica microresonator.” In: *Optica* 2.12, pp. 1078–1085.

Zhang, Han et al. (2011). “Preparation and storage of frequency-uncorrelated entangled photons from cavity-enhanced spontaneous parametric downconversion.” In: *Nature Photonics* 5.10, pp. 628–632.

Zhao, Mengdi and Kejie Fang (2022). “InGaP quantum nanophotonic integrated circuits with 1.5% nonlinearity-to-loss ratio.” In: *Optica* 9.2, pp. 258–263.

Chapter 7

CONCLUSION AND OUTLOOK

Several works centered around frequency stabilization and frequency conversion using the silicon nitride microresonator is presented in this thesis. At the conclusion of this thesis, a brief summary and outlook from my own perspective will be provided for each individual work.

In chapter 2, a DFB laser diode self-injection-locked to a silicon nitride spiral resonator can achieve a performance compatible with commercial fiber laser. This is a mature result built on serval years iteration of resonator designs. The trick is to pick a thickness that can allow bending radius to form a compact spiral while not too thick to cause extra loss. The spiral resonator is already a few centimeters in its radius, making it larger will lose the benefit of compact and there is little room for improvement. The next step would be moving from hybrid integrated laser to heterogeneous integrated laser as in (Xiang et al., 2023). The challenges are the degradation of quality factors during the process and low laser to microresonator coupling factors due to extra waveguide needed as a bridge between two materials. These two factors are critical for noise performance and are also hard to address.

In chapter 3, a home-build method for laser noise measurement is presented. It achieves a low noise floor at high frequency offsets, enough for measuring the frequency noise of the state-of-the-art integrated lasers. There is commercially available equipment that can achieve similar or better performance but at a cost of more than 40k USD. This work presents an affordable way to measure low frequency noise for research groups. The noise floor at low frequency offset (below 1kHz) is large, which may be addressed by better mechanical and temperature stabilization of the measurement setup.

In chapter 4, a low-noise 780nm laser signal is obtained through self-injection-lock second harmonic generation. This is perhaps the first application of second harmonic generation in silicon nitride. The design of the resonator has not gone through iterations and there is large space for improvements. The quality factor of near-IR mode is around 20M, which in principle can be improved to 50M in a better fabrication run. This will directly improve the SHG efficiency and laser linewidth. One benefit of this method is the noise reduction factor only relies on the quality

factor of the near-IR mode, and the noise performance can remain unimpacted by the quality factor of 780nm mode. Designing and fabricating a high-quality factor resonator at 780nm is less mature as the 780nm wavelength is not used as common as the telecom band.

Chapter 5 extends the SHG wavelength to 520nm. This further suggests that it can be generalized to the second harmonic generation of other wavelengths. The photogalvanic effect could in principle be applied to sum/difference frequency generation. In this case, two different frequencies of laser are pumped into the resonator and their difference frequency or sum frequency is generated. This would make the frequency conversion using photogalvanic effect more versatile.

Chapter 6 presents the efficient generation of entangled photon pairs using photogalvanic effect. It shows the $\chi^{(2)}$ process of silicon nitride could be efficient enough for down-conversion applications. Further research direction should be optical parametric down(OPO) conversion using the $\chi^{(2)}$. Current OPO threshold is theoretically calculated in the order of Watt. Given the design of microresonator is still in its first generation, efficiency may be improved by optimizing the design. Other challenges are presented such that the charges may be washed away by the second harmonic pump. Hypothetically, if OPO signal is generated, it can sustain the grating charges together with the pump signal. A broad range of applications are available if OPO can be achieved.

In conclusion, frequency stabilization relying on the high quality factor of silicon nitride resonator is quite mature and at the state-of-the-art of integrated photonics. The frequency conversion using second-order nonlinearity induced by photogalvanic effect is relatively new, not well-understood and has promising potentials.

References

Xiang, Chao et al. (2023). “3D integration enables ultralow-noise isolator-free lasers in silicon photonics.” In: *Nature* 620.7972, pp. 78–85.